The provenance of late Cenozoic East Asian Red Clay : Tectonic-metamorphic history of potential source regions and a novel combined zircon-rutile approach

Bohm, Katja

2022-02

Bohm , K , Stevens , T , Kaakinen , A , Lahaye , Y , O'Brien , H & Zhang , Z 2022 , ' The provenance of late Cenozoic East Asian Red Clay : Tectonic-metamorphic history of potential source regions and a novel combined zircon-rutile approach ' , Earth - Science Reviews , vol. 225 , 103909 . https://doi.org/10.1016/j.earscirev.2021.103909

http://hdl.handle.net/10138/339653
https://doi.org/10.1016/j.earscirev.2021.103909

Earth-Science Reviews 225 (2022) 103909

Contents lists available at ScienceDirect

Earth-Science Reviews

journal homepage: www.elsevier.com/locate/earscirev

The provenance of late Cenozoic East Asian Red Clay: Tectonic-metamorphic history of potential source regions and a novel combined zircon-rutile approach

Katja Bohm [a,b,*], Thomas Stevens [b], Anu Kaakinen [a], Yann Lahaye [c], Hugh O'Brien [c], Zhaoqun Zhang [d,e,f]

[a] Department of Geosciences and Geography, University of Helsinki, P.O. Box 64, FI-00014, Finland
[b] Department of Earth Sciences, Uppsala University, Villavägen 16, SE-752 36 Uppsala, Sweden
[c] Geological Survey of Finland, P.O. Box 96, 02151 Espoo, Finland
[d] Key Laboratory of Vertebrate Evolution and Human Origin of the Chinese Academy of Sciences, Institute of Vertebrate Paleontology and Paleoanthropology, Chinese Academy of Sciences, Beijing 100044, China
[e] CAS Center for Excellence in Life and Paleoenvironment, Beijing, China
[f] University of Chinese Academy of Sciences, Beijing, China

ARTICLE INFO

Keywords:
Mineral dust
Single-grain provenance
Detrital zircon
Detrital rutile
Chinese Loess Plateau
Nihewan

ABSTRACT

Constraining the provenance of aeolian mineral dust is critical in understanding past climate changes, atmospheric dust activity, circulation, and sediment generation. On the Chinese Loess Plateau (CLP), use of detrital zircon U-Pb age data as source tracers for the dust has seen a huge growth and lead to breakthroughs in understanding dust provenance. However, significant ambiguities remain especially regarding the provenance of the aeolian Neogene Red Clay (RC). To address this, here we review the state of the art of understanding of Neogene RC provenance, with a focus on single-grain analyses, and introduce detrital rutile geochemistry as a tool to complement zircon U-Pb dating. Furthermore, to better utilise the link between the detrital minerals and their primary origin, we compile primary source region geologic background and single-grain data relevant for use of geochronological and metamorphic provenance proxy minerals. We discuss four major tectonic divisions in northern China and southern Mongolia: North China Craton (NCC), Tarim Craton (TC), Central China Orogen (CCO), parts of the Central Asian Orogenic Belt (CAOB), and briefly summarize the Tibetan-Himalayan orogen. Many of these regions have been tectonically active during the same time periods in the Earth's history, and our analysis demonstrates how use of zircon age data alone has limitations in differentiating between a number of key potential dust sources to the CLP. Addition of a metamorphic source tracer such as rutile allows some of these possible source areas to be distinguished. For example, the proximal northern NCC regions that show high−/ultrahigh-temperature metamorphic conditions can potentially be diagnostic of a northerly source component to CLP dust. Our combined zircon-rutile data analysis of ca. 4 Ma Nihewan RC in northern CLP verifies the utility of the novel rutile provenance proxy in sourcing CLP sediments. The zircon and rutile data suggest similar dust provenance: the dominant sources are proximal areas on the NCC, while contributions from the dry areas in parts of the CAOB, central deserts, and the Yellow River are also likely. Our results also hint at a minor source component deriving from distal western source regions in the TC, and/or in the central parts of the CCO, but rutile data from potential secondary source areas are needed to verify this possibility. We also conclude that multi-proxy single-grain provenance analyses are needed for more reliable provenance analyses.

Abbreviations: CAOB, Central Asian Orogenic Belt; CCO, Central China Orogen; CLP, Chinese Loess Plateau; EASM, East Asian summer monsoon; EAWM, East Asian winter monsoon; EKO, East Kunlun Orogen; HP, high-pressure; HT, high-temperature; IMSZ, Inner Mongolia Suture Zone; KB, Khondalite Belt; LIP, Large Igneous Province; MDS, Multidimensional scaling; MML, Main Mongolian Lineament; NCC, North China Craton; NQO, North Qilian Orogen; NQUHP, North Qaidam ultrahigh-pressure Belt; PAO, Palaeo-Asian Ocean; QOB, Qinling Orogenic Belt; RC, Red Clay; SGC, Songpan-Ganzi complex; TC, Tarim Craton; TNCO, Trans-North China Orogen; TP, Tibetan Plateau; TTG, Tonalite-trondhjemite-granodiorite; UHP, Ultrahigh-pressure; UHT, Ultrahigh-temperature; YR, Yellow River.

* Corresponding author at Department of Geosciences and Geography, University of Helsinki, P.O. Box 64, FI-00014, Finland.
E-mail address: katja.bohm@helsinki.fi (K. Bohm).

https://doi.org/10.1016/j.earscirev.2021.103909
Received 29 June 2021; Received in revised form 16 December 2021; Accepted 20 December 2021
Available online 28 December 2021

1. Introduction

The information linking an eroding original (primary) rock and a subsequent sediment deposit can persist in a detrital mineral grain for millions of years. This information is fundamental in understanding the erosion and denudation of land, and of sediment cycling from source to sink. For a long time, this fundamental information has been out of reach for fine-grained, dominantly silt to clay sized wind-blown sediments (deposits of atmospheric mineral dust), but recently has become more attainable because new analytical instruments are capable of single-grain analyses of fine silt particles. This is of crucial importance as it is increasingly recognised that atmospheric mineral dust plays a significant role in the global climate system, yet this role is still poorly understood, and the multiple interactions between dust and climate are hard to fully synthesize in climate models (Kohfeld and Harrison, 2001; Shao et al., 2011; Tegen, 2003). For example, Adebiyi and Kok (2020) recently showed that the coarse (≥5 μm) mineral dust component [which includes the size fraction feasible to be targeted in detrital single-grain analysis (>10 μm)] is substantially underestimated in climate models, yet has significant, specific, yet poorly constrained impacts on climate.

Atmospheric mineral dust (here referred to only as 'dust') acts as an agent of climate change by affecting the radiative balance of the planet, the chemical composition of the atmosphere, and cloud and precipitation patterns, while its deposition has impacts on the albedo of snow/ice surfaces, and biogeochemical and carbon cycles (e.g. Aoki et al., 2006; Coale et al., 1996; Maher et al., 2010; Martin, 1990; Reynolds et al., 2001; Shao et al., 2011; Tegen et al., 1996; Yin and Chen, 2007). Furthermore, dust not only acts as an agent of climate change, but variations in dust availability, transport, and deposition also respond to regional and/or global environmental changes, forming complex forcing and response feedbacks. As such, in order to better understand the climate system generally, and to improve projection of future climate and atmospheric circulation, improved global and regional climate models are needed that have better constrained atmospheric dust parameters and dust activity. While monitoring of current dust activity is a crucial part of this, testing the full range of dust-climate interactions requires constraining dust activity in the past. Provenance research of atmospheric dust in ancient aeolian silt (loess and 'Red Clay') deposits is one of the few ways to investigate past atmospheric circulation patterns and dust generation (especially coarse dust), and provides much needed information on the interactions between climate, tectonics, and dust. Knowledge of past dust emission areas, transport mechanisms and deposition is also relevant for making improved palaeoclimatic reconstructions from the loess climate proxy records.

The Chinese Loess Plateau (CLP) is a globally exceptional terrestrial archive of past atmospheric mineral dust. It covers a ~ 440,000 km^2 area in North China (Fig. 1), and the thickness of the dust deposits can reach hundreds of meters. The dust deposits on the CLP and adjacent areas extend back into the late Oligocene-early Miocene (Guo et al., 2002b; Qiang et al., 2011) or even into the Eocene (Licht et al., 2014; Wasiljeff et al., 2020), making them the longest, near continuous record of climate change on land, and the accumulation of dust still continues today. Combined, this provides an enormous amount of geologic material to study Cenozoic environmental and landscape change, as well as dust activity. However, while significant advances have been made in understanding the sources of dust to the CLP in recent years, there is still much uncertainty about the relative importance of specific source areas

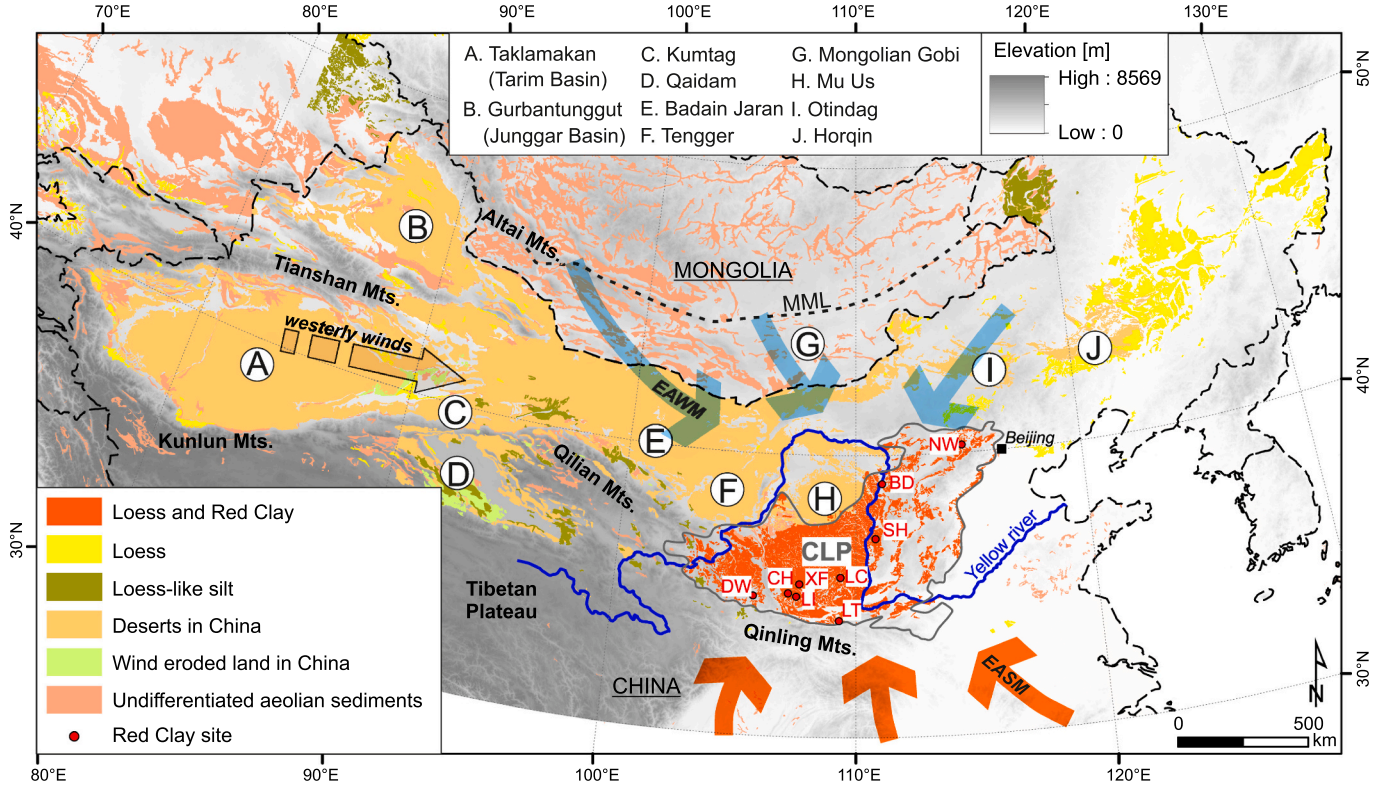

Fig. 1. The location of the Chinese Loess Plateau (CLP), Yellow River, and potential source areas to the Red Clay and loess, as well as sites mentioned in the text. The distribution of Neogene-Quaternary loess and Red Clay, loess-like silt, and undifferentiated aeolian sediments are modified from Börker et al. (2018). The Miocene-Pliocene Red Clay is most extensively distributed in the central CLP (An et al., 2014). The distributions of deserts and wind-eroded land in China are from 1:200,000 Desert Distribution Dataset provided by the Environmental and Ecological Science Data Center for West China, National Natural Science Foundation of China (http://westdc.westgis.ac.cn). EASM: East Asian summer monsoon. EAWM: East Asian winter monsoon. MML: Main Mongolian Lineament. Red Clay sites discussed in this paper: BD: Baode, CH: Chaona, DW: Dongwan LC: Luochuan, LI: Lingtai, LT: Lantian, NW: Nihewan, SH: Shilou, XF: Xifeng. (For interpretation of the references to colour in this figure legend, the reader is referred to the web version of this article.)

over the Cenozoic (e.g. Licht et al., 2016; Nie et al., 2018; Zhang et al., 2018a; Zhang et al., 2021a). The use of U-Pb dating of single detrital zircon grains in particular has revolutionised studies of dust provenance on the CLP (e.g. Bird et al., 2015; Nie et al., 2014a, 2015, 2018; Shang et al., 2016; Stevens et al., 2010, 2013; Zhang et al., 2016a, 2018a; Zhang et al., 2021a) yet the U-Pb ages of zircons from various source terranes overlap, making further refinement problematic (e.g. Fenn et al., 2018). Furthermore, these studies require a firm basis in understanding the crustal evolution of East Asia in the context of zircon formation and sediment provenance interpretations, yet such a wide scale synthesis is lacking in the literature. This uncertainty is particularly marked in the late Neogene CLP sediments, known as the Red Clay (RC) deposits, for which considerable debate still exists surrounding their provenance. The late Neogene can be considered as a potential analogue for future warmer climates (de la Vega et al., 2020). During the late Neogene, the mean global temperature was ~2–4 °C higher than modern values (Dowsett et al., 2013; Lunt et al., 2010; Sloan et al., 1996), but the tectonic setting and topography of East Asia were already similar to what they are today.

As such, in this paper, we address these gaps by 1) synthesizing understanding of the geologic background of potential primary source areas of the late Neogene CLP dust, which enables clear identification of key features that both facilitate and complicate single-grain provenance interpretations; 2) compiling existing single-grain provenance datasets as well as; 3) reviewing past Neogene dust provenance work on the CLP in order to reveal the current understanding from existing studies; and 4) testing a new combined single-grain zircon age and rutile geochemistry provenance approach that aims to utilise both crustal formation age and metamorphism information to assign dust sources and thereby greatly refine future provenance interpretations of dust to the CLP.

Our overview of the geologic background of the potential primary source areas of the CLP dust is aimed at facilitating more effective use of this information in provenance research, especially through use of established and novel single-grain methods. Knowledge of this geologic background is essential in interpreting the protosource information from detrital mineral studies, particularly where data from secondary (sedimentary) sources are scarce. We define primary source areas as the areas where the detrital minerals initially crystallized, i.e. the high-altitude orogens that provide dust material to the low-altitude sedimentary basins and river systems (secondary sources), as described by Sun et al. (2020). We also consider the crystalline bedrock underlying the secondary sources as primary sources. The mineral grains that have been deposited on the CLP cache information on their formation and alteration in these primary rocks (e.g. age or metamorphic temperature) and this information can be used in single-grain provenance work. After this we aim at illustrating the effectiveness of a new multi-proxy provenance approach using the chemistry of detrital rutile grains, in combination with U-Pb ages of detrital zircons, using examples from the late Neogene CLP RC sediments. Although the focus of this paper is on the late Neogene CLP sediments, it can be used as a general guide for sourcing CLP sediments of any age.

2. The Neogene Red Clay deposits and their provenance

The aeolian Neogene RC and Quaternary loess-palaeosol deposits on the CLP formed under the influence of the East Asian Monsoon system. The East Asian Winter Monsoon (EAWM) and the westerly winds (all winds deriving from the west to the CLP, not only the high-level westerly jet stream) transported dust to the CLP during the cold and dry winter seasons, while the East Asian Summer Monsoon (EASM), originating from the equatorial ocean, brought heavy rains during the summer season. During the late Neogene, the EASM was likely intensified (e.g. Ding et al., 1999; Ren et al., 2020), possibly even stronger than present (Farnsworth et al., 2019), triggering intense weathering and pedogenic modification. The RC deposits indeed exhibit higher levels of pedogenesis and, possibly also because of the warmer late Neogene climate (Nie et al., 2014b), furthermore have a stronger reddish colour than the Quaternary loess-palaeosol sediments. While some authors have suggested combined alluvial and aeolian deposition on mudflats for the RC formation (Alonso-Zarza et al., 2009; Meijer et al., 2020), the consensus is that the bulk of the RCs consists of sub-aerially deposited aeolian dust similar to the Quaternary loess (e.g. Ding et al., 1998a; Guo et al., 2001; Miao et al., 2004; Qiang et al., 2011; Sun et al., 1998).

The CLP lies downwind of the modern upper Yellow River (YR) channel-floodplain, numerous mountain belts, and arid regions in northern China and southern Mongolia (Fig. 1). All these areas may have been active dust sources over the Cenozoic. The increase in dust accumulation on the CLP during the Neogene has been linked with the aridification of inland Asia and the growth and expansion of Asian dust sources. These have likely been driven by the combination of global Cenozoic cooling, uplift of the Tibetan Plateau (TP), the retreat of the Paratethys Sea, as well as changes in the mid-latitude westerly and Asian monsoon circulation (An et al., 2001; Guo et al., 2002b; Lu et al., 2010, 2019; Ramstein et al., 1997; Rea et al., 1998). Regional tectonics have also been thought to be significant factors in controlling dust accumulation on the CLP, both by strengthening the East Asian monsoon system (An et al., 2001), which can increase erosion in the source areas (Nie et al., 2018), and also by providing a stable depositional basin as the basement of the CLP (Wang et al., 2018).

Several late Neogene episodes related to changes in the dust cycle in central-eastern Asia can be identified from the sediments in the central Asian dry lands and/or on the CLP:

1) ca. 8–7 Ma: the onset of widespread RC deposition in the most parts of the CLP (Ding et al., 1998a; Sun et al., 1998; Wang et al., 2018), the expansion of Asian dust sources and aridification of Asia (e.g. An et al., 2001; Sun et al., 2009; Lu et al., 2010; Zhang et al., 2018a).
2) ca. 5.3 Ma (Miocene-Pliocene boundary): Global climate change that further expanded the Asian dust sources at the Miocene-Pliocene boundary (e.g. Sun and Liu, 2006). This boundary is well expressed in the RC sequences of the Baode area in northern CLP, where the late Miocene Baode Formation and the Pliocene Jingle Formation differ in e.g. colour and fossil record (Zhu et al., 2008).
3) ca. 3.6–3.3 Ma: Expansion of Northern Hemisphere ice sheets and/or tropical forcing of aridification leading to a cooler and drier climate (e.g. An et al., 2001; Guo et al., 2002b;; Lu et al., 2010; Su et al., 2019a), which increased dust availability and transport to the CLP. The EASM was possibly intensified during this time interval (An et al., 2001; Ren et al., 2020), triggering increased erosion and dust availability in source areas (Nie et al., 2018). Recent evidence also points to relatively weaker westerlies, indicated by decreased dust fluxes to the CLP and the North Pacific Ocean, before the intensification of the Northern Hemisphere glaciation at ca. 2.7 Ma (Abell et al., 2021).
4) ca. 2.7–2.6 Ma (Pliocene-Pleistocene boundary): Another episode when Northern Hemisphere glaciations became enhanced (e.g. An et al., 1999; Ding et al., 2000; Haug et al., 1999; Lu et al., 2010), and subsequently increased dust availability and transport to the CLP, as represented by the shift from RC to loess deposition.

Provenance research of the RC deposits allows us to better understand the spatiotemporal variations in the late Neogene wind systems, the controls on dust emission, and the tendency of dust producing areas to generate silt, and allow investigation of the causes of these shifts in late Neogene dustiness over the CLP. There have been extensive studies into the provenance of aeolian dust deposits on the CLP, using a variety of techniques and provenance tracers. High mountains and arid lands in northern and western China, southern Mongolia, and adjacent areas are likely the most crucial in terms of dust production and storage that subsequently feeds deposits on the CLP. Northeastern China cannot be excluded from these potential source areas, although it probably plays a minor role as a source for the Neogene dust (Shang et al., 2016). At least

in the Quaternary, the YR has most likely also acted as an important transport medium, bringing sediments from the Northern TP and depositing on floodplains and alluvial platforms closer to the CLP, where they were subsequently deflated and wind-transported to the final deposition place on the CLP (Nie et al., 2015; Stevens et al., 2013).

Despite this general consensus, there is considerable debate about the specific sources and temporal changes in source of the late Neogene RC. While several detrital zircon U-Pb studies have been able to detect temporal variations in the provenance of the late Neogene RC deposits (Gong et al., 2017; Nie et al., 2018; Shang et al., 2016), bulk sediment/whole rock provenance studies have not been able to distinguish those variations, at least not from the RC units younger than ca. 7 Ma (e.g. Bird et al., 2020; Chen and Li, 2013; Nie et al., 2013). Detrital mineral single-grain provenance proxies are in most cases able to distinguish multiple different sources to a single deposit, which makes them ideal to use on CLP sediments, which most likely receive material from mixed sources. However, hypothetically, if detrital zircon ages were used alone in sourcing the CLP dust, as has frequently been the case, it may lead to ambiguous provenance interpretations and leaves metamorphic source area signals underrepresented (Section 3). For example, the detrital zircon age distributions of most the potential source areas and of almost all the aeolian sediments on the CLP include the same double peaks in the 500–400 Ma and 300–200 Ma age ranges (Section 7). Additionally, potential dust sources in the north and west, such as the Qaidam and Tarim Basins, and the Northern TP, often share a high peak in early Palaeozoic zircon ages, which may make it difficult to distinguish these sources from one another based on zircon age distributions alone. Various methods have been used to attempt to differentiate between these age distributions, such as high grain analysis numbers accompanied with quantitative statistical analysis of source area contributions (Licht et al., 2016; Zhang et al., 2021a), or with comparison of prominent age clusters (Nie et al., 2018), grouping source area age data based on their tectonic origin (Zhang et al., 2016a) or proximity to the CLP (Zhang et al., 2018a), as well as other statistical approaches like multidimensional scaling (MDS; Vermeesch, 2013). Although these approaches help in source assignments, ambiguities remain when multiple sources share the double peaks even if in different proportions. While high-*N* detrital zircon data provide more possibilities for quantitative and more reliable provenance interpretations than low-*N* data, fundamentally it is impossible to estimate the proportional influence of each source age peak to the RC/loess double peaks unless assumptions are made a priori of mixing contributions (see methods above). Perhaps even more importantly, use of zircons alone also poses a potential fertility bias that leads to mafic igneous rocks and metamorphic rocks being underrepresented in these data sets (e.g. Chew et al., 2020). As a robust mineral that can survive multiple sedimentary cycles, the use of zircon also causes complexity when the source to sink route is not straightforward (Andersen et al., 2016).

While high-*N* detrital zircon U-Pb dating is arguably the best single approach for understanding dust sources to the CLP, the ambiguities of solely using detrital zircon age data in studying the provenance of the CLP sediments can potentially be overcome by multi-proxy single-grain provenance analysis. Indeed, Fenn et al. (2018) found that detrital zircon U-Pb dating alone was unable to detect source detail in Quaternary loess that could be revealed when zircon data was combined with detrital garnet geochemistry. As we outline below, other metamorphic minerals, such as detrital rutiles, also have potential in distinguishing sources that cannot be differentiated by zircon U-Pb dating, thus allowing considerable breakthroughs in assigning specific sources and source changes to the CLP.

3. Zircon and rutile as provenance tracers

Both zircon ($ZrSiO_4$) and rutile (TiO_2) are non-magnetic heavy minerals (densities 4.6–4.7 g cm^{-3} for zircon and 4.23–5.5 g cm^{-3} for rutile) and have tetragonal crystal structures. They are very stable both mechanically and chemically during weathering, transport, and diagenetic processes (Morton and Hallsworth, 2007), which allows them to preserve information from primary source rocks and makes them good targets for single-grain provenance work. Zircons form in various types of igneous and metamorphic rocks. Intermediate and felsic igneous rocks have higher concentrations of zircons than mafic igneous or metamorphic rocks, which may cause bias in detrital zircon provenance studies (Sláma and Košler, 2012). Rutile occurs mainly in high-grade (amphibolite to granulite facies) metamorphic rocks, but is also present in alkaline and hydrothermally or metasomatically altered igneous rocks, and, as an accessory mineral, in various other types of igneous and metamorphic rocks (Deer et al., 2013; Force, 1980).

The U-Pb method is widely used in geochronology because two decay series of uranium isotopes (^{238}U and ^{235}U to ^{206}Pb and ^{207}Pb, respectively) can be used that are linked via the constant $^{238}U/^{235}U$ ratio (137.88; Steiger and Jäger, 1977). Additionally, in e.g. zircon, the amount of the non-radiogenic isotope of Pb (^{204}Pb) at the time of crystallization is minimal, and does not increase afterwards, so the Pb present at the time of crystallization can be constrained. Another powerful feature of the U-Pb system is that the half-lives of the two isotopes are long enough to cover most of the Earth's history. The development of analytical methods has allowed faster analyses of zircon U-Pb ages and increased their use for provenance work that requires at least 117 (Vermeesch, 2004) or even 300—1000 (Pullen et al., 2014) analyses per sample to reliably interpret the population presence or absence, and relative size of age peaks. In the past decade or so, detrital zircon U-Pb dating has become the most prominent single-grain provenance method for different types of sediments. Since the initial work of Stevens et al. (2010), the technique has become widely used in provenance work on the CLP.

Rutile is the dominant carrier of high field strength elements (Ti, Zr, Nb, Hf, Ta) in rocks (e.g. Foley et al., 2000; Zack et al., 2002). In nature, titanium dioxide has two additional polymorphs: brookite and anatase, which are the low-temperature polymorphs of TiO_2, while rutile corresponds to higher pressures and temperatures (Meinhold, 2010). According to Triebold et al. (2011), the three TiO_2 polymorphs can be discriminated based on their V, Cr, Fe, and Nb contents, which is essential before applying other rutile geochemistry-based provenance applications.

Rutiles can also be dated with U-Pb isotopes, but there are two other major applications for provenance studies that are based on the trace element contents of rutile. One is Zr-in-rutile geothermometry, and the other is a source rock lithology characterization in terms of whether the protolith of the metamorphic source rock was pelitic or mafic. Zr-in-rutile thermometry is based on the fact that Zr content in rutile is highly temperature-dependent (Tomkins et al., 2007; Watson et al., 2006; Zack et al., 2004a), and on the assumption that rutile is in equilibrium with quartz and zircon during growth according to the equilibrium reaction $ZrSiO_4$ (zircon) = ZrO_2 (in rutile) + SiO_2 (quartz/coesite) (Ferry and Watson, 2007). There are several different Zr-in-rutile thermometers. Some require an input of the pressure conditions, which for detrital rutiles is impossible to know. The first Zr-in-rutile thermometer was introduced by Zack et al. (2004a) and did not require a pressure component. Watson et al. (2006) offered a revised thermometer that was also independent of pressure and Ferry and Watson (2007) took into account the activity of quartz. Tomkins et al. (2007) presented Zr-in-rutile thermometers that were pressure-dependent. As it is impossible to determine the metamorphic conditions of the source rocks for each detrital rutile, a systematic assumption of the conditions must be made. Triebold et al. (2012) suggest using the thermometer by Tomkins et al. (2007) with a default setting of 10 kbar and α-quartz. Triebold et al. (2012) argue that equilibrium with either α- or β-quartz is much more likely than with coesite, the high-pressure form of quartz, and that the difference between α- and β-quartz is very small. In general, the differences between the various Zr-in-rutile thermometers are relatively small and do not significantly change the

interpretation.

The lithological classification of the source rock protolith based on the Nb and Cr contents of rutiles was first introduced by Zack et al. (2002). Metamafic (−basic) rutiles show lower Nb and higher Cr contents than metapelitic rutiles. Triebold et al. (2007) later noticed that eclogites (high-pressure metamafic rocks) do not directly follow this discrimination and suggested a log(Cr/Nb) = 0 ratio as the discriminator of the two lithologies. Furthermore, Meinhold et al. (2008) added a lower limit of 800 ppm Nb for metapelitic rutiles. For provenance studies, Triebold et al. (2012) suggested yet another discrimination method: x = 5*(Nb[ppm] - 500) - Cr[ppm]. Using this equation, metamafic rutiles will yield negative values of *x* and metapelitic rutiles will yield positive values. Despite the development in the method, the Cr-Nb discrimination still cannot be used blindly, especially in cases where the Nb and Cr contents are low and the geological conditions have been unusual. Exceptions in such cases should be carefully reviewed. Kooijman et al. (2012), and Meyer et al. (2011) have shown that in some ultrahigh-temperature (UHT) granulites, the Cr-Nb discrimination is not completely valid and is disturbed by retrograde processes.

Despite its potential, rutile is less commonly used as a provenance proxy than zircon. In aeolian deposits, detrital rutile geochemistry has so far only been tested on European loess sequences (Újvári et al., 2013) and no rutile provenance studies of the CLP sediments have been published so far. Since both zircon and rutile are non-magnetic heavy minerals, they can be separated from the bulk sediment simultaneously with the same traditional separation methods, i.e. heavy mineral and magnetic separations. Furthermore, because rutile and zircon share similar physical properties (specific gravity, crystal system (shape), magnetic properties), it is likely that they share similar transport paths. This means that differences in provenance indicated from zircons and rutiles likely result from the types of primary source rocks that they can be traced to. Zircons likely have eroded from intermediate or felsic rocks, while rutiles probably originate from metamorphic rocks that may initially have been sedimentary or igneous rocks. Thus, with the two minerals, it is essentially possible to cover all major types of potential primary source rocks to some extent. In cases where two or more source areas share similar zircon age signals, rutile geochemistry has potential to distinguish those sources, if they have contrasting metamorphic histories.

However, the use of detrital zircon and rutile as provenance tracers requires good understanding of the tectonic and metamorphic histories of the primary dust source areas. This especially concerns the use of detrital rutile because there are no published rutile data from the presumed secondary (sedimentary) sources to the CLP. With the two minerals (and the information that they hold on the primary source rocks) in mind, in the next section we present geological background on northern, western and northeastern China, as well as southern Mongolia relevant to provenance interpretation. After that, we summarise previously published zircon U-Pb data from the potential secondary sources, and report previously published rutile geochemistry from the primary source regions. We also summarise previous single-grain provenance work done on the Neogene RC. Finally, in order to illustrate the potential of the joint zircon and rutile provenance method, and to utilise the compiled primary source region data, we then report and interpret new zircon and rutile provenance data from a ca. 4 Ma unit of Nihewan RC, located in the northern CLP. Our aims here are to provide a benchmark geologic background and rutile and zircon database for northern China-southern Mongolia that enables better interpretation of zircon age and rutile trace element data in terms of provenance on the CLP, and to demonstrate the potential of a combined zircon and rutile single-grain approach in making significant advances in understanding dust sources to the CLP.

4. Short geologic background of the primary source regions

The geology of China and Mongolia reflects their formation via multiple continental block collisions. The collisional history dates back to the Archean and still continues today as the Indian plate is colliding with the Eurasian plate. Although Precambrian rocks occur in most areas covered in this paper, Precambrian China can be divided into three major blocks: the North China Craton (NCC), Tarim Craton (TC), and South China Craton (Fig. 2), while Precambrian Mongolia consists of various microcontinental blocks of which most are in northern Mongolia (e.g. Badarch et al., 2002). Parts of the major Precambrian blocks and of other older continental fragments and tectonic elements in China have widely experienced ultrahigh-pressure (UHP) metamorphic conditions during the Phanerozoic (Stern et al., 2018). Coupled with abundant ophiolite belts and collisional orogenies, they mark the closure events of multiple pre-existing oceans (Stern et al., 2018). In fact, a major part of northern and western China, and of Mongolia, formed during Palaeozoic to Mesozoic closures of the Proto-Tethys (early Palaeozoic), the Palaeo-Tethys (early Mesozoic), and/or the Palaeo-Asian (late Palaeozoic to early Mesozoic) Oceans (e.g. Zhao et al., 2018 and references therein; Fig. 2). Most metamorphic terranes of the area correspond to these events.

Middle to Late Mesozoic igneous rocks in China and Mongolia are mainly related to the 'Yanshan Revolution' (or 'Yanshan Movement') that mostly affected areas in eastern China and Mongolia (Fig. 2 and Fig. 1 in Dong et al., 2015). The youngest tectonic events of the study region are related to the formation of the Tibetan-Himalayan orogen, which has predominantly affected the CLP sediments and their accumulation by changing the atmospheric circulation and climatic controls in the region through TP uplift (e.g. An et al., 2001), by reactivating older orogenic belts, which increases erosion from those primary sources, and by changing river drainage.

The current area of exposed metamorphic rocks in China accounts for one fifth of the land area (Geng et al., 2018). The abundance of metamorphic terranes in Northern China and adjacent areas gives rise to provenance work that focuses on the metamorphism of the source rocks, or in this case, the metamorphic temperatures recorded by rutile. All the previously published Zr-in-rutile temperatures from the primary source areas are listed in Section 8. In the following text, the term metamorphic facies is used to describe metamorphic conditions, which depend on both pressure and temperature. Consequently, it is impossible to set exact temperature limits for each metamorphic facies. However, some approximate temperature ranges of different metamorphic facies can be constructed. Here the division of the facies used by e.g. Zack et al. (2004b) is followed: <500 °C for greenschist/blueschist facies, 500–750 °C for amphibolite/eclogite facies, and > 750 °C for granulite facies. Granulite facies rocks can be further classified as high-temperature (HT) or UHT rocks if their formation temperature exceeds 800 °C or 900 °C, respectively. It is also possible to have high-pressure (HP)/UHP rocks (blueschist or eclogite facies), especially in subduction zones where the subducting plate can reach considerable depths. HP/UHP rocks, however, do not necessarily have high formation temperatures. These are essential distinctions to make in using rutile palaeothermometry in provenance work, and to aid future interpretations we summarise the state of the art of these aspects below.

As this review aims to describe northern China-southern Mongolia geologic history with a focus on provenance studies on the CLP, and for clarity, the divisions of the terranes in this paper may not be consistent with other divisions made in previous studies that focus solely on the geological history and processes in the study region. The complexity of the regional geology has also made occasional simplification of the terrane descriptions unavoidable, which may have led to some information not being fully reported here. The next two sections describe the primary source areas. Firstly, geochronology, which aids provenance interpretations made from detrital mineral formation ages, and secondly, metamorphic temperatures, which help provenance inferences made from metamorphic detrital minerals. In addition to short summaries at the end of Sections 5 and 6, the primary source region data discussed in the following sections are also compiled in Table 1.

Table 1
Summary of the primary source region data discussed in Sections 5 and 6.

Potential source region	Primary source terranes	Metamorphic T [°C]	HT/UHT metam. T [°C]	Ages (of crystalline rocks)						
				<200 Ma	200–300 Ma	300–400 Ma	400–540 Ma	0.54–1.0 Ga	1.0–2.5 Ga	≥2.5 Ga
Western China distal sources	Tarim Craton & Tarim LIP	300–400[1] & 660–700[2]	800–860[3]		280–300[4]			0.7–1.0[5,6,7]	1.8–2.5[8,9,10,11]	2.5–2.6[7,11]
	West Kunlun	620–720[12]	800–820[12]		214[13]		405–471[13]			
	South Tianshan	<580[14]	800–960[15]		270–290[16]	320–420[16]				
	Altyn Tagh	~600–800[17,18,19]	800–870[19] & ~950[18]				450–510[20]	0.90–0.94[21]	1.1–2.3[6,21]	2.6–3.6[6]
Northwestern China distal sources	Junggar				270–300[16]		510[22]		1.85[22]	
	Central Tianshan	<500[16] & 750–800[23]	800–840[23]		250–300[16]	300–400[16]	400–500[16]	0.8–1.0[16]	1.0–1.45 & 1.8[16]	2.5[16]
	North Tianshan				260–300[16]	300–400[16]	400–450[16]			
	Yili	low- and high-grade rocks[16,24]			260–300[16]	300–400[16]	400–470[16]	0.85–0.93[16]		
	Chinese Altai	<780[25–28]	~980[25]		260–290[25]	365–390[25,28,29]	410–541[29]	0.54–0.92[29]		
Central China (West of CLP) sources	Qaidam		910–1010[30]		240–290[31]	380–400[31]	400–470[31]	0.92 & 0.96[31]		
	North Qaidam UHP Belt	<650[32]–800[33,34]	800–880[32,33] & 960–1040[35]				400–460[33]			
	East Kunlun Orogen	535–770[36–38]			220–250[39]		400–540[39]	0.95–1.0[39]	1.0–2.2[38]	2.5–2.7[38]
	Qilian orogen (Qilian Block & North Qilian Orogen)	420–557[34,40,41] (NQO)				ca. 370–400[42]	400–520[38,39,42]	ca. 0.9[43]		
	Songpan-Ganzi	low-grade rocks[44]		150–200[45,46]	200–230[45,46]					
Northern China, Southern Mongolian (NW of CLP) sources	Beishan	~600 & 730–800[47]	800–840[47]		ca. 300[48]	340–400[48,49]	400–500[48,49]	0.7[48] & 0.9–1.0[50]		
	Northern Alxa	~ < 750[51]			270–300[52]	360–370[51]				
	CAOB terranes in S Mongolia	~ < 750[53]		ca. 150–200[53,54]	ca. 250–300[53,54]	300–400[53,54]	400–540[53–55]	ca. 0.9–1.0[55–57]		
NE China sources	Southern orogen	<500[58]			ca. 240–280[59]		ca. 450[59]			
	Northern orogen	<790[60]			ca. 230–300[59]	ca. 300–340[59]	ca. 420–520[59]			
	NE China & NE China Khondalite Belt	~650[61]	<850[61]	ca. 130 & 190[62]	ca. 250[62]	ca. 320[62]	ca. 450–540[62,63]	ca. 0.65–1.0[63]	1.7–1.98[63]	2.5–2.8[63]
Sources south of CLP	Qinling	~700[64]	880–920[65]	100–200[66,67]	200–300[66,67]		400–510[66,67]	0.7–1.0[66,67]		
	Dabie	680–800[68,69]	800–830[68] & 930[69]	125–135[70]	200–240[71]			0.75[71]	ca 1.8–2.0[71]	ca. 2.5[71]
Sources east of CLP	Sulu				220–230[71]			ca. 0.75[71]	1.8–2.0[71]	2.5[71]
	Eastern NCC	<750[72]	~840–1150[72]						ca. 1.9–2.2[72,73,74]	2.50–2.55 & 2.7–2.8[75]
Proximal sources	TNCO	~740–800[76]	800–930[76,77]						ca. 1.8–2.5[74,78–80]	
	W NCC	~600–800[81]	850–1000[81,82] (KB)						ca. 1.92–1.95[74,83–84]	2.50–2.55 & 2.7–2.8[75]

References: 1. Zhang et al. (1999); 2. Ge et al. (2016); 3. Zhang et al. (2012b); 4. Xu et al. (2014); 5. Ge et al. (2014a); 6. Lu et al. (2008); 7. Zhang et al. (2013); 8. Wang et al. (2014a); 9. Zhu et al. (2011); 10. Ge et al. (2013a); 11. Ge et al. (2014b); 12. Qu et al. (2007); 13. Yuan et al. (2002); 14. Gao et al. (1999); 15. Wang et al. (1999); 16. Han and Zhao (2018) and references therein; 17. Dong et al. (2018a); 18. Zhang et al. (2014a); 19. Liu et al. (2012a); 20. Liu et al. (2010); 21. Wang et al. (2013); 22. Zhou et al. (2018); 23. Mao et al. (2015); 24. Wang et al. (2014b); 25. Liu et al. (2020a); 26. Jiang et al. (2015); 27. Wei et al. (2007); 28. Jiang et al. (2010); 29. Windley et al. (2002); 30. Teng et al. (2020); 31. Cheng et al. (2017) and references therein; 32. Zhou et al. (2019); 33. Zhang et al. (2008); 34. Zhang et al. (2010); 35. Song et al. (2004); 36. Liu et al. (2005); 37. Meng et al. (2013); 38. Song et al. (2018); 39. Dong et al. (2018b) and references therein; 40. Song et al. (2007); 41. Zhang et al. (2007); 42. Song et al. (2013b); 43. Wan et al. (2001); 44. Yin and Harrison (2000); 45. Roger et al. (2004); 46: Zhang et al. (2014b); 47. (Zong et al., 2017); 48. Song et al. (2013a); 49. Xiao et al. (2010); 50. Liu et al. (2015a); 51. Zhao et al. (2020); 52. Liu et al. (2017); 53. Badarch et al. (2002) and references therein; 54. Taylor et al. (2013); 55. Demoux et al. (2009); 56. Wang et al. (2001); 57. Yarmolyuk et al. (2005); 58. Zhang et al. (2016b); 59. Eizenhöfer and Zhao (2018) and references therein; 60. Zhang et al. (2018b); 61. Zhou and Wilde (2013) and references therein; 62. Wu et al. (2011); 63. Zhou et al. (2018) and references therein; 64. You et al. (1993); 65. Bader et al. (2013) and references therein; 66. Dong et al. (2011) and references therein; 67. Dong and Santosh (2016) and references therein; 68. Zhang et al. (1996); 69. Lei et al. (2020); 70. Li et al. (2010); 71. Hacker et al. (2006); 72. Cai et al. (2020); 73. Zhao et al. (2012); 74. Zhao et al. (2005); 75. Zhao and Cawood (2012); 76. Wang et al. (2020); 77. Guo et al. (2002a); 78. Wang et al. (2010); 79. Trap et al. (2012); 80. Tang and Santosh (2018); 81. Jiao et al. (2011); 82. Zhao et al. (1999); 83. Santosh et al. (2007a); 84. Santosh et al. (2007b).

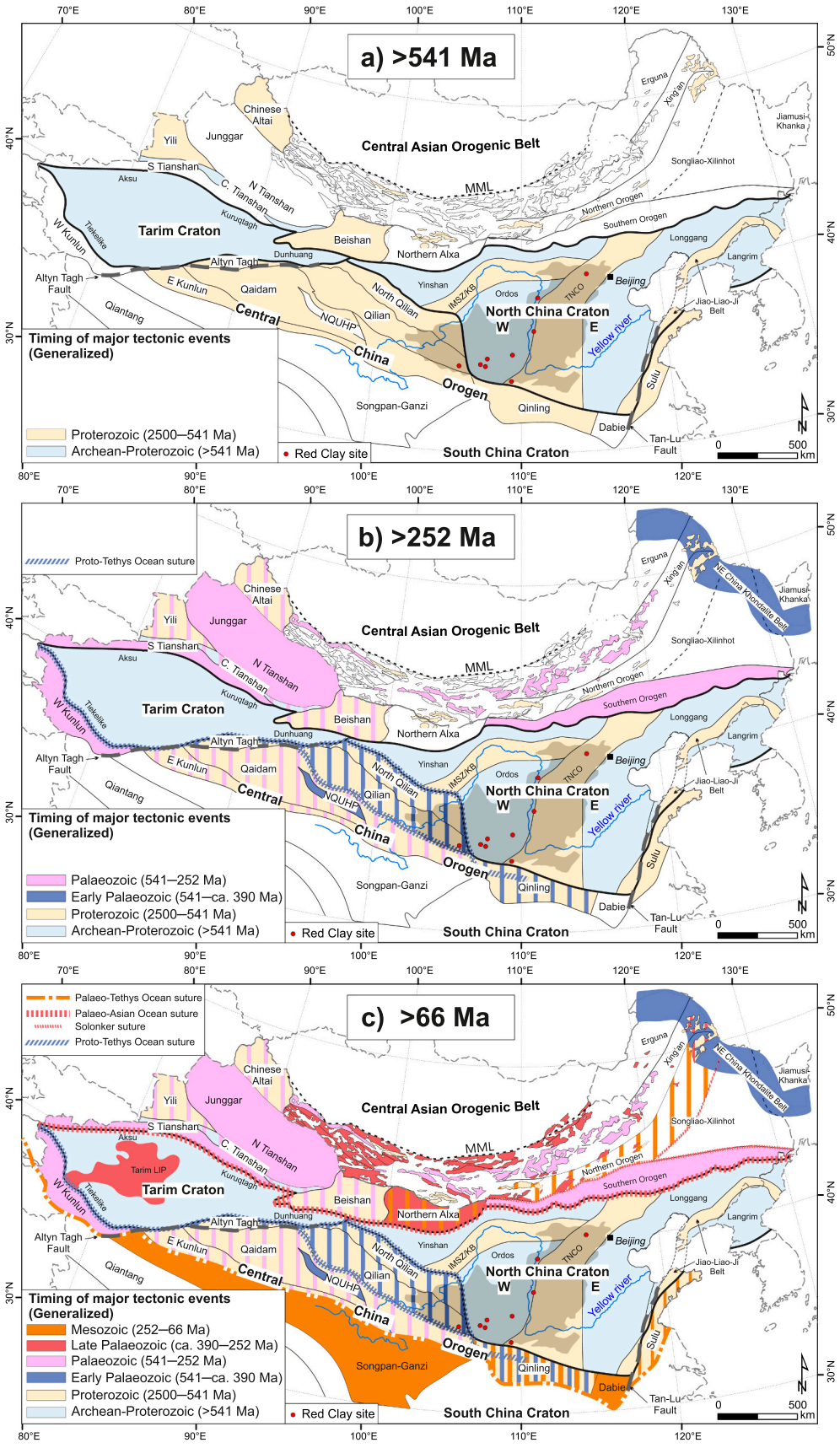

Fig. 2. A simplified map of geologic terrane ages in northern China, southern Mongolia, and parts of the Korean Peninsula. A) The oldest terranes with relatively abundant Archaean rocks, accompanied with records of Proterozoic activity, are the North China Craton, Tarim, and Central Tianshan. The North Altyn Tagh and East Kunlun also include Archaean rocks, but the Precambrian rocks are mostly Proterozoic. In addition to Central Tianshan, the Central Asian Orogenic Belt (CAOB) also includes other Precambrian (mostly Meso- to Neoproterozoic) terranes that later amalgamated with other tectonic fragments to form the CAOB. B) The terranes in Central China Orogen (CCO) were active during the early Palaeozoic closure of the Proto-Tethys Ocean. Some of the tectonic fragments in the CAOB were active during early Palaeozoic orogenic events. C) Most of the CAOB in northern China and southern Mongolia was affected by the late Palaeozoic to early Mesozoic closure of the Palaeo-Asian Ocean. In the CCO, the early Mesozoic closure of the Palaeo-Tethys Ocean affected the southern and eastern parts of the region. During the late Mesozoic, especially the eastern parts of the whole study region were also affected by the Yanshan Revolution. Terrane boundaries and sutures are drawn after Badarch et al. (2002), Eizenhöfer and Zhao (2018), Han and Zhao (2018), Liu et al. (2017), Parfenov et al. (2004), Xiao et al. (2010), Yang et al. (2007), Zhao et al. (2005, 2018), Zhou and Wilde (2013), Zhou et al. (2018), and Zhou et al. (2019). Shaded area marks the Chinese Loess Plateau. IMSZ: Inner Mongolia suture zone. KB: Khondalite Belt. MML: Main Mongolian Lineament. NQUHP; North Qaidam UHP Belt. W(E): Western (Eastern) Block of NCC. Information on the Red Clay sites in Fig. 1. (For interpretation of the references to colour in this figure legend, the reader is referred to the web version of this article.)

5. Geochronology of the primary source regions

5.1. North China Craton

The oldest rocks of Asia are found in the eastern North China Craton (NCC: also known as the Sino-Korean Craton in the literature), and date back to ca. 3.8 Ga (Wan et al., 2012). Despite the occurrence of some Eoarchean rocks, most Archean rocks in the NCC are Neoarchean, having formed during two magmatic events at 2.8–2.7 Ga and 2.55–2.50 Ga (Zhai and Zhou, 2015; Zhao and Cawood, 2012). The NCC itself consists of two Archean blocks, the Western and Eastern Blocks, which are divided by the Palaeoproterozoic (ca. 2.5–1.8 Ga) Trans-North China Orogen (TNCO; Fig. 2) (e.g. Wang et al., 2010; Trap et al., 2012; Tang and Santosh, 2018 and references therein; Zhao et al., 2000, 2005, 2008). The TNCO has recorded major rock-forming events at ca. 2.5 Ga, ca. 2.1 Ga, and during the final collision of the Western and Eastern Blocks at ca. 1.9–1.8 Ga (e.g. Trap et al., 2012; Tang and Santosh, 2018 and references therein; Wang et al., 2010; Zhao et al., 2005, 2008). The Western Block is further divided into Yinshan and Ordos Blocks by the ~east-west trending Palaeoproterozoic (ca. 1.95–1.92 Ga; Zhao et al., 2005; Santosh et al., 2007a, 2007b) Inner Mongolia Suture Zone (IMSZ). The CLP is located mostly on the Ordos Block and the TNCO. The Lüliang Complex (Mts.) which is close to the Shilou RC (Figs. 11 and A1), mostly records tectonic events of ca. 1.88–1.82 Ga, and other events at ca. 2.2 Ga, 2.1 Ga, and 1.95–1.9 Ga (Liu et al., 2006; Tang and Santosh, 2018 and references therein). The Eastern Block of the NCC is also divided into two blocks, Longgang and Langrim, separated by a Palaeoproterozoic orogenic belt, the ca. 2.2–1.9 Ga Jiao-Liao-Ji Belt (Zhao et al., 2005, 2012 and references therein; Cai et al., 2020 and references therein).

5.2. Tarim Craton and Altyn Tagh

The TC is mostly covered by the Cenozoic sediments of the Taklamakan Desert (Sun et al., 2009; Zheng et al., 2015), and the exposed basement rocks can only be found on its margins. The desert, which possibly acts as a distal western source for the aeolian CLP sediments, is surrounded by several mountain belts: the Tianshan Mts. to the north, the western Kunlun Mts. to the south, and the Altyn Tagh Mts. to the southeast. The exposed basement rocks can be divided into five blocks (clockwise from the north- to southwest): Aksu, Kuruqtagh (Kuruktag, Quruqtagh or Kuluketage), Dunhuang, North Altyn Tagh, and Tiekelike (Tiekelike uplift or the North Kunlun Terrane) Blocks (Fig. 2). The Precambrian evolution of TC is still debated, although the Proterozoic linkages to the assembly and breakup of the supercontinents Columbia/Nuna and Rodinia are agreed upon (e.g. Ge et al., 2014a, 2016; Lu et al., 2008; Shu et al., 2011; Wang et al., 2013; Zhang et al., 2013). The North Altyn Tagh, which is the northern/northeasternmost part of Altyn Tagh orogen, is considered to belong to the Archean-Palaeoproterozoic basement of the TC, but the rest of Altyn Tagh is commonly treated separately (e.g. Lu et al., 2008; Wang et al., 2013; Zhao and Cawood, 2012).

Archean rocks in TC, most of which formed at ca. 2.6–2.5 Ga, are mainly found on the eastern and northern margins of the craton, from the Kuruqtagh and Dunhuang Blocks, and North Altyn Tagh (Ge et al., 2014b and references therein; Lu et al., 2008; Zhang et al., 2013 and references therein, Zhao and Cawood, 2012 and references therein). The prevailing cratonic basement rocks, however, are Palaeoproterozoic mafic-felsic intrusions and high-grade metamorphic rocks, and Meso- to Neoproterozoic low-grade metasedimentary and volcanic strata (Lu et al., 2008; Stern et al., 2018; Zhao and Cawood, 2012).

Major Palaeoproterozoic tectonothermal events in the eastern and southern margin of the TC (Dunhuang, and Tiekelike Blocks, and North Altyn Tagh), as well as in the western tip of the Yinshan Block in the NCC (Alxa Block), are almost coeval, at ca. 2.5–2.2 Ga and 2.1–1.8 Ga, and probably related to the assembly of the Columbia/Nuna supercontinent (Wang et al., 2014a and references therein). Also in the NE margin of TC in Kuruqtagh, magmatic events at 2.47 Ga have been reported (Shu et al., 2011), and major metamorphic events occurred at ca. 2.0–1.8 Ga (Ge et al., 2013a; Ge et al., 2014b). Detrital zircons from (meta)sedimentary rocks in the Aksu Block in the NW TC suggest that a Palaeoproterozoic (ca. 2.0–1.8 Ga) orogeny extended to this region as well (Zhu et al., 2011).

The Kuruqtagh and Tiekelike Blocks in the NE and SW TC, respectively, as well as the southern parts of Altyn Tagh, have recorded late Mesoproterozoic to early Neoproterozoic orogenic events (ca. 1.0–0.9 Ga) and subsequent rifting events (ca. 0.9–0.7 Ga) that have been linked with assembly and break-up of the Rodinia supercontinent (e.g. Ge et al., 2014a; Lu et al., 2008; Wang et al., 2013; Zhang et al., 2013). In the NW margin of TC, the Aksu Group, which consists of mafic green- and blueschists, and metasedimentary rocks, formed in a Neoproterozoic active margin where the HP blueschist metamorphism likely occurred between ca. 730–700 Ma (Zhu et al., 2011), although some suggest an earlier age of before ca. 760 Ma (Zhang et al., 2013). The Precambrian basement of the TC is covered by Neoproterozoic to Cambrian sedimentary sequences that are preserved in both northern and southern parts of the TC (Zhang et al., 2013). They are particularly well exposed in the Aksu Block in the NW margin of TC, where the late Neoproterozoic Sinian sedimentary rocks have a maximum depositional age of ca. 602 Ma (Zhu et al., 2011).

The southern margin of TC collided with the Qiantang Block forming the West Kunlun in the Early Palaeozoic (Section 5.3). Parts of Altyn Tagh were also metamorphosed in an Early Palaeozoic collisional orogenic event that manifests itself in ca. 510–450 Ma high-grade (HP-UHP) metamorphic rocks (Liu et al., 2010, 2012a; Wang et al., 2013). The northern margin of TC on the other hand amalgamated with the southwestern part of the Central Asian Orogenic Belt (CAOB) in the late Palaeozoic during the Tianshan orogen (Section 5.4). TC has also recorded late Palaeozoic plume activity. The Tarim Large Igneous Province (LIP) that extends over a $>$ 250,000 km^2 wide area in the central and western parts of the craton (Fig. 2), formed in three stages at around 300–280 Ma (Xu et al., 2014).

5.3. Central China Orogen

The E-W trending Kunlun-Qilian-Qinling-Dabie-Sulu orogenic belts start from southwestern TC and spread out all the way to eastern China (Fig. 2), together also called the Central China Orogen (CCO). The CCO formed during closure of the Proto-Tethys Ocean, but some parts have also recorded the closure of the Palaeo-Tethys Ocean (Zhao et al., 2018 and references therein; Fig. 2). To the south of the TC, the West and East Kunlun Blocks/Mts./orogenic belts are separated by the Altyn Tagh Fault (Fig. 2). The West Kunlun acts as a potential distal western (primary) source to the CLP sediments via the Tarim Basin/Taklamakan Desert, but likely also blocks any major dust transport from further west. The West Kunlun formed in two stages of subduction-collision between the TC and Qiantang Block: first, in the closure of the Proto-Tethys, that lasted from mid-Ordovician to late Ordovician followed by postcollisional early Devonian events, and secondly, in the closure of Palaeo-Tethys from early Permian to the late Triassic (Yuan et al., 2002; Zhao et al., 2018 and references therein).

Compared to the West Kunlun and TC, the East Kunlun Orogen (EKO), the Songpan-Ganzi complex (SGC), the Altyn Tagh Mts., the Qaidam Block, and the Qilian Mts. (Fig. 2) act as more proximal primary western source regions to the CLP sediments via the Qaidam Basin or proximal deserts and, in the eastern parts, via the YR. They are located in the northern margin of the TP. Despite a sporadic occurrence of Triassic-Jurassic (ca. 230–150 Ma) granites (e.g. Roger et al., 2004; Zhang et al., 2014b), the SGC differs from the other areas in that, instead of crystalline rocks, it consists mostly of Triassic flysch sediments that are intensely deformed and/or metamorphosed in low-grade conditions (e.g. Yin and Harrison, 2000). The Triassic sediments of the SGC were

sourced from the north (EKO, NCC), east (Qinling-Dabie orogenic system), and south (South China Craton) of the complex (Enkelmann et al., 2007; Weislogel et al., 2006; Yin and Harrison, 2000), which suggests that detrital zircons from the SGC have a wide age range (see Section 7). The SGC is included in this review, because the YR starts from the complex, and some detritus may therefore have been transported downstream in the river and eventually ended up to the CLP. However, it is unlikely that the SGC has acted as a major source for the aeolian CLP sediments and it is uncertain if the YR had formed already in the Neogene.

All the areas north of the SGC in the CCO have a strong early Palaeozoic age component (Fig. 2), but the geologic history extends back to the Proterozoic. The EKO formed during collision of the Qiangtang and Qaidam Blocks (Dong et al., 2018b), but the tectonic history of EKO is complex and not well understood. Although the basement of the EKO includes various Proterozoic metamorphic rocks, the major part of the block consists of widespread ophiolites and other subduction-related rocks that have formed during the early Palaeozoic (ca. 500–400 Ma) (Dong et al., 2018b; Stern et al., 2018). Parts of the EKO also record the closure of the Palaeo-Tethys Ocean in Triassic Period (Dong et al., 2018b).

Between the EKO in the south, the Altyn Tagh Mts. in the northwest, and the Qilian Mts. in the northeast, lies the Qaidam Block (Fig. 2), whose basement rocks reflect the tectonic history of those three orogenic belts (Cheng et al., 2017). The major age groups of the plutonic rocks of the Qaidam basement are early Neoproterozoic (955 Ma and 916 Ma), early Palaeozoic (470–380 Ma) and late Palaeozoic to Mesozoic (290–240 Ma) (Cheng et al., 2017 and references therein). The Qaidam Block collided with the Qilian Block during Ordovician-Silurian time (ca. 450 Ma), forming the North Qaidam UHP Belt (NQUHP; e.g. Zhang et al., 2008).

Further north, the Qilian Orogen can be subdivided into the North Qilian Orogen (NQO) and the Qilian Block (Fig. 2). According to Song et al. (2013b) the Qilian Orogen records tectonic events from the Neoproterozoic breakup of the supercontinent Rodinia to the closure of the Qilian Ocean (potentially part of the Proto-Tethys Ocean) at ca. 445 Ma, and to the subsequent mountain-building in the late Silurian and Devonian. Eventually, in the late Devonian, post-orogenic extension resulted in the collapse of the Qilian orogenic belt, and in the Carboniferous, marine sedimentary deposits formed in the NQO until the India-Asia collision in the Cenozoic started to re-activate the mountains (Song et al., 2013b).

The eastern parts of the CCO that are located south and (south)east of the CLP, include the Qinling Orogenic Belt (QOB) and the Dabie-Sulu orogenic belt (Fig. 2). The latter is usually not considered as a source region for the CLP sediments, but because it is part of the CCO and located relatively close to the CLP, it is briefly discussed here. Because of its proximity, the QOB, on the other hand, has likely provided material at least to the southern CLP (Zhang et al., 2018a). The QOB, which forms the mountain belt that separates North and South China and broadly acts as the southern boundary of the CLP, formed in the collision between the NCC and South China Craton (Dong and Santosh, 2016 and references therein; Dong et al., 2011 and references therein). According to Dong and Santosh (2016), four distinct accretion and collision events occurred in the QOB: 1) the ca. 1.0 Ga Grenvillian orogeny, 2) a Neoproterozoic subduction/accretion, 3) two-stage subduction during the early Palaeozoic and late Palaeozoic, and 4) the late Triassic collision between the South China Craton and the southern part of the QOB. Even later, Early Jurassic to Cretaceous and Palaeogene tectonics evolved the QOB into an intra-continental orogen (Dong and Santosh, 2016; Dong et al., 2011). The age peaks from the igneous rocks from the QOB correspond to these events: ca. 950–900 Ma, 800 Ma, 450 Ma, 200 Ma, and 150 Ma (Fig. 6 in Dong and Santosh, 2016; Dong et al., 2011).

The Dabie-Sulu orogenic belt between the NCC and South China Craton is an UHP metamorphic terrane. The Dabie Block can also be considered as a continuation of the Triassic Qinling collisional orogen. Similarly to the QOB, the Dabie Block consists mainly of Triassic metamorphic rocks and Jurassic-Cretaceous (ca. 135–125 Ma; Li et al., 2010) igneous rocks (e.g. Hacker et al., 2006; Zhang et al., 1996). The Sulu Block is displaced to the northeast of Dabie Block by the Tan-Lu Fault (Fig. 2). The peak UHP metamorphism in Sulu has been dated to ca. 230–220 Ma (Hacker et al., 2006). Pre-Triassic zircon ages from Sulu area show peaks at ca. 2500 Ma, 2000–1800 Ma, and 750 Ma (Hacker et al., 2006).

5.4. Central Asian Orogenic Belt

The CAOB (also termed as the Altaids) is a potential north-northwestern primary source area to the CLP sediments and it is commonly referred to when the dust transport is designated to the EAWM. The CAOB spreads out from northern China to Mongolia and all the way to the Ural Mountains in Russia. It is bounded by the Siberian and Baltica cratons in the north and by the TC and NCC in the south. The CAOB is a combination of various Archean to Neoproterozoic micro-continental blocks or continental fragments, various arc systems and other tectonic elements that have amalgamated together in the closure of the Palaeo-Asian Ocean (PAO). The CAOB started to form already during the latest Mesoproterozoic (ca. 1 Ga) (Khain et al., 2002), although some suggest a later time at ca. 600 Ma (Wilhem et al., 2012). The eastward propagating final closure of the PAO occurred at the southern margin of CAOB during the late Palaeozoic-early Mesozoic time (e.g. Eizenhöfer et al., 2014; Eizenhöfer and Zhao, 2018; Wang et al., 2017a; Xiao et al., 2003; Zhou et al., 2018). The suture zones, along which the PAO closed, are the Tianshan Suture in the south-western CAOB, the Beishan-Alxa Suture in the southern CAOB and the Solonker Suture in the southeastern CAOB (Fig. 2).

In the following text, only the Mongolian and Chinese parts of the CAOB are considered, since it is unlikely that aeolian sediments from central Asia have been able to cross the various mountain belts that act as barriers in the west. Consequently, even though Mongolia forms the heart of the CAOB, only the southern part of the country is a focus here. Traditionally, Mongolia has been subdivided into two geologic domains that are separated by an approximate topographic and structural boundary called the Main Mongolian Lineament (MML) (Badarch et al., 2002 and references therein) (Figs. 1 and 2). The northern domain is generally older with mainly Neoproterozoic blocks that were affected by an early Palaeozoic orogeny, while the southern domain contains early Palaeozoic blocks reworked by late Palaeozoic to early Mesozoic tectonothermal events (Badarch et al., 2002 and references therein; Kröner et al., 2010). The MML follows the Mongolian Altai and Gobi-Altai Mts. in the west and continues roughly north of the Zuunbayan Basin in eastern Mongolia (Fig. A1; Badarch et al., 2002). It is likely that the MML also acts as a barrier for dust transport from northern Mongolia to the CLP. The Mongolian Gobi Desert is located mostly in the southern domain (Fig. 1).

Because of its complexity, there have been variable practices in the literature regarding the subdivision of the CAOB. This text will focus on eight different regions of the CAOB: Chinese Altai, Junggar, Yili, Chinese Tianshan, Beishan, Northern Alxa, Southern Mongolia, and NE China. In Figs. 2 and 3, the Southern Mongolia domain and adjacent areas are further divided into smaller terranes according to Badarch et al. (2002) and Parfenov et al. (2004), but these terranes are not discussed in detail.

5.4.1. CAOB in western China

The Chinese Altai, Junggar, Yili, and the Chinese Tianshan (North, Central, and South Tianshan; Fig. 2) surround the Gurbantunggut Desert/Junggar Basin (Fig. 1) that acts as a potential distal northwestern secondary source to the aeolian CLP sediments. The Junggar Block, which includes the Junggar and Turpan Basins (Fig. A1), and the North Tianshan, south of the Altai Mts., is mostly covered by Palaeozoic-Cenozoic sedimentary rocks. Although the basement rocks of the Junggar Block are largely unknown, the >450 Ma aged detrital zircons

from the block suggest dominant early Palaeozoic (ca. 510 Ma), and minor Palaeoproterozoic (ca. 1850 Ma) basement rock components (Zhou et al., 2018). The Junggar Basin is also surrounded by abundant Carboniferous and Permian rocks in the Chinese Altai, East Junggar Arc (south of Altai), North Tianshan and West Junggar Arc (northwest of Junggar Basin) (Han and Zhao, 2018; Wilhem et al., 2012).

Precambrian terranes are found from Central Tianshan, the Yili Block, and the Chinese Altai. The oldest rocks of this region are in Central Tianshan, where the major magmatic episodes took place at ca. 2.5 Ga, 1.8 Ga, and 1.45–0.8 Ga (Han and Zhao, 2018 and references therein). West of the Junggar Block, the Yili Block contains Meso- to Neoproterozoic basement rocks and abundant Palaeozoic rocks (Han and Zhao, 2018). North of the Junggar Block, the Chinese Altai formed during the long-lived Altai Orogen, which started in the Neoproterozoic and lasted until late Cenozoic, although its main period of evolution had ended by late Palaeozoic (Windley et al., 2002). The northernmost tip of the Chinese Altai consists mostly of late Neoproterozoic to Middle Ordovician metasediments and volcanic rocks, but magmatic events have lasted until Early Devonian (Windley et al., 2002). Compared to the northern part, the central part of the Chinese Altai is mostly Neoproterozoic to Silurian terrane that includes abundant high-grade metamorphic rocks and granites as well as metasediments (Windley et al., 2002). Younger rocks, such as late Devonian to Early Carboniferous granites are also present. Devonian to Early Carboniferous magmatic rocks are found mostly in the southern margin of the Chinese Altai (Windley et al., 2002). Two metamorphic events have been recorded from the Chinese Altai. First, at 390–365 Ma (Jiang et al., 2010; Liu et al., 2020a and references therein) and later at 293–260 Ma (Liu et al., 2020a and references therein).

The Chinese Tianshan can be divided into three units: North, Central, and South Tianshan (Fig. 2). The North Tianshan is located between the Junggar Basin and the Yili Block/Basin in the west and continues to the south of the Junggar and Turpan Basins in the east (Fig. 2). South Tianshan is located on the northern margin of the TC, and Central Tianshan forms strips between the Yili Block-North Tianshan and South Tianshan (Fig. 2). According to Han and Zhao (2018), no Precambrian rocks are found from the North Tianshan, but Palaeozoic magmatism was pervasive between ca. 450–260 Ma. Similarly, the Precambrian basement in Central Tianshan is overlain by Palaeozoic strata including granitoids with a continuous age range from ca. 500 Ma to ca. 250 Ma (Han and Zhao, 2018 and references therein). These ages have a wider range than in the entire Junggar-Tianshan region, where the Phanerozoic granitoids are mostly between ca. 300–270 Ma in age (Han and Zhao, 2018). The South Tianshan is a HP/UHP metamorphic belt that represents the closure of the PAO in the late Palaeozoic (Han and Zhao, 2018 and references therein; Xiao et al., 2013). Ophiolites are also abundant in the South Tianshan, with ages ranging mostly from 420 to 320 Ma (Han and Zhao, 2018 and references therein).

5.4.2. CAOB in northern China and southern Mongolia

The central parts of northern China and southern Mongolia are widely covered by deserts or arid/semi-arid areas (Fig. 1) that are capable of producing or storing silt for subsequent aeolian transport. The underlying bedrock is divided here into three units: the Beishan, the Northern Alxa, and the Southern Mongolia domain.

In the Chinese parts, the Beishan orogenic belt is located north of the Dunhuang Block (TC), northwest of the Yinshan Block (NCC), and east of the Tianshan, connecting Tianshan through the Northern Alxa region to the Solonker suture in the east (Fig. 2). Beishan is mostly composed of Neoproterozoic, Ordovician-Silurian, and late Permian-Triassic rocks (Xiao et al., 2010). High-grade metamorphic rocks in Beishan show the highest zircon U-Pb age peaks at 494 Ma, 464 Ma, and 375 Ma, and minor peaks at 742 Ma, 701 Ma, and ca. 300 Ma (Song et al., 2013a). Older Neoproterozoic rocks, with an age peak at 1040–910 Ma, have also been reported (Liu et al., 2015a).

The Northern Alxa region to the east of the Beishan orogenic belt includes ophiolitic and tectonic belts related to the closure of the PAO (e.g. Liu et al., 2017; Xiao et al., 2015; Zhao et al., 2020). The basement rocks are dominated by late Palaeozoic to Mesozoic magmatic rocks, with minor occurrences of early Palaeozoic magmatic rocks (e.g. Liu et al., 2017; Zhao et al., 2020). This region is mostly covered by the Badain Jaran Desert.

In the Mongolian part of the CAOB, one of the two presumably Precambrian terranes of the Southern Mongolia domain is situated in the southernmost tip of Mongolia, partly overlying the Northern Alxa Block (Fig. 2). Based on zircon U-Pb ages of 952 Ma and 916 Ma (Wang et al., 2001; Yarmolyuk et al., 2005) some authors suggest the existence of a Neoproterozoic South Mongolia microcontinent. However, based on microstructural analyses and zircon U-Pb ages, Taylor et al. (2013) interpret the Precambrian zircon ages as sediment protolith ages, and suggest that the southern part of Mongolia formed in a Devonian-Carboniferous arc system followed by a Permian-Triassic collision with northern China.

Most of the southern Mongolia domain is Phanerozoic (Badarch et al., 2002). A broad but poorly defined trend of eastward decreasing age of the rocks can be observed. According to Badarch et al. (2002) and Kröner et al. (2010), the southwestern parts of Mongolia consist mainly of Devonian to Permian rock units and minor Ordovician-Silurian rocks. A minor Ordovician-Devonian ophiolite terrane is located in the northwestern part of the southern Mongolia domain (Badarch et al., 2002). In the northern part of the domain (central Mongolia; Fig. 2), magmatic activity during the early Neoproterozoic (ca. 983–954 Ga) and events at ca. 500 Ma have been recorded (Demoux et al., 2009). The metamorphic and igneous rocks of the central parts of the southern Mongolia domain consist mostly of Ordovician-Silurian metamorphic rocks, Devonian-Permian plutonic and volcanic rocks, and Jurassic and Cretaceous volcanic rocks (Badarch et al., 2002). In Eastern Mongolia, Devonian-Permian plutonic and volcanic rocks are also common, as well as Triassic-Jurassic plutonic rocks. A terrane of Cenozoic plateau basalt is also present in eastern Mongolia (Badarch et al., 2002).

5.4.3. Eastern CAOB

The eastern segment of the CAOB, which is comprised of NE China and adjacent areas, is located north and northeast of the CLP, and has the potential to act as a source for the CLP dust via northerly/northeasterly winds. The eastern CAOB is known as the Xing'an-Mongolia Orogenic Belt. Numerous tectonic divisions of the area have been proposed, but most studies identify at least four blocks or terranes from northwest to southeast: the Erguna, Xing'an, Songliao-Xilinhot and Jiamusi-Khanka Blocks (Fig. 2) (e.g. Eizenhöfer and Zhao, 2018; Wu et al., 2011; Zhou et al., 2018).

The >450 Ma aged basement rocks in the Xing'an-Mongolia Orogenic Belt are mostly early Palaeozoic (540–460 Ma) (Zhou and Wilde, 2013 and references therein; Zhou et al., 2018 and references therein). Minor Neo- and Mesoproterozoic (1020–650 Ma), Palaeoproterozoic (1980–1700), and Neoarchean (2760–2490 Ma) rocks are also present (Zhou and Wilde, 2013 and references therein; Zhou et al., 2018 and references therein). Most of the Xing'an-Mongolia Orogenic Belt formed during Palaeozoic subduction and accretion events that led to the closure of the PAO (e.g. Zhou and Wilde, 2013; Zhou et al., 2018). One of the first closure events of PAO in the SE CAOB has been identified from the so-called Southern Orogen (which roughly corresponds to the 'Bainaimiao Arc' in some studies), which is located between the Solonker suture zone and the NCC (Fig. 2). The ages of detrital zircons from Permian sedimentary rocks and of igneous zircons from the Southern Orogen are mostly early Palaeozoic (ca. 450 Ma) (Eizenhöfer et al., 2014; Eizenhöfer and Zhao, 2018 and references therein). The so-called Northern Orogen (which roughly corresponds to the 'Baolidao Arc' in some studies), which is located north of the Solonker suture zone, also includes early Palaeozoic rocks mainly in its southern margin, although late Palaeozoic rocks are more abundant (Eizenhöfer and Zhao, 2018 and references therein). Early Palaeozoic rocks are found also from other

parts of the Xing'an-Mongolia Orogenic Belt. Zhou and Wilde (2013) and Zhou et al. (2011), for example, identify a late Pan-African (ca. 500 Ma) high-grade metamorphic belt from the eastern NE China, which they named the 'NE China Khondalite Belt' (Fig. 2).

According to Wu et al. (2011), granitoids are widespread in NE China and most of them crystallized during the late Palaeozoic, with zircon U-Pb age peaks at ca. 320 Ma, 250 Ma, 190 Ma, and 130 Ma. The final closure events of the PAO, and the termination of the CAOB, are considered to have taken place along the Solonker suture zone (Eizenhöfer et al., 2014; Wu et al., 2011; Xiao et al., 2003, 2015). The timing of the last closure events has been constrained to the period between 239 and 222 Ma (Wang et al., 2017a). After that, the eastern parts of NE China were affected by the subduction of the Palaeo-Pacific plate which formed most of the Jurassic granitoids in NE China (Wu et al., 2011).

5.5. Late Mesozoic rocks

Although most of the tectonic events that created the continental crust of the research area had already occurred by the early Mesozoic, some major tectonic events also took place in late Mesozoic time, like those already mentioned in the e.g. Qinling and Dabie orogenic belts. Most Jurassic-Cretaceous igneous rocks in northern China are concentrated in the eastern and southern parts (Dong et al., 2015; Stern et al., 2018). The late Mesozoic (ca. 170–120 Ma) tectonothermal events in East Asia are commonly called the 'Yanshan Revolution' or the 'Yanshan Movement' in Chinese literature (e.g. Dong et al., 2015). In the early stage (ca. 170–135 Ma) of the Yanshan Revolution, the events include, for example, collisional orogenies, accretions, intracontinental deformation and regional metamorphic events, but in the later stage (ca. 135–120 Ma), crustal extension resulted in large-scale magmatism, rift basins, metamorphic core complexes, and domal structures (Dong et al., 2015 and references therein). There are major Jurassic-Cretaceous orogenic belts located in the northeastern China and in Mongolia that formed in the first stage of Yanshan Revolution. Many Jurassic and/or Cretaceous orogens or accretionary complexes and igneous rocks are located in the areas east-northeast of the CLP (Fig. 1 in Dong et al., 2015).

5.6. Tibetan-Himalayan Orogen and the uplift history of the Northern Tibetan Plateau

The still ongoing India-Asia collision has resulted in the largest mountain chain on Earth. The timing of the start of the collision is debated with estimates depending on the favoured collision model, and ranging from ca. 65 (Ding et al., 2005) to 34 Ma (Aitchison et al., 2007), or even to 14 Ma (Xiao et al., 2017), although most studies prefer 55–50 Ma (e.g. Dupont-Nivet et al., 2010; Li et al., 2015 and references therein; Yuan et al., 2013; Zhu et al., 2005). The subsequent formation of the Tibetan Plateau (TP) and the evolution of its uplift in space and in time are important factors to consider, not only for understanding the regional geology, but also when studying the provenance of the aeolian sediments on the CLP. Multiple studies have reported that the uplift of the TP affected climate, especially by increasing aridification of Asian interior and by affecting Asian monsoon evolution (e.g. An et al., 2001; Manabe and Broccoli, 1990; Ren et al., 2020; Ruddiman and Kutzbach, 1989).

The uplift history of the TP is complex and disputed, and different models for the TP evolution have been suggested. For example, while many have proposed a high plateau in central Tibet already in the Eocene and an outward growth of TP towards its margins in north and south (e.g. Li et al., 2015 and references therein; Wang et al., 2014c and references therein), others suggest the high-elevation TP (in the literal sense of the word "plateau") only occurred during the late Palaeogene or Neogene (Fang et al., 2020; Spicer et al., 2020; Su et al., 2019b; Wang et al., 2017b). The youngest thrust belts are, however, situated at the margins of the Tibetan-Himalayan orogen (Li et al., 2015; Wang et al., 2014c), although deformation in parts of the northern TP (which is the target of this review) may have already started at the time of the India-Asia collision at ca. 50 Ma (Yuan et al., 2013 and references therein). At the northern margin, the thrust belts include e.g. the Main Pamir (<20 Ma), Mazatage (southern Tarim Basin) (<3 Ma), West Kunlun (ca. 23–0 Ma), and Northern Qilian Shan (8.3–3–0 Ma) thrust belts (Li et al., 2015 and references therein; Wang et al., 2014c and references therein). Strong NW TP uplift is suggested to have occurred at 1) ca. 23–12 Ma, 2) ca. 12–8 Ma, and 3) from 5 Ma onwards (Jiang and Li, 2014; Wang et al., 2003), while Eocene-Pliocene uplift events or rapid exhumation in the eastern and NE TP have been suggested to have occurred at least at ca. 1) 35–19 Ma, 2) 15–10 Ma, 3) 8 Ma, and 4) 3.6 Ma (Fang et al., 2007; Li et al., 2014 Li et al., 2015 and references therein; Nie et al., 2019; Wang et al., 2012; Wang et al., 2017b; Yuan et al., 2013 and references therein; Zhang et al., 2014c; Zheng et al., 2010). The first stages of NW and eastern TP uplift (Jiang and Li, 2014; Wang et al., 2003, 2012) at ca. 25–20 Ma roughly coincide with the onset of the aeolian sedimentation on the western CLP (Guo et al., 2002b; Qiang et al., 2011), and the late Neogene tectonic events correspond to the earlier listed (Section 2) times of events in dust cycle changes at ca. 8–7 Ma and ca. 3.6–3.3 Ma. However, the exact timing and nature of these uplift phases, as well as their extent, remains debated. Indeed, it is widely disputed as to whether the uplift of the TP was the main driver of the East Asian environmental changes during Pliocene or whether global cooling was more significant in changing the East Asian climate and dust cycles during this time period (e.g. An et al., 2001; Ge et al., 2013b; Li et al., 2014; Liu et al., 2015b; Lu et al., 2010, 2019; Nie et al., 2014a; Ren et al., 2020; Sun et al., 2020; Zhang et al., 2019). Indeed, many authors have noted a more convincing link between the timing of global cooling and aridification events in Asia and changes in RC and loess deposition (Ding et al., 2000; Lu et al., 2010). At present then, the role of Tibetan uplift in driving changes in climate or loess accumulation in East Asia remains unclear.

5.7. Summary

Section 5 discusses five major orogenic segments of the research area: the NCC, the TC and Altyn Tagh, the CCO, and the CAOB. The CLP lies mostly on the Ordos Block and TNCO in the Archean-Proterozoic NCC (Fig. 2). The TC and Altyn Tagh also experienced major rock forming events from the Neoarchean through Proterozoic, but these rocks are not widely exposed on the surface in the region. The Altyn Tagh subsequently experienced UHP metamorphism during the early Palaeozoic. The southern margin of TC also experienced early Palaeozoic collision forming parts of the CCO, while the northern margin of TC, on the other hand, collided with the southwestern part of CAOB in the late Palaeozoic. The youngest igneous event of the TC was when the Tarim LIP formed during the late Palaeozoic. While some of the geological history of the CCO is complex and extends back to Archean, most of the CCO formed during Neoproterozoic and early Palaeozoic. The collisional history is, however, relatively widely spread through all Palaeozoic, and in most terranes extends to early Mesozoic, and in the eastern parts, also to middle-late Mesozoic. The parts of the CAOB discussed in this paper have some Precambrian remnants that are mostly Neoproterozoic. However, the amalgamation of the numerous different blocks of CAOB in this region mostly occurred during the Palaeozoic and early Mesozoic. Especially the Southern Mongolia domain and the southern margin of the CAOB are dominated by late Palaeozoic rocks, marking the final closure events of the Palaeo-Asian Ocean. Subsequently, areas in NE China also experienced the late Mesozoic Yanshan Revolution.

6. Metamorphism in the primary source regions

6.1. North China Craton

In the NCC, the Archean basement rocks in both the Western and Eastern Blocks have been metamorphosed in greenschist through granulite facies (Zhao et al., 2005 and references therein). The low-grade metamorphic rocks include granites and greenstones, and the high-grade rocks include tonalite-trondhjemite-granodiorite (TTG) gneiss domes and granulites. The most striking feature in the NCC in terms of metamorphic temperatures is the abundant UHT rocks (e.g Guo et al., 2012; Jiao et al., 2011; Liu et al., 2012b; Santosh et al., 2007a) in the Khondalite Belt (KB; part of the IMSZ) in the Western Block (Fig. 3). The name of the KB refers to the graphite-bearing sillimanite garnet gneisses (khondalites) that are abundant in the area. The khondalites are accompanied with quartzo-feldspathic gneisses, garnet quartzites, marbles, and calc-silicate rocks with minor amphibolite and mafic granulites (e.g. Guo et al., 2012). While the KB formed under high-pressure granulite facies metamorphism as a result of the collision of the Yinshan and Ordos Blocks at ca. 1.95 Ga, the UHT metamorphism has been dated to have occurred later, at 1.93–1.92 Ga (Santosh et al., 2007a, 2007b). According to Jiao et al. (2011), the peak metamorphic temperatures of metasedimentary granulites in the area ranged between ~850 to ~1000 °C, and even >1000 °C based on Zr-in-rutile thermometry. Lower calculated temperatures (~650–850 °C) were assigned for post-peak processes (e.g. diffusion, dissolution/reprecipitation) by Jiao et al. (2011). The exposed parts of the eastern KB lie just north of the YR and Mu Us Desert (and probably also in the basement of the desert), and partly even underlay the northern parts of the CLP. This proximity may make it a significant contributor of detrital material to the desert and to the CLP.

The Helan-Qianli Mts. that are located to the west of the CLP (Figs. 11 and A1) belong to the khondalite series in the IMSZ/KB, but show also minor garnet-sillimanite S-type granites in addition to the khondalite series rocks (Zhao et al., 1999). Calculated metamorphic temperatures indicate three different metamorphic stages in a clockwise metamorphic *P-T* path: 600–650 °C, 750–800 °C, and 700–750 °C (Zhao et al., 1999). Unlike in the nearby KB, no HT/UHT rocks have been reported from the area.

The TNCO, which forms the basement of much of the eastern CLP, formed at ca. 1.85 Ga during the amalgamation of the Eastern and Western Blocks of the NCC (Zhao et al., 2005 and references therein). The TNCO has high-grade metamorphic complexes in Taihua, Fuping, Hengshan, Huai'an and Xuanhua, and low to intermediate grade metamorphic complexes in Dengfeng, Zhongtiao, Zanhuang, Lüliang, and Wutai (see locations in Fig. 11) (Zhao et al., 2000). The high-grade metamorphic complexes in the TNCO are mainly TTG gneisses and medium to high-pressure granulites. The Huai'an complex contains HP granulites with peak metamorphic temperatures between 750 and 870 °C, based on multimineral geothermobarometers (Guo et al., 2002a). Additionally, TNCO-aged rutile xenocrysts in Cenozoic carbonatite dykes near the Huai'an complex, ~50 km west of Nihewan (Section 10), record peak temperatures of 743–932 °C based on Zr-in-rutile geothermometry (corresponding to 859–4426 ppm Zr) (Wang et al., 2020).

6.2. High- and ultrahigh-temperature rocks outside the Khondalite Belt and Trans-North China Orogen

While granulites are common, and found in most orogenic belts, HT

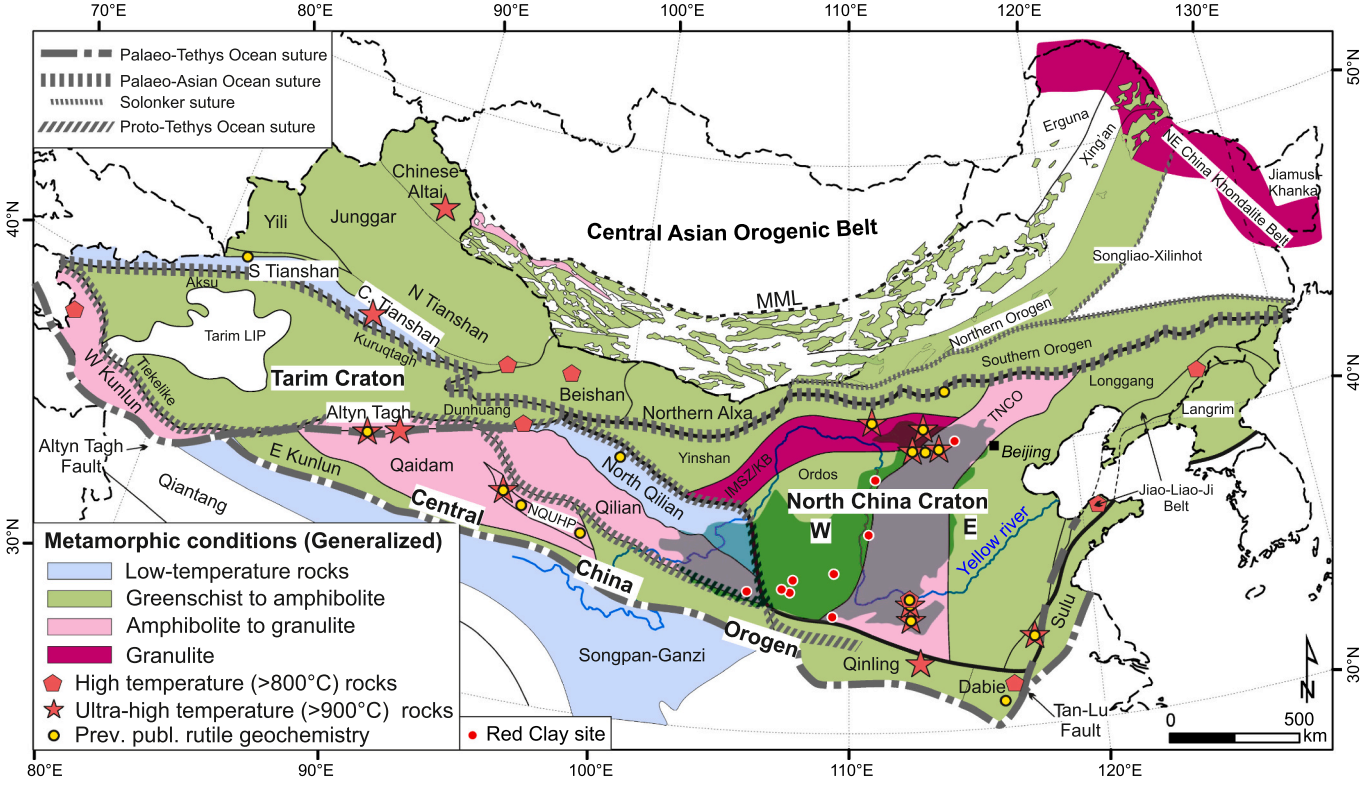

Fig. 3. Metamorphic temperature map of northern China, southern Mongolia, and parts of the Korean Peninsula. Most UHT localities in the study region are in the Inner Mongolia Suture Zone/Khondalite Belt (IMSZ/KB) and the Trans-North China Orogen (TNCO) north of or on the CLP (shaded area). The Tarim Craton, South Tianshan and North Qilian Orogen (NQO) to the west/northwest of the CLP are mostly low-grade or low-temperature regions. Also to the west of CLP, the Central China Orogen surrounding the Qaidam Basin is, however, dominated by higher metamorphic temperatures. Most of the terranes in the Central Asian Orogenic Belt have been metamorphosed in greenschist to amphibolite facies, Information on the Red Clay sites in Fig. 1. Terrane boundaries and other structural units are same as in Fig. 2. (For interpretation of the references to colour in this figure legend, the reader is referred to the web version of this article.)

and UHT granulites outside the KB and TNCO in the research area are relatively sporadic (Fig. 3). In the far west in the West Kunlun, HT-HP granulites experienced peak metamorphic temperatures of 760–820 °C based on conventional garnet and clinopyroxene Fe-Mg exchange geothermometry (Qu et al., 2007). Higher temperatures are reported from the distal northwestern primary source area in southern Chinese Altai, where some middle Devonian (ca. 390 Ma) and Permian (ca. 280 Ma) metapelitic HT-UHT granulites and gneisses have experienced peak temperatures up to ~980 °C based on different geothermobarometers (Liu et al., 2020a). Further south, localities with HT/UHT metamorphism from Southern and Central Tianshan have also been reported. Ophiolites in the Southern Tianshan have peak temperatures of 840–950 °C based on different geothermobarometers (Zhang and Jin, 2016), and granulites in the same area have recorded similar peak conditions (795–964 °C) (Wang et al., 1999). Low pressure (LP)-HT granulites in eastern part of Central Tianshan have peak metamorphic temperatures of 750–840 °C based on different geothermobarometers (Mao et al., 2015).

To the southeast of Tianshan, in the Dunhuang Block of TC, Palaeoproterozoic HP mafic granulites experienced peak temperatures between 760 and 858 °C depending on which geothermobarometer is used (Zhang et al., 2012b). Together with Altyn Tagh, Qaidam, and Qilian Block, this region surrounding the northern and eastern parts of Qaidam Basin has generally been metamorphosed in relatively high temperatures (Fig. 3). In the SE margin of TC, HT/UHT granulites have been reported from a HP-UHP metamorphic belt in the southern Altyn Tagh, where they record Early Palaeozoic subduction-collision events (e.g. Dong et al., 2018a; Liu et al., 2012a; Zhang et al., 2014a). There, the Zr-in-rutile peak metamorphic temperatures reached ~950 °C (~3000 ppm Zr) at ca. 485 Ma and post-peak temperatures ~780 °C (~1000 ppm Zr) at ca. 450 Ma (Zhang et al., 2014a). Nearby, early Cambrian UHT rocks from the western Qaidam Block recorded Ti-in-zircon (Ferry and Watson, 2007) peak temperatures between 914 and 1009 °C for felsic and pelitic gneisses and ~ 910 °C for mafic granulite (Teng et al., 2020). In the NQUHP, some very high-pressure garnet peridotites (with rutile exsolutions in garnet) have also experienced UHT conditions with a temperature range 960–1040 °C (Song et al., 2004).

In the eastern parts of CCO in the QOB, south of the CLP, Early Palaeozoic HT/UHT metamorphism occurred, and based on conventional geothermobarometry, peak temperatures of 880–920 °C have been reported (Bader et al., 2013 and references therein). In a HT metamorphic terrane in the Dabie Block, the metamorphism reached temperatures up to 800–830 °C (Zhang et al., 1996). However, UHT peak metamorphism at 927 °C based on Ti-in-zircon geothermometry has also been reported from the same terrane, although the rutile inclusions in these zircons record temperatures of only 783–798 °C (Lei et al., 2020). Nearby, southeast of the CLP in eastern NCC, in the southwestern part of the Jiao-Liao-Ji Belt, Palaeoproterozoic HP-UHT mafic granulites with Zr-in-rutile metamorphic peak temperatures of ~935 °C (up to ~950 °C) and post-peak temperatures of ~800 °C were recently reported (Cai et al., 2020). Further northeast in the Jiao-Liao-Ji Belt, HT granulites have been reported from pelitic granulites (up to 900 °C) in the middle regions of the belt (Tam et al., 2012), and from mafic and pelitic granulites in northeastern parts (up to 890 °C) (Cai et al., 2017).

6.3. Tarim Craton and Altyn Tagh

In addition to the HT rocks in Dunhuang, the Tiekelike and Kuruqtagh Blocks in TC also contain Palaeoproterozoic high-grade metamorphic rocks that are probably related to the assembly of the Columbia/Nuna supercontinent (Wang et al., 2014a; Zhang et al., 2012a). Compared to the HT granulites in Dunhuang, the Proterozoic metapelitic mica schists in Kuruqtagh experienced lower temperatures of 690 °C (Ge et al., 2013a). Also the Neoproterozoic metamorphic rocks in Kuruqtagh experienced upper amphibolite facies metamorphism at peak temperatures of 660–700 °C (Ge et al., 2016). The Precambrian North Altyn Tagh consists also of amphibolite to granulite facies metamorphic rocks. Between the North Altyn Tagh and the previously discussed southern Altyn Tagh HP-UHP metamorphic belt, the metamorphic conditions in the Altyn Tagh in terms of temperature have been low (Dong et al., 2018a and references therein). Similarly, in the northwestern TC, the Neoproterozoic Aksu blueschists formed in low temperatures, at about 300–400 °C (Zhang et al., 1999). As discussed earlier, the Meso- to Neoproterozoic low-grade metasedimentary and volcanic strata are one of the prevailing rock types in TC.

6.4. Central China Orogen

In the western parts of the CCO, the West Kunlun is dominated by igneous and supracrustal rocks, but the metamorphic complexes include gneisses and migmatites in the north, and low- to medium-grade schists and gneisses in the south (Gaetani et al., 1990; Yuan et al., 2002). Further east, the EKO has various types of metamorphic, sedimentary, and igneous rocks and has a rather complex tectonic history. The western part of the EKO consists mainly of Early Palaeozoic low-grade metamorphic rocks and marine sediments (e.g. Liu et al., 2005). The eastern part of the EKO is dominated by amphibolite-facies metamorphism, except at some localities with greenschist-facies dominance and some localities with granulite-facies relics in amphibolite-facies rocks (Liu et al., 2005). For the amphibolite-facies rocks, metamorphic temperatures between 535 and 770 °C have been reported, and for the granulite relics, temperatures of 826–896 °C (Liu et al., 2005). The EKO also includes a 500 km long HP/UHP metamorphic belt that experienced peak metamorphic temperatures of 590–675 °C (Meng et al., 2013; Song et al., 2018), marking the subduction-collision during the closure of the Proto-Tethys Ocean (Song et al., 2018).

Apart from EKO, other areas surrounding the Qaidam Basin are relatively high-grade metamorphic regions. The NQUHP consists mainly of ortho- and paragneisses, amphibolites, mafic granulites, marbles, and locally granite intrusions, eclogites, and garnet peridotites (Zhang et al., 2008; Zhou et al., 2019). In addition to the previously mentioned UHT rocks in the NQUHP, some eclogites have been granulitized with metamorphic temperatures reaching up to 883 °C, followed by a retrograde amphibolite facies stage at temperatures <650 °C (Zhou et al., 2019). The Qilian Block between the NQO and the NQUHP consists of Precambrian basement with felsic gneiss, marble, amphibolite, and minor granulite, and is overlain by Palaeozoic sedimentary sequences. Contrary to the Qilian Block, the metamorphic rocks in the NQO are mostly blueschists, eclogites, and greenschists. The NQO is a HP-low-temperature zone, where the Early Palaeozoic peak metamorphic temperatures of the HP rocks have been as low as 420–540 °C (Song et al., 2007; Zhang et al., 2007).

In the eastern CCO, despite the previously discussed UHT rocks in the QOB, most of the QOB has, however, been metamorphosed in amphibolite facies. The northern part of the QOB has recorded peak metamorphic temperatures of ~700 °C (You et al., 1993). Further east, the Dabie Block can be subdivided into different units based on the grade of metamorphism (Zhang et al., 1996). The northern part of the block consists of low-grade metasedimentary rocks. Other parts consist mainly of HP/UHP rocks, such as eclogites and blueschists, with coesite and diamond localities. A minor HT belt is also identified, with upper amphibolite to granulite facies rocks that show peak metamorphic temperatures at ~680–750 °C for the amphibolite facies rocks and ~ 750–830 °C for the granulite facies rocks (Zhang et al., 1996). The Sulu Block, which is located to the east of the CLP, has a similar metamorphic rock assemblage as the Dabie Block and is not further discussed here.

6.5. Central Asian Orogenic Belt

Despite the above-mentioned sporadic occurrence of HT/UHT rocks in the Chinese Altai and South and Central Tianshan, the CAOB in

western China is mostly a relatively low-temperature region in terms of metamorphism. For example, the Chinese Altai consists mostly of greenschist to amphibolite facies rocks (<780 °C; Liu et al., 2020a and references therein; Jiang et al., 2010, 2015; Wei et al., 2007; Windley et al., 2002), and the higher temperature granulites are mostly found from the southern Chinese Altai, as discussed earlier. Also in the west, the Yili Block contains both low- and high-grade rocks (Wang et al., 2014b and references therein). Further south, low metamorphic temperatures become more dominant. The exposed metamorphic rocks in North Tianshan are mostly HP metamorphic rocks that formed in an accretionary wedge (Han and Zhao, 2018) and the relatively abundant Precambrian rocks in Central Tianshan comprise high-grade metamorphic suites, but the younger rocks are mainly lower grade greenschists (Han and Zhao, 2018). South Tianshan is generally a HP-low-temperature metamorphic belt that consists mainly of HP blueschist-, and eclogite-facies rocks and low-pressure and -temperature greenschist facies rocks. The belt includes abundant HP-UHP metamorphic rocks, but the peak metamorphic temperatures of even the HP rocks have mostly been relatively low, up to 580 °C (Gao et al., 1999).

Along the southern margin of the CAOB, further east, the Beishan orogenic belt includes high-grade metamorphic rocks and low-grade metasedimentary rocks (Song et al., 2013a). By using a garnet-biotite thermometer, Zong et al. (2017) calculated metamorphic temperatures of ~600 °C, and by Ti-in-zircon thermometer, temperatures up to 840 °C. In the neighbouring block, the metamorphism of the northern Alxa-southern Mongolia region mostly impacted the older basement rocks that have been metamorphosed in greenschist to amphibolite facies (Zhao et al., 2020). According to Zhao et al. (2020), most granitoids in the northern Alxa region are, however, free from metamorphism. In the southernmost tip of Mongolia, the Neoproterozoic to Palaeozoic terrane includes high-grade amphibolite facies metamorphic rocks that are presumably older than lower-grade metamorphic rocks in the area (Wang et al., 2001), but no detailed studies on the metamorphic conditions have been published.

The metamorphic rocks in the southern Mongolian parts of the CAOB are typically metasediments that were metamorphosed in greenschist facies (Badarch et al., 2002). Higher grade rocks are mainly found from areas in SE Mongolia, where gneisses, amphibolites, and other variably metamorphosed rocks have been identified (Badarch et al., 2002). The SE CAOB that recorded the last closure events of the PAO, formed in multiple subduction and accretion events, which have locally led to the formation of HP metamorphic rocks. The metamorphic assemblage of the Solonker suture between the Northern and Southern Orogens in Inner Mongolia consists mostly of greenschist- and amphibolite-facies rocks, with some HP blueschist localities (Zhang et al., 2016b). The highest temperatures, 760–790 °C (Zhang et al., 2018b), have been reported from a single area in the Northern Orogen, but many rocks in the Solonker suture zone also show formation temperatures lower than 500 °C (Zhang et al., 2016b). The most eastern segment of the CAOB in NE China includes high-grade metamorphic rocks that form the "NE China Khondalite Belt" (Zhou and Wilde, 2013; Zhou et al., 2011).

6.6. Summary

The most conspicuous region in the research area in terms of metamorphic temperatures is the UHT KB (in IMSZ/NCC), that lies just north of, and partly underlies, the CLP. UHT rocks are not widespread in any other area, although they occur sporadically in other regions (Fig. 3). Also, the TNCO in the NCC is mostly a high-grade metamorphic terrane with some UHT localities. The Archean to Proterozoic blocks of the NCC are generally metamorphosed in different conditions from greenschist to granulite facies.

In the west, the TC consists mostly of relatively low-grade metamorphic rocks, with temperatures <700 °C, whereas the adjacent Altyn Tagh region was affected by amphibolite to granulite facies metamorphism, locally reaching UHT temperatures up to ~950 °C. Further to the southeast, the CCO shows variability in metamorphic conditions between terranes. The West Kunlun, although not rich in metamorphic rocks, comprises both lower- and higher-grade rocks, with some HT localities. The EKO also consists of various grades of metamorphic rocks, but the greenschist to amphibolite facies rocks dominate, with temperatures mostly <770 °C. The Qaidam Block is a dominantly high-grade metamorphic terrane with amphibolites and granulites, and especially in the NQUHP, the peak temperatures reached HT and UHT conditions. The Qilian Block is similar to the Qaidam Block with mostly amphibolite facies rocks, but the NQO is a strikingly different HP-low-temperature terrane with temperatures <540 °C. In the southern/southeastern regions of the CLP, the QOB mostly consists of rocks with peak temperatures of ~700 °C. The Dabie-Sulu regions have abundant HP/UHP rocks, but metamorphic temperatures have been moderate, apart from some HT/UHT localities.

The parts of the CAOB discussed in this paper have generally experienced low- to medium-grade metamorphism from greenschist to amphibolite facies. An exception is in the NE China Khondalite belt, from where HT rocks with temperatures <850 °C have been reported. On the contrary, an especially low-temperature zone is located in the southwest in the South Tianshan, where HP rocks have temperatures <580 °C. Together with the relatively low-grade metamorphic conditions of the TC, these distal western primary dust source regions to the CLP sediments form a region of relatively low metamorphic temperatures, which continues to the more proximal western source terrane of the NQO.

7. Detrital zircon U-Pb data from potential source regions

In the past decade or so, detrital zircon U-Pb dating has become the most prominent single-grain provenance method, with a rapid increase in amounts of data for CLP and potential source sediments, especially for the late Quaternary loess (e.g. Bird et al., 2015; Fenn et al., 2018; Licht et al., 2016: Nie et al., 2015, 2018; Pullen et al., 2011; Rittner et al., 2016; Stevens et al., 2010, 2013; Zhang et al., 2016a, 2018a; Zhang et al., 2021a). This has allowed a more precise and accurate interpretation of the sources for the sediments. However, as the data are collected and filtered in many different ways, their comparison may be challenging. There are differences not only in the analytical methods, but also in the decisions related to which ages are used, discordance acceptance criteria, and how the data are plotted and the results compared.

In order to compile an internally consistent data set of the original published ages from the previous studies, these data are grouped and standardised as far as possible here. Firstly, a discordance filter of 10% has been applied to the age data, while a threshold of 1.0 Ga separates the U-Pb age used; $^{206}Pb/^{238}U$ ages <1.0 Ga and $^{207}Pb/^{206}Pb$ ages >1.0 Ga. The detrital age data are plotted as KDEs with a bandwidth of 15 Myr using the R package "provenance" (Vermeesch et al., 2016).

The detrital zircon age distributions of potential source regions in the range of 600–0 Ma are presented in Fig. 4. Most of these secondary (sedimentary) source areas show two major peaks in the zircon age probability diagrams: an early Palaeozoic (ca. 500–400 Ma) and a late Palaeozoic-early Mesozoic (ca. 300–200 Ma) peak, which reflect the geologic history of the primary source areas (Fig. 4). Smaller peaks can be seen at age ranges 1000–500 Ma, 2000–1500 Ma, and at ca. 2500 Ma (Fig. 5). The CLP lies mostly on the NCC (Fig. 2), and it is therefore likely that the majority of the Palaeoproterozoic and Archean detrital zircons in the CLP sediments derive from the NCC, where these old rocks are dominant and widely exposed.

Most western sources and sources in the CCO show a higher 500–400 Ma age component, while most of the CAOB, central deserts (Kumtag, Badain Jaran and Tengger deserts), and NCC sources show a higher 300–200 Ma age component. However, there are exceptions: Junggar in the CAOB, the Qinling Mts. in the CCO, and western Mu Us in the NCC. The underlying basement in the Junggar Basin is relatively unknown,

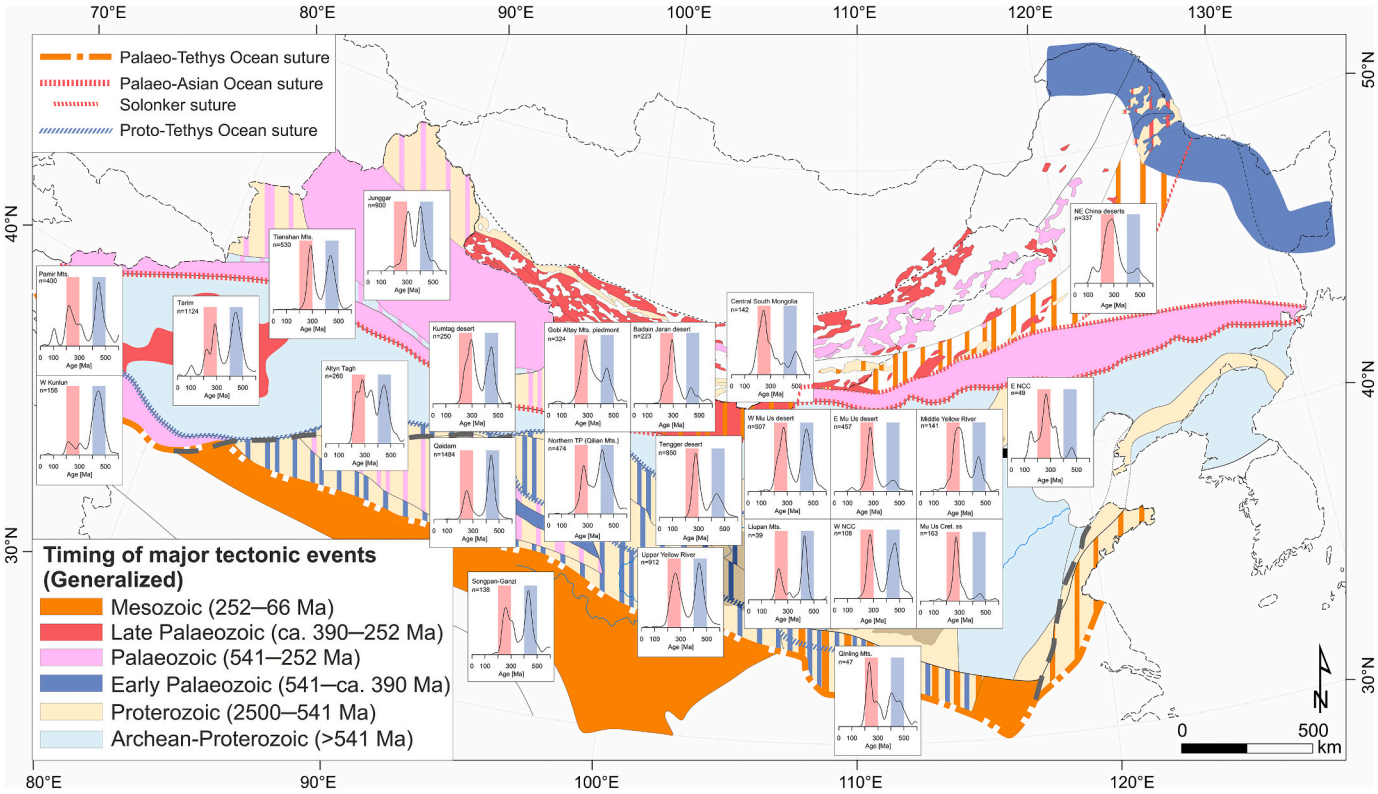

Fig. 4. KDEs of the secondary (sedimentary) source region detrital zircon U-Pb ages in the range of 600–0 Ma. The early Palaeozoic (500–400 Ma) age range is highlighted in blue colour, and the late Palaeozoic to early Mesozoic (300–200 Ma) age range in red colour. Data sources are listed in Appendix A. The background is explained in Fig. 2. The number of zircon ages refers to those between 600 and 0 Ma, although the KDEs are drawn from the whole data. Reflecting the geologic history of the primary source areas, most regions to the west of CLP have higher 500–400 Ma age peak than the 300–200 Ma peak, while the opposite pattern occurs in the regions to the north, northwest and northeast of CLP. (For interpretation of the references to colour in this figure legend, the reader is referred to the web version of this article.)

and the surrounding regions have also been active in the early Palaeozoic time (Section 5.4.1), which may explain the high amount of 500–400 Ma zircon ages in the basin. The detrital zircon ages from the Qinling Mts. are low in number and the relative heights of the peaks are unreliable. The Qinling Mts. age peaks roughly correspond to the orogenic events of the QOB at ca. 150 Ma, ca. 200 Ma, ca. 450 Ma, and ca. 1000–700 Ma, although the youngest ages are not clearly presented in the age distribution (Figs. 4 and 5). The proportion of the early Palaeozoic ages in the zircon age distribution here may also be underestimated because of the low number of zircons (Diwu et al., 2012). In terms of the western Mu Us, Stevens et al. (2013) showed that the YR brings sediments from the Northern TP to this part of the desert, which explains the distinct age-distribution curves between the eastern and western Mu Us. The eastern Mu Us sample reflects sources from the underlying Cretaceous sandstone and NCC, while the western Mu Us sample reflects sources from the Northern TP, despite its location on the NCC.

In addition to the Qinling Mts., the zircon age distribution of the SGC is more diverse than those of the other CCO sources, which likely reflects the multiple source areas of the Triassic sediments in the SGC (Section 5.3). As mentioned earlier, the SGC is included in this review, because it may have provided sediments to the CLP through YR transport, although it is not clear whether the YR existed in the Neogene. Additionally, there are no indicators of southwesterly palaeowinds that would be required to transport this material to the CLP in the absence of long-distance river transport, and the abundance of ca. 780 Ma and ca. 1850 Ma zircons in the complex (Fig. 5) should also be reflected in the RC zircon age distributions, which is not the case (Nie et al., 2018). The upper YR and western Mu Us, however, do show a small peak of Neoproterozoic ages (Fig. 5), which may derive from the SGC. The multiple steps of transport would explain the relatively low amount of Neoproterozoic ages in the RCs even if the Neoproterozoic zircons are initially sourced from the SGC.

Another notable feature of the Neoproterozoic ages in the CCO is from Qaidam Basin, where the age distribution is strongly dominated by the early Paleozoic age peak (Fig. 5), consistent with the CCO evolution. However, Neoproterozoic ages are relatively few, despite the fact that the Qaidam, EKO, Qilian, and Altyn Tagh terranes that underlie or surround the Qaidam Basin were all tectonically active during this Era. The reasons for his are unclear. One explanation could be that the Neoproterozoic tectonic events in the CCO were not as widespread as the later events (Section 5.3).

The age distribution from Tarim Basin (Taklamakan Desert) is surprising in its relatively low number of Precambrian zircons (Fig. 5). Other perhaps unexpected peaks are the ca. 210 Ma, ca. 100 Ma, and younger age peaks (Figs. 4 and 5), since no Mesozoic nor Cenozoic tectonothermal events have been reported from Tarim (Stern et al., 2018; Zhang et al., 2013). It is likely that these zircons are related to the Mesozoic and Cenozoic magmatic events of the Pamir (Chapman et al., 2018; Rittner et al., 2016), which is supported by the Pamir age distribution (Figs. 4 and 5). Some of the younger zircons may have also formed in metamorphic events linked to the Tibetan-Himalayan orogen. The early and late Palaeozoic peaks have similar heights, which reflects the early Palaeozoic collisional events to the south of the craton (Kunlun-Altyn Tagh-Qaidam), and the late Palaeozoic events to the north of the craton (Tianshan/CAOB). The late Palaeozoic peak may also include zircons formed in the Tarim LIP.

A similar, perhaps unexpected, scarcity of Precambrian zircons is also seen in the Altyn Tagh age distribution (Fig. 5), and the abundance of <400 Ma ages is also inconsistent with what we know about the

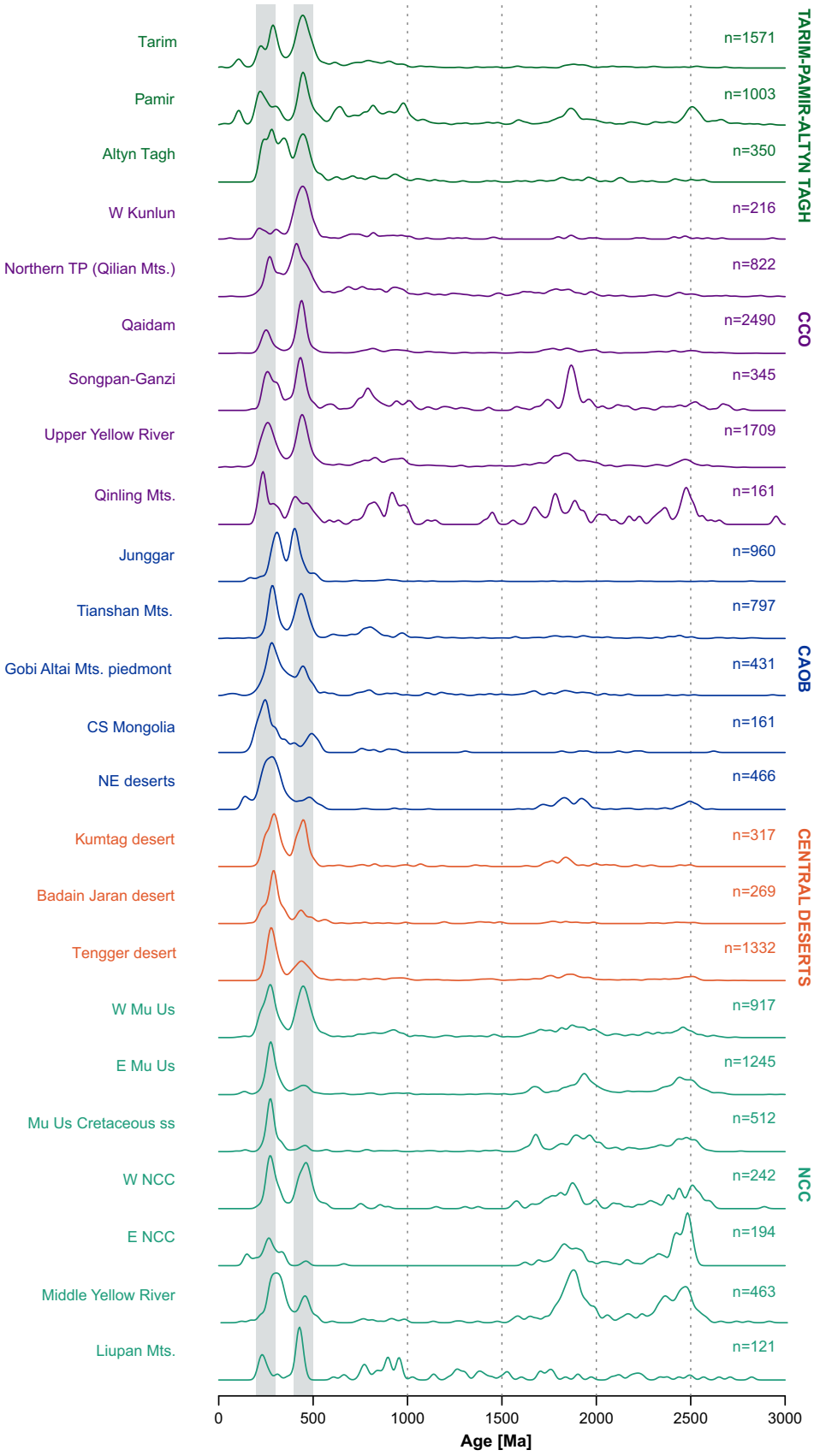

Fig. 5. KDEs of the secondary (sedimentary) source region detrital zircon U-Pb ages. The grey bars indicate the age ranges 300–200 and 500–400 Ma. The Tarim Basin and Altyn Tagh have unexpectedly low amounts of Precambrian zircons when compared to the primary rocks in these areas (Section 5.2), and the Altyn Tagh also has unexpectedly abundant <400 Ma ages. The ca. <210 Ma zircons of Tarim are likely sourced from the Pamir Mts. Most areas in the CCO are consistent with the primary rocks (Section 5.3), and the anomalous Qinling Mts. age peaks roughly correspond to the orogenic events of the QOB at ca. 150 Ma, ca. 200 Ma, ca. 450 Ma, and ca. 1000–700 Ma. The age distributions of the CAOB secondary sources are also mostly consistent with the CAOB primary source rocks (Section 5.4), although Junggar Basin data may also show features of the relatively poorly understood basement rocks. The central deserts show affinity to the CAOB sources, with the exception of the Kumtag, that may also receive more material from the CCO and/or Tarim. Most of the NCC samples have abundant Precambrian ages, consistent with the primary rocks (Section 5.1). The W Mu Us reflects material transported from the northern TP via the YR, while the E Mu Us reflects sources from the underlying Cretaceous sandstone (Stevens et al., 2013). The W NCC samples are from southern CLP river sediments and the abundant 500–400 Ma zircon ages may derive from the collisional events between the North QOB and the NCC (Diwu et al., 2012). The Liupan Mts. sample is from Cretaceous strata and possibly reflects the tectonic events of QOB, similarly to the sample from the Qinling Mts. The E NCC and NE deserts have abundant <200 Ma ages that are likely linked to the late Mesozoic Yanshan Revolution. Locations of the samples are indicated in Supplementary Fig. A1. Data sources are listed in Appendix A.

primary rocks in the Altyn Tagh region (Section 5.2). It is unclear where those zircons derive from. The zircon age distribution of the nearby Kumtag Desert, which is located on the TC (Dunhuang Block), between the CAOB and CCO, has relatively high peaks of both 300–200 and 500–400 Ma ages, which may reflect material from both north and south of the desert.

The Badain Jaran Desert lies mostly on the Yinshan (Alxa) Block/western NCC, southeast of the Beishan Mts., north of the Qilian Mts., and northwest of Tengger Desert (Fig. 1). The age distributions of the Badain Jaran and Tengger Deserts are quite similar and show affinity to CAOB sources despite their location on the western NCC. The western NCC samples that were sampled from modern river sediments of the Jing and Luo Rivers in the southern CLP (Diwu et al., 2012), show abundant early Palaeozoic zircons, which Diwu et al. (2012) designate to the collisional events between the North QOB and the NCC. The Liupan Mts. sample is from Cretaceous strata (Nie et al., 2014a) and possibly also reflects events related to the QOB (Fig. 5). Eastern NCC samples are consistent with the old craton that reactivated before and during the late Mesozoic Yanshan Revolution.

The sources in CAOB seem to be consistent with the tectonic evolution of the area. The Tianshan Mts., the Gobi Altay Mts. piedmont, Central South Mongolia, and NE China deserts all have higher 300–200 Ma age components, and the 500–400 Ma age component is, as expected, relatively low in the latter three, although the number of zircon ages in the Central South Mongolia sample is too low for reliable comparison of relative peak heights. The Mesozoic Yanshan Revolution is recorded in the NE deserts by the 200–100 Ma zircon ages but the 500–400 Ma age component is lower than would be expected since early Palaeozoic activity is recorded also from this region (Fig. 4, Section 5.4.3). There is also variation in the exact locations of the <500 Ma age peaks in the CAOB samples, which may reflect the complex history of the CAOB with many collisional events of numerous different microcontinents and other tectonic blocks (Section 5.4).

8. Previously published rutile data from the potential source regions

There are five studies that have analysed detrital rutiles in the research area of this paper: Liu et al. (2014a), Liu et al. (2014b), Zhao and Liu (2019), Liu et al. (2020b), and Zhao et al. (2021). Other studies have used Zr-in-rutile thermometry in non-detrital metamorphic rocks. All previously published Zr contents in rutiles of the area are listed in Table 2. Fig. 3 shows the locations of these studies.

A closer look at the study of by Liu et al. (2014a) from the northern NCC can be used as an example of a sedimentary provenance analysis with detrital rutiles, although they primarily used zircon data. The detrital rutiles from two different Precambrian formations in the studied Huade Group in northern NCC showed distinct features in terms of Cr-Nb systematics. The older formation showed only metapelitic rutiles, while the younger formation had a mixed population of metamafic and metapelitic rutiles. Also, the Zr-in-rutile temperatures were slightly higher for the younger formation, and two UHT rutiles suggested that the KB could be one source area for the sediments, according to Liu et al. (2014a).

Another study close to the CLP (Fig. 11 in Section 10) is by Shi et al. (2012), who used Zr-in-rutile thermometry in the Daixian rutile ore deposit located close to the KB in the TNCO (Figs. 3 and 11). Their study reports ca. 1.78 Ga amphibolite facies metamorphism and rutile crystallization temperatures mostly up to ~650 °C. All their rutiles indicate a metamafic protolith according to the Cr-Nb systematics. Additionally, detrital rutiles from Carboniferous bauxite ores in northern and southern TNCO yield distinct Zr-in-rutile metamorphic temperature signals (Zhao and Liu, 2019; Liu et al., 2020b; Zhao et al., 2021); the northern part having more abundant (66%) granulite facies rutiles than the southern part (13%) (Zhao et al., 2021). The northern TNCO detrital rutiles appear to be sourced from the adjacent Wutai and Fuping complexes, and from the northern margin of the NCC, while the rutiles in the southern TNCO bauxites were mostly derived from adjacent metamorphic complexes (e.g. Zhongtiao) and from North QOB (Zhao et al., 2021).

9. Neogene Red Clay provenance

9.1. Published Red Clay zircon U-Pb data

A number of single-grain (zircon U-Pb) provenance studies have hitherto been conducted on the RC deposits. Similarly to the source region sediments, most RC units show two significant zircon age populations: 300–200 Ma and 500–400 Ma, and occasionally smaller peaks in the age ranges of 1000–500 Ma, 2000–1500 Ma, and at ca. 2500 Ma

Table 2
Previously published metamorphic temperatures from the potential source regions calculated by using Zr-in-rutile geothermometry. Studies on detrital rutiles are in italics. Thermometers: 1: Zack et al. (2004a); 2a: Tomkins et al. (2007) in α-quartz field; 2b: Tomkins et al. (2007) in β-quartz field; 2c: Tomkins et al. (2007) in coesite field 3: Ferry and Watson (2007); 4: Watson et al. (2006).

Area	Rock type	Peak T [°C]	Thermometer	Zr [ppm]	Rock lithology (Cr-Nb)	Reference
CAOB: W Tianshan	eclogite	~638[a]	1	150–160[a]	mafic	Su et al. (2018)
CAOB: W Tianshan	vein in eclogite	540–580	2c	38–66	mafic	Lü et al. (2012)
CAOB: W Tianshan	eclogite and vein	530–570	2a, 2c	22–66	mafic	Chen et al. (2013)
CAOB: W Tianshan	eclogite	368–528	1	19–68	mafic	Tan et al. (2019)
CAOB: W Tianshan	eclogite	496–524	2c	11–17	mafic	Zhang et al. (2010)
S Altyn Tagh	HP granulite	780–950	2a–b	727–4099	mafic & pelitic	Zhang et al. (2014a)
CCO: N Qaidam	eclogite & vein in eclogite	609–682	2b–c	62–181	mafic	Chen et al. (2020)
CCO: N Qaidam	eclogite	615–765	2c	60–417	mafic	Zhang et al. (2010)
CCO: N Qilian	eclogite	555–608	2a	31–71	mafic	Zhang et al. (2010)
CCO: Dabie	rutile inclusions in UHT metamorphic zircons	783–798	2b	1251–1451	–	Lei et al. (2020)
CCO: Dabie	*UHP metasediments and river sands*	*566–752*	*2c*	*32–371*	*mafic & pelitic*	Liu et al. (2014b)
N NCC	*metasediments*	*~630–770*[b]	*4*	*291–17,995*	*mafic & pelitic*	Liu et al. (2014a)
N NCC: KB	UHT granulites	650–1000	3	500–8000	pelitic	Jiao et al. (2011)
N NCC: TNCO	rutile xenocrysts in carbonatite dykes	743–932	2a	859–4426	pelitic	Wang et al. (2020)
N NCC: TNCO	gneisses and quartzite in a rutile ore deposit	595–682	2b	170–526	mafic	Shi et al. (2012)
N NCC: TNCO	*bauxite ore*	*470–955*	*4*	*22–5244*	*mafic & pelitic*	Zhao et al. (2021)
S NCC: TNCO	*bauxite ore*	*408–903*	*4*	*6–3617*	*mafic & pelitic*	Zhao et al. (2021)
S NCC: TNCO	*bauxite ore*	*448–845*	*4*	*2–2310*	*mafic & pelitic*	Liu et al. (2020b)
S NCC: TNCO	*bauxite ore*	*527–942*	*4*	*53–4824*	*mafic & pelitic*	Zhao and Liu (2019)
E NCC: Jiao-Liao-Ji Belt	mafic granulites	778–948	2a	1021–4209	mafic	Cai et al. (2020)

[a] Only the highest reported temperature/Zr concentration is listed.
[b] Outliers in data are excluded.

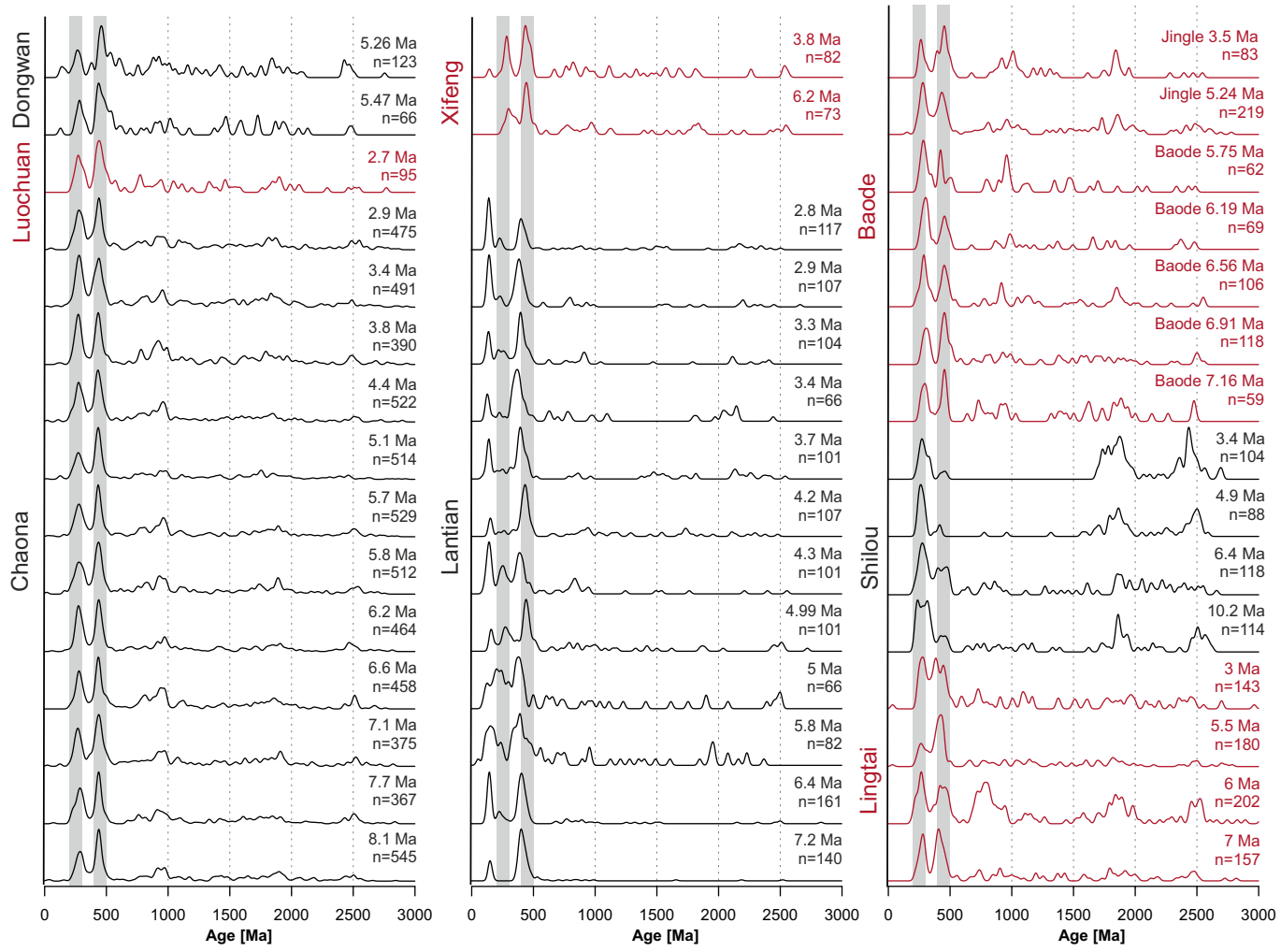

Fig. 6. KDEs of the published Red Clay zircon U-Pb ages. The grey bars indicate the age ranges 300–200 and 500–400 Ma. Data are from: Shang et al. (2016; Dongwan, Baode, Lantian), Gong et al. (2017; Lingtai), Nie et al. (2018; Chaona), Pan et al. (2018; Shilou), Zhang et al. (2018a; Lantian), and Liu et al. (2019; Xifeng, Luochuan). The data set from Chaona, central CLP, is the only data set with high-*N* zircon ages. There, the proportion of 300–200 Ma and 2750–1500 Ma ages compared to the 500–400 Ma ages is relatively lower in the 8.1 Ma and 5.8–4.4 Ma units than in the 7.7–6.2 Ma and 3.8–2.9 Ma units (Nie et al., 2018). (For interpretation of the references to colour in this figure legend, the reader is referred to the web version of this article.)

(Fig. 6). Below, each site is first examined through time, and following this the differences between sites are compared.

The RC accumulation in the northernmost RC site Baode began at least 7.23 Myr ago (Zhu et al., 2008). The zircon U-Pb data from 7.16–3.5 Ma units show that the 300–200 Ma age component is generally higher than the 500–400 Ma age component, but the low number of zircon ages reported by Shang et al. (2016) limits the ability to reliably interpret possible temporal variation in the Baode RC provenance. The 5.24 Ma Jingle Formation sample has the highest amount of zircon data, and the highest peak at 300–200 Ma (Fig. 6). The prevailing 300–200 Ma age peaks indicate that the dominant sources of dust in Baode were the CAOB areas and the Mu Us Cretaceous sandstone/eastern Mu Us to the north and northwest of the CLP, but the presence of the 500–400 Ma ages indicates that material deriving from the Northern TP, YR, and possibly from Tarim is also present at the site (Shang et al., 2016). The larger grain size of the Baode RC, however, implies a more proximal dominant source of dust when compared to the RCs in the southern sites at Lantian and Dongwan (Shang et al., 2016).

Similarly to Baode, the 11–2.6 Ma [Xu et al., 2009; debate also exists over whether the basal age of the Shilou RC is 11 Ma (Xu et al., 2009), 8.2 Ma (Ao et al., 2016) or 5.2 Ma (Anwar et al., 2015)] Shilou RC in the eastern CLP, west of the Lüliang Mts. (Figs. 11 and A1), shows prevailing 300–200 Ma, 2000–1500 Ma, and ca. 2500 Ma ages (Fig. 6). According to Pan et al. (2018), the data do not show significant input from distal western sources, such as Taklamakan Desert or the Qaidam Basin, but they claim that the older units (10.2 and 6.4 Ma) in Shilou show similar zircon U-Pb age spectra to the Junggar Basin, Gobi Alxa arid lands (Gobi Altai Mts. piedmont in Fig. 5), and to the western Mu Us. The latter seems plausible, because the presence of the ca. 1.8 Ga and 2.5 Ga age peaks, especially in the oldest unit, would suggest a more proximal source from the NCC (Section 5.1). However, the western Mu Us (and to some degree the Gobi Alxa arid lands) has a strong 500–400 Ma age component, which is very weak in the oldest Shilou sample (Figs. 5 and 6), although this western Mu Us peak represents input from the YR, which may not have existed in the Miocene. The low number of zircon age data from Shilou may also lead to underrepresentation of some age peaks. Pan et al. (2018) also report that the grain size of the RC increased after 5.7 Ma and, based on zircon data, the source areas changed to more proximal regions: the eastern Mu Us Desert, the middle reaches of the YR, and the Lüliang Mts, which they propose to have rapidly uplifted at ca. 5.7 Ma.

In the central CLP, a limited amount of zircon U-Pb data has been published from the Luochuan and Xifeng RC deposits. Liu et al. (2019) reported zircon ages from a 2.7 Ma unit in Luochuan and from 3.8 Ma

and 6.2 Ma units in Xifeng. Their results show that both the 500–400 Ma and the 300–200 Ma age peaks are present in all these RC units, and that the former age peak may be higher, although the low number of zircon ages hampers the inferences made from the relative heights of the peaks. Slight differences in the Xifeng samples can be seen in the lower proportion of ca. 350 Ma grains, and the higher proportion of ca. 500 Ma ages in the younger unit. Combined with heavy mineral analysis and a closer look at U-Pb dated euhedral zircons, Liu et al. (2019) suggest a wide geographical source area for the RCs, which includes the YR, the Qilian Mts., the Mu Us, Tengger and Badain Jaran Deserts, and possibly the Tianshan-Altai-Gobi igneous rocks.

The Chaona RC in the central CLP has by far the most published zircon data and the only RC data set with consistent high-*N* zircon age data for the same site, allowing a reliable comparison of the relative heights of the age peaks. The RC has a basal age of ca. 8.1 Ma (Song et al., 2000). The proportion of 300–200 Ma and 2750–1500 Ma ages compared to the 500–400 Ma ages is relatively lower in the 8.1 Ma and 5.8–4.4 Ma units than in the 7.7–6.2 Ma and 3.8–2.9 Ma units (Fig. 6; Nie et al., 2018). According to Nie et al. (2014a) the lowermost unit shows a mixed source from the nearby Liupan Mts. that was rapidly exhumed at ca. 8 Ma, and from Qaidam Basin, based mostly on the high 450–400 Ma age peak. Later, Nie et al. (2018) argued that the distant Taklamakan Desert and other distant central Asian areas are unlikely to be the main sources of RC of any age. Instead, they suggest a mix of two main sources for the dust: Qaidam Basin/Gobi (Qilian Mts.) and the middle reaches of YR/eastern Mu Us Desert. Increased input from the latter is indicated by the time intervals of higher relative 300–200 Ma and 2750–1500 Ma age proportions, which also correspond with higher dust accumulation rates in the CLP and North Pacific Ocean and with periods of intensified monsoon precipitation (Nie et al., 2018).

The Lingtai RC site is located close to Chaona and Xifeng (Fig. 1) and dates back to ca. 7.0 Ma (Ding et al., 1998b). The zircon U-Pb age data show significant variability between the 7–3 Ma units (Fig. 6). The lowermost Lingtai units (7.0 and 6.0 Ma) and the youngest (3.0 Ma) unit show high 300–200 Ma age peaks, indicating a strong input from northern source regions (Gong et al., 2017). Even older age peaks of 900–600 Ma, 2000–1500 Ma, and ca. 2500 Ma are present in the 6 Ma unit, which may indicate zircons derived from the nearby Liupan Mts. and NCC (Fig. 5). The 5.5 Ma Lingtai RC unit shows similar results to the roughly coeval samples from Chaona, with a high 500–400 Ma age peak, suggesting dominant western sources. For the older units, Gong et al. (2017) argue that the strong signal from the northern sources may have been caused by decreased dust availability in the western source regions as a result of high humidity before ca. 5.5 Ma. Both Nie et al. (2014a) and Gong et al. (2017) note that the Tarim Basin became more arid at ca. 5.3 Ma according to Sun and Liu (2006) and Liu et al. (2014c), which would have increased the dust availability there and subsequently resulted in increasing dust transport to the CLP. Surprisingly, the dominant 300–200 Ma age peak in the 3.0 Ma unit at Lingtai differs from the coeval Chaona unit, which has a higher 500–400 Ma age peak. Gong et al. (2017) do not discuss the possible reasons for this, but point out that the relatively low number of the analysed zircon ages may be a factor.

Compared to most of the other sites, a significant amount of variation is seen in the zircon age spectra of the southernmost RC site in Lantian. The oldest RC samples in Lantian have a depositional age of ca. 7.2 Ma (An et al., 2000). Many units show a dominant peak at ca. 160–130 Ma (Fig. 6), which is either absent or not as strongly present in the other sites. All the units also have a high peak in the age range of ca. 550–350 Ma. The 4.99 Ma and the 4.2 Ma units, which were reported by Shang et al. (2016), show this peak at the slightly older side of the age range (Fig. 6), which may be caused by the low number of zircon ages in each of these units. A minor peak in the age range of 350–200 Ma is observed in almost all samples, except the oldest RC unit. According to Zhang et al. (2018a), the ca. 160–130 Ma and ca. 550–350 Ma peaks correspond to sources from the North QOB., although the latter peak can also be explained by western sources. Furthermore, Zhang et al. (2018a) designate the ca. 350–250 Ma ages to the arid regions between the Gobi Altay Mts. and northeastern TP (Tengger and Badain Jaran Deserts, CS Mongolia, and Gobi Altay Mts. piedmont in Fig. 5), and the 250–200 Ma ages to the NE TP itself. Zhang et al. (2018a) also suggest that there was an expansion of the source regions after 7.2 Ma, based on the zircon age distributions.

The westernmost RC site in Dongwan has a dominant western source signal at 5.47–5.26 Ma, with abundant 500–400 Ma detrital zircon ages (Shang et al., 2016). The low number of reported zircon ages limits the interpretation between different units in Dongwan, but the smaller grain size of the Dongwan RC compared to Lantian seems to imply distant sources, possibly the recently formed arid Taklamakan Desert (Shang et al., 2016).

More general observations on the spatiotemporal RC provenance variations can be made when the zircon age data are grouped by site (Fig. 7) and by depositional age (Fig. 8). It is important to note that the interpretations from the grouped RC data will be dominantly influenced by sites that are represented by the most zircons. In this sense, and given the spatial variability of zircon ages in the RC, the grouped data should not be viewed as representative of the average distribution of the RC as a whole. In particular, Chaona ($n = 5642$) and Lantian ($n = 1297$) together make up around three quarters of the data, and Chaona alone, more than half. As such, these RC data are heavily biased to these sites, which in turn may make it harder to define overall differences between the loess and RC. The same is also the case of the loess data (Figs. 8 and 9), which are also dominated by large data sets from a few sites.

The spatial distribution of grouped RC zircon ages (Fig. 7) shows that the northern/northeastern CLP RC sites (Baode and Shilou) have a distinct source signature from the southern/southwestern sites (Luochuan, Xifeng, Chaona, Lingtai, Dongwan, and Lantian). The southernmost site, Lantian, is strikingly different from the other sites with the very low 300–200 Ma peak, and a strong peak at 160–130 Ma, which is explained by the QOB source from the south. Shilou on the other hand has a very low 500–400 Ma age peak compared with the other sites. The northernmost sites, Baode and Shilou, are the only sites where the 300–200 Ma peak is higher than the 500–400 Ma peak. In addition to receiving material from the northern/northwestern sources, one potential explanation for this is that for Baode, the Mu Us Desert would act as a western source, while for the other sites, it lies to the north, and would be a northern, northwestern (Shilou) or even a northeastern (Dongwan) source. As such, the dominant winds at Baode may have also been westerly rather than northerly, as with other sites, and the abundance of 300–200 Ma ages could be explained by input from the eastern Mu Us, where those ages are prevalent (Fig. 5). As discussed by Shang et al. (2016), this is supported by the silt-dominated grain size of the Baode and Jingle RC. Baode RC also has a significant 500–400 Ma age peak, which indicates that western distal sources, or the western Mu Us, may also have contributed material to this site. However, it is unclear whether the Mu Us Desert had formed already in the Neogene. In the absence of a desert, river systems would have been able to provide dust to the CLP.

The Lingtai and Lantian RC have a younger age peak (at ca. 400 Ma) than the other southern sites in the 500–400 Ma age range (Fig. 7). In Lingtai, this was explained by sources from the Liupan Mts., while in Lantian, it can be explained by sources from the North QOB. The older early Palaeozoic peak at ca. 450 Ma in the other southern RC sites corresponds better to the western sources from CCO and/or Tarim Basin (Fig. 5).

The Neoproterozoic ages of ca. 1000–800 Ma are most abundant in the Baode, Chaona, and Dongwan sites, although all RC sites have some zircons of this age range. These zircons may initially be sourced from the SGC via the YR as discussed in Section 7, or from Liupan and Qinling Mts. for Chaona and Dongwan. In Baode, northwestern sources from CAOB, e.g., the Tianshan and the CAOB terranes in Mongolia, could also explain these zircon ages (Table 1). Both the Tianshan and CS Mongolia

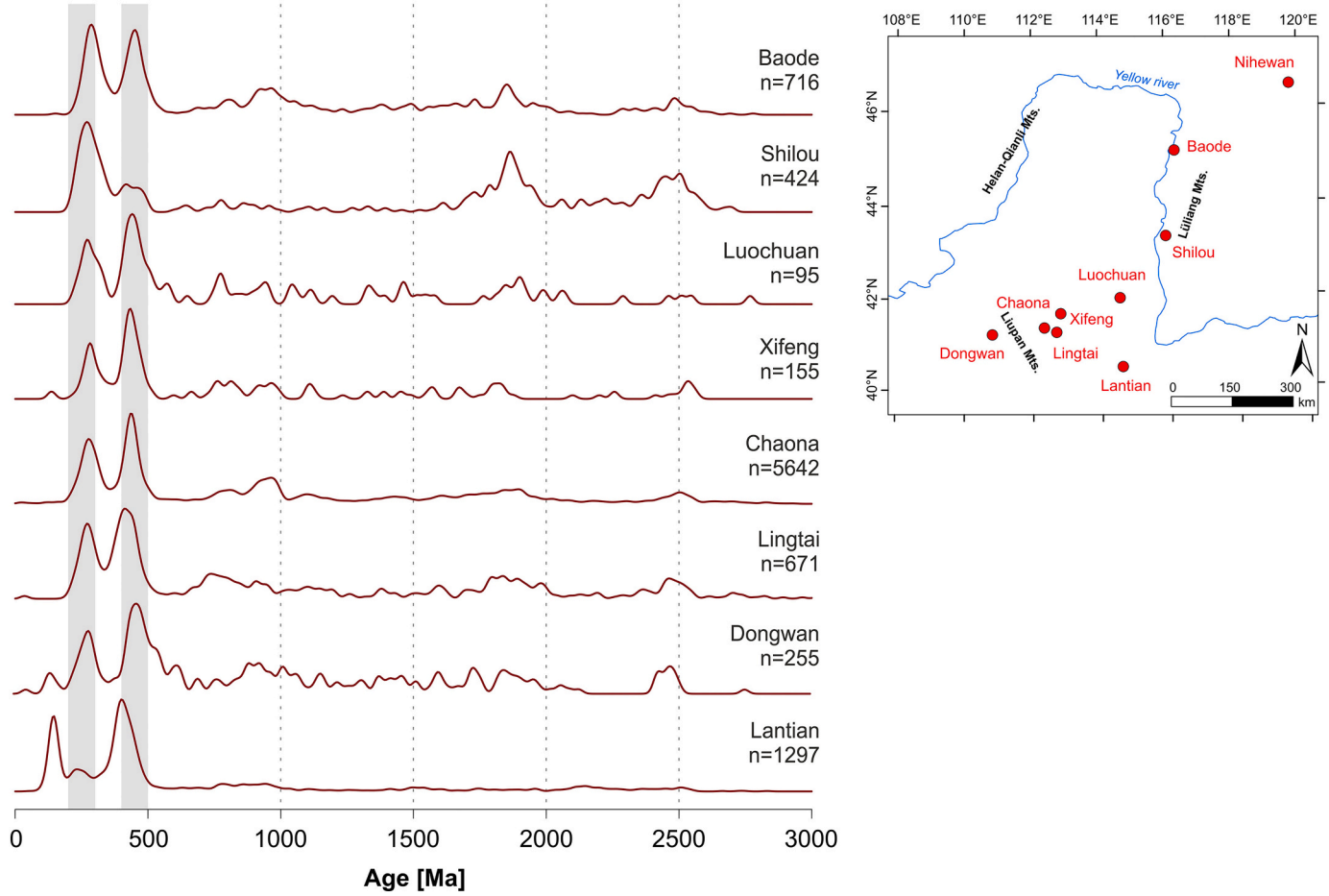

Fig. 7. KDEs of the Red Clay zircon U-Pb ages grouped by site and the locations of the RC sites discussed in this paper. The grey bars indicate the age ranges 300–200 and 500–400 Ma. Data are from: Shang et al. (2016; Dongwan, Baode, Lantian), Gong et al. (2017; Lingtai), Nie et al. (2018; Chaona), Pan et al. (2018; Shilou), Zhang et al. (2018a; Lantian), and Liu et al. (2019; Xifeng, Luochuan). The northern sites (Baode and Shilou) have higher 300–200 Ma age peaks than the 500–400 Ma age peaks, which likely reflects dominant dust sources from the CAOB and eastern Mu Us. Shilou also received material from the proximal Lüliang Mts. (TNCO). The southern/southwestern RC sites show a significant peak at 500–400 Ma, indicating dominant western sources from the CCO and/or Tarim, or from the northwest via the western Mu Us. In Baode, this age peak could be explained by a westerly source from the western Mu Us. The Lantian site differs from the other sites by almost lacking the 300–200 Ma age peak, by showing a high ca. 160–130 Ma peak, and by showing a younger early Palaeozoic age peak (at ca. 400 Ma) than the other sites, all of which can be caused by dominant sources from the North QOB (Zhang et al., 2018a). (For interpretation of the references to colour in this figure legend, the reader is referred to the web version of this article.)

have low Neoproterozoic age peaks in their detrital zircon age spectra (Fig. 5), and in CS Mongolia these ages may be underestimated because of the low number of analyses. In general, there are very few detrital zircon studies from the southern Mongolian drylands, which hampers the understanding of this region as a potential source area for the CLP sediments.

When the grouped data set from the Neogene RC is compared with the Quaternary loess (Fig. 9), there seems to be only slight differences in the source signal based on the zircon age distributions. The main differences are that the loess has higher components of grains <100 Ma, as well as broader ca. 300–200 Ma and 500–300 Ma age peaks than the RC. Potentially the 500–300 age peak is slightly younger in the loess than in the RC, and the Archean-Proterozoic age peaks are slightly larger in the RC. This similarity of the zircon ages between the RC and loess supports previous studies (e.g. Bird et al., 2020; Chen and Li, 2013; Nie et al., 2013) that indicate no significant change in dust provenance across the Neogene-Quaternary boundary.

A closer look at the temporal variation across the RC sites is shown in Fig. 8. Note that the oldest, 10.2 Ma RC is a single sample from Shilou, and the second oldest group of samples (8.1–7.7 Ma) are samples only from Chaona. Ignoring the 10.2 Ma Shilou sample, the 500–400 Ma age peak remains quite constant throughout the RC deposition, suggesting that input from western sources has been present since at least 8.1 Ma (Fig. 8). The ages at ca. 400–350 Ma increase in the youngest (3.5–2.7 Ma) RC deposits and resemble the Quaternary loess, although the increase in those ages is mostly due to the samples from Lingtai and Lantian. The most prominent changes are seen in the 300–200 Ma and the <200 Ma age peaks (Fig. 8), of which the latter are shown only from Lantian, Dongwan, and Xifeng sites. During 8.1–6.6 Ma, the 300–200 Ma age peaks are lower in height than in the subsequent time period of 6.56–6.19 Ma. During 6–5.47 Ma the peak again becomes lower in height, after which, the relative amount of the 300–200 Ma ages starts to increase towards the Quaternary, which could be interpreted to reflect the strengthening of the EAWM and/or the increased dust availability in northern source regions (Gong et al., 2017), where zircons of these ages are particularly well expressed.

9.2. *Provenance of the Red Clays: summary from published data*

From the previous provenance studies and the analyses presented above, it is clear that the Neogene RC dust has originated from multiple sources and that the sources lie mostly to the west and northwest of the CLP. While the RCs certainly record a mix of sources, the secondary source areas also likely received material from multiple primary and

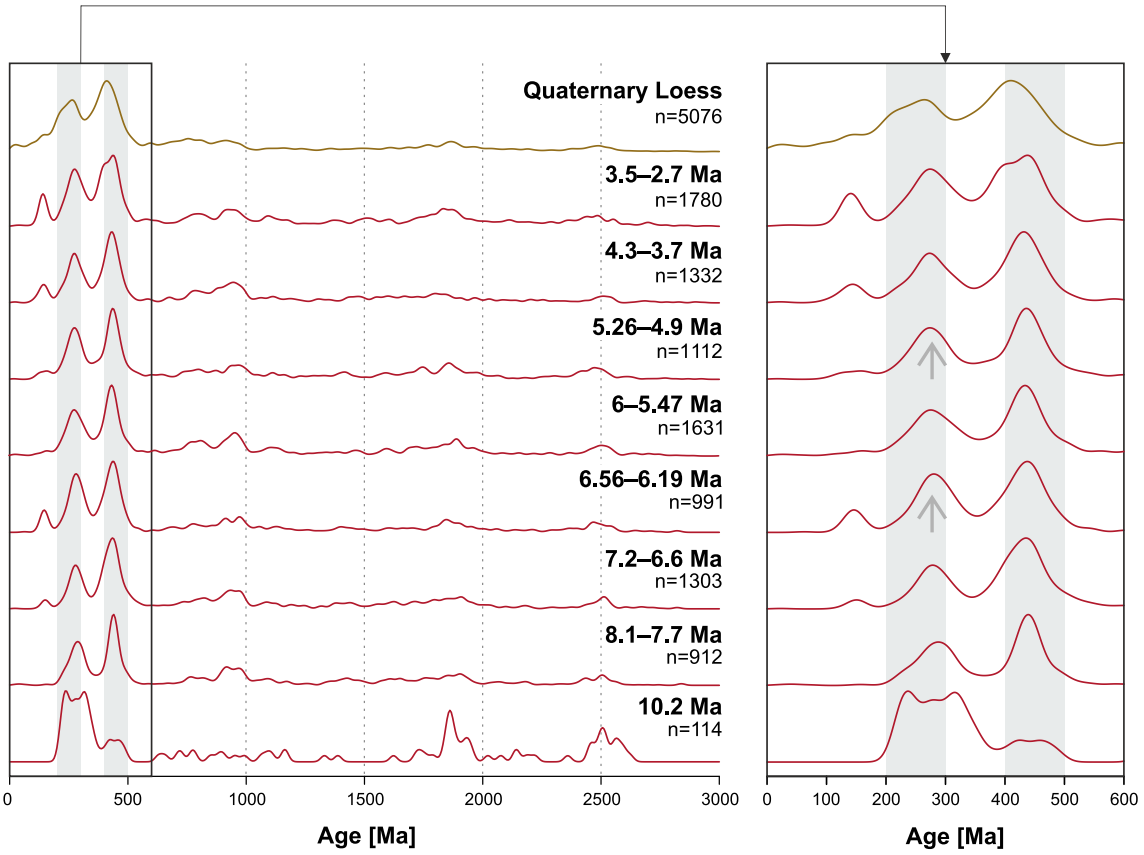

Fig. 8. Temporal variation of the Red Clay zircon U-Pb age distributions. The loess data are included for comparison. The grey bars indicate the age ranges 300–200 and 500–400 Ma. The increase in 300–200 Ma ages is indicated by arrows. Loess data from: Pullen et al. (2011), Bird et al. (2015), and Zhang et al. (2018a). Red Clay data from: Shang et al. (2016; Dongwan, Baode, Lantian), Gong et al. (2017; Lingtai), Nie et al. (2018; Chaona), Pan et al. (2018; Shilou), Zhang et al. (2018a; Lantian), and Liu et al. (2019; Xifeng, Luochuan). Note that the oldest sample is a single sample from Shilou and the second oldest group contains samples only from Chaona. Most changes in the age distributions are seen in the 300–200 Ma ages, which increase in the 6.56–6.19 Ma and 5.26–4.9 Ma groups and remain relatively high towards the Quaternary. (For interpretation of the references to colour in this figure legend, the reader is referred to the web version of this article.)

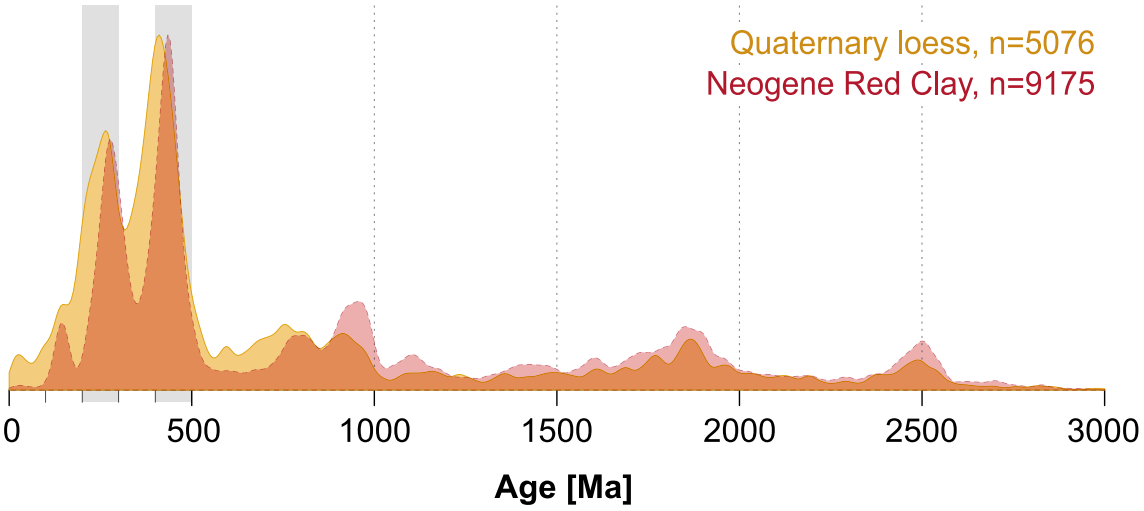

Fig. 9. KDEs of the grouped Red Clay (red) and loess (yellow) zircon U-Pb ages compared. The grey bars indicate the age ranges 300–200 and 500–400 Ma. Loess data from: Pullen et al. (2011): Heimugou; Bird et al. (2015): Jingbian, Beiguoyuan, and Lingtai; and Zhang et al. (2018a): Lantian. Red Clay data from: Shang et al. (2016; Dongwan, Baode, Lantian), Gong et al. (2017; Lingtai), Nie et al. (2018; Chaona), Pan et al. (2018; Shilou), Zhang et al. (2018a; Lantian), and Liu et al. (2019; Xifeng, Luochuan). (For interpretation of the references to colour in this figure legend, the reader is referred to the web version of this article.)

secondary source regions, which complicates the RC source interpretation. Based on the observations from the data above we can make some basic interpretations of general provenance trends in the RC.

The spatial differences in the RC provenance are especially clear when comparing the detrital zircon U-Pb ages from the northern RC sites (Baode, Shilou) to those of the more southern sites (Luochuan, Xifeng, Chaona, Lingtai, Dongwan, Lantian; Fig. 7). The northern RC sites seem to have more influx from northern sources (CAOB and NCC), which is indicated by the high 300–200 Ma age peaks and the relative abundance of the Archean and Palaeoproterozoic ages, while the southern sites show dominance of western sources indicated by the high 500–400 Ma age peaks. These inferences are supported by the NW/N-SE/S trending decrease of grain size, implying that low-level northerly/northwesterly winds dominated dust transport during the Neogene, and that the EAWM pattern already existed in the late Pliocene (Han et al., 2007; Miao et al., 2004; Wen et al., 2005; Zan et al., 2018). A W-E trend is also seen when the grain sizes of the western CLP RC deposits in Linxia Basin (Fig. A1) are compared to the more eastern CLP sites (Lingtai, Lantian), which implies that a W-E wind component also existed in the late Pliocene (Zan et al., 2018). The combined zircon U-Pb data in Fig. 8 support a westerly wind component since at least 8.1 Ma (see discussion below). Dust trajectory modelling by Shang et al. (2016) additionally shows that the northerly winds may have been more dominant in transporting dust to Baode than to Lantian, Dongwan or Chaona, whereas the proportion of trajectories crossing the western deserts (Tarim and Northern TP) increases from Baode to Lantian to Chaona/Dongwan. However, the proportion of the EAWM vs. other northwesterly/westerly winds as the transporting agent, remain poorly understood.

Another ambiguity that remains is the proximity of the western sources. As shown in Figs. 8 and 9, the early Palaeozoic age peak (ca. 450–420 Ma) seems to be the most prominent and quite stable source signal since at least 8.1 Ma. Thus, western sources, whether distal or more proximal, have been significant during this time period. A proximal source may be the western Mu Us Desert, which shows high abundance of the early Palaeozoic ages (Figs. 4 and 5). However, the environmental-sedimentary nature of this area during the Neogene is unclear. Furthermore, the present-day west Mu Us zircon age spectrum is highly influenced by sediment influx from the YR (Stevens et al., 2013). However, it is uncertain whether this system had been formed in the Neogene, although Lin et al. (2001) suggest the YR bend around the Ordos Block formed in late Miocene-early Pliocene, and Wang et al. (2019) demonstrate YR transport of sediment to the nearby Yinchuan Basin from at least 3.3 Ma. Recently, Zhang et al. (2021b) also showed evidence that a similar upper-middle YR fluvial system as seen today had already formed by ca. 5 Ma. Alternatively, dust may have been transported from the sources in the CCO or even further afield in the Tarim Basin, both of which also show a high peak at 500–400 Ma. As discussed in Section 5.6, the NE TP rapidly uplifted at 8.1 Ma producing an increase in the sedimentation rates in Qaidam Basin (Cheng et al., 2021; Fang et al., 2007), which may have also increased dust transport from the CCO to the CLP. In terms of Tarim Basin, it is not well understood whether the distal basin acted as a coarse dust source, as it is an enclosed basin where only high elevation suspended dust can travel far afield (Sun, 2002), although since the finer grain sizes of the RC deposits compared to loess seem to indicate a longer transport for the Neogene dust (Yang and Ding, 2004), this may well be the case. To resolve these ambiguities and develop a better understanding of the proximity of the possible western sources, a distinction of the distal and proximal western source area signals is required, which is not possible with the zircon ages, since the CCO and Tarim sources share very similar age distributions (Fig. 4). In Section 6, we showed that these areas have distinct metamorphic natures in terms of formation temperatures (Fig. 3), and as such, metamorphic mineral tracers, such as detrital rutiles, could as such be used to discriminate the two potential western sources.

The temporal variations in the wind directions during Neogene are even less understood than the spatial variations. Excluding the 10.2 Ma Shilou sample, Fig. 8 shows that most changes in the 500–200 Ma zircon U-Pb ages of the RCs occur in the 300–200 Ma age component. The 500–400 Ma age peak shows only slight change in the youngest RC units (3.5–2.7 Ma), where the peak widens and gets younger, and starts to resemble the Quaternary loess (Fig. 8). The 300–200 Ma ages, on the other hand, show relatively higher proportions during 6.56–6.19 Ma and from 5.26 Ma onwards, and relatively lower proportions during 8.1–6.6 Ma and 6–5.47 Ma (Fig. 8). However again, based on the zircon ages alone, it is not possible to trace these changes to specific source areas, as the 300–200 Ma age peaks are present in various sources north, west and south of the CLP (Fig. 4). Either a more detailed study on the specific zircons (e.g. Hf isotopes), or potentially another single-grain provenance proxy such as the rutile geochemical analysis addressed in this paper, is needed to better understand the sources that produce the 300–200 Ma signal in the zircon age distributions, and thus to better understand the possible temporal variations in the RC source(s). The parts of the CAOB discussed in this paper are usually considered the main source for the 300–200 Ma zircon age component. This area has a relatively dominant medium-temperature greenschist to amphibolite facies metamorphic nature compared to the more diverse western source areas (Fig. 3). However, its distal western parts in South Tianshan have distinct low temperatures and this “cool” trend continues further east in the NQO in the CCO. In the NE CAOB, on the other hand, the NE China Khondalite Belt could provide high-temperature metamorphic signals to sources to the northeast of the CLP, although the zircons from the NE China deserts do not have a strong early Palaeozoic age signal that would correspond to the age of the belt (Figs. 4 and 5). Despite the uniform medium-temperature signal from the southern Mongolia and northern China CAOB, in the more proximal northern/northwestern source regions, the NCC has multiple high-grade metamorphic terranes or complexes, of which the KB is unique in its abundant UHT localities (Section 6). Combined with zircon age data, Zr-in-rutile temperatures of detrital rutiles could be used to pinpoint this northern/northwestern source area that, according to the Palaeoproterozoic zircon ages, is likely present at least in the signal from the eastern Mu Us, the Cretaceous sandstone in Mu Us, and the middle reaches of the YR (Fig. 5).

A further major question in provenance of the aeolian CLP sediments also remains over whether the transition from the Neogene to Quaternary was marked by a shift in dust source(s) in the RC to loess. Whole rock geochemical provenance studies by Sun (2005), Sun and Zhu (2010) and to some extent Xiong et al. (2010) suggest a provenance shift did occur at the Pliocene-Pleistocene transition, while Wang et al. (2007), Chen and Li (2013) and Bird et al. (2020), as well as heavy mineral studies by Nie et al. (2013) and Peng et al. (2016), argue that no provenance change occurred. Quartz-based tracers also imply no major provenance change occurred during the Pliocene-Pleistocene transition (Ma et al., 2015), although quartz $\delta^{18}O$ values indicate some changes in the composition of the source systems at 2.6 Ma (Hou et al., 2003; Yan et al., 2017). The grouped data of RC and loess in Fig. 9 indicates slight differences in the sources of the two deposits, although the grouping of data may be problematic, especially in biasing the RC data towards the Chaona zircons as addressed earlier. The loess shows higher proportions of <100 Ma, ca. 250–200 Ma and 400–300 Ma ages than the RC, and the 500–400 Ma age peak is slightly younger in the loess than in the RC (Fig. 9). These variations are, however, smaller than those variations observed within the RC through time and between sites across the CLP, and the small differences between the loess and the RC could also derive from laboratory calibration procedures. Zircon U-Pb studies that have analysed samples from both RC and loess from the same site, generally indicate only slight changes in the age distributions (Liu et al., 2019; Nie et al., 2018). One exception is in the southernmost site in Lantian, where the distal sources from the arid regions between the Gobi Altay Mts. and NE TP seem to have become more significant in the Quaternary than they were in the Neogene, based on clearly increased proportion of ca. 280–270 Ma ages (Zhang et al., 2018a). Whether the overall small

changes in the zircon age spectra between the RC and loess reflect true changes in provenance at the Neogene-Quaternary transition, or only the result of spatial variation and uneven sampling, is left unanswered.

In sum, the specific ambiguities introduced here cannot be solved by any amount of zircon U-Pb age data alone. However, because of its ability to detect multiple mixed sources, a single-grain method is justified for detailed provenance analysis of the CLP dust. The ambiguities of the zircon U-Pb data can be explained by not only the scarcity of high-*N* data, but also by the overlapping main periods of tectonic activity in the potential primary source regions of the CLP dust. From the geologic history outlined above, we know the closures of the PAO and the Palaeo-Tethys Ocean partly overlap, resulting in late Palaeozoic to early Mesozoic ages in most source areas (Fig. 5). We also know that the CCO mostly formed in the early Palaeozoic, but parts of the CAOB were also active during that same time period. Although a rough division can be made between western source areas with dominant 500–400 Ma ages (Tarim and Altyn Tagh, CCO) and north/northwestern source areas with dominant 300–200 Ma ages (CAOB), these age components are more or less present in most of these source areas (Fig. 4), which makes it difficult to distinguish the relative proportion of dust input from those sources, and statistical unmixing tools that may be able to do this (Licht et al., 2016; Zhang et al., 2021a) require high-*N* data which at the present is not available for the majority of RCs. However, these source areas with similar age distributions have largely experienced different metamorphic conditions during their formation (Section 6). Although zircon can be a high-grade metamorphic mineral and therefore could also be used to address the metamorphic source signal, the very fine grain size of the RC sediments normally limits the number of analyses to only one analysis per grain if using laser ablation methods. Furthermore, zircons bias the results towards intermediate and felsic rocks. Therefore, a multi-proxy single-grain approach with both igneous and metamorphic minerals would be preferable. Rutile, a predominantly metamorphic mineral, has multiple applications for provenance, e.g. geothermometry and lithological classification of the metamorphic protolith. The similar physical properties of zircon and rutile also enables a relatively easy simultaneous preparation of the two minerals for analyses. For these and above discussed reasons, we suggest the use of joint detrital rutile geochemical and zircon U-Pb analysis for provenance studies of the CLP dust in order to overcome limitations in existing data and resolve the outstanding questions over loess and RC provenance. In the next section, this joint method is tested to analyse the provenance of the Nihewan RC in northern CLP and to demonstrate the potential of this approach.

10. Nihewan Red Clay provenance

10.1. Geologic background and sampling

The Nihewan Basin lies on the northeastern margin of the CLP (NW in Fig. 1) and is famous for yielding rich early Pleistocene mammalian fauna and Palaeolithic sites (Barbour, 1924, 1925; Barbour et al., 1926). The basin is part of the Fen-Wei Graben system covering an area of ~150–200 km^2, and is filled with more than 150 m of Cenozoic aeolian, fluvial and lacustrine deposits exposed along the banks of Huliu and Sanggan rivers (Cai et al., 2013). The Cenozoic sediments in the Nihewan Basin are clustered in four units, the early Pliocene "*Hipparion*" RCs of the Shixia Formation (Barbour, 1925; Huang and Guo, 1981), late Pliocene fluvio-lacustrine and palustrine Daodi Formation (Du et al., 1988), Pleistocene fluvio-lacustrine Nihewan Formation and the overlying Malan loess. The Shixia Formation unconformably rests on the crystalline basement rocks and consists of dominantly silts and clays with distinctive red colouration and carbonate nodule rich horizons, reminiscent of Neogene RC deposits on the CLP. The high degree of similarity of the REE patterns between the Shixia RCs and those from the CLP (Liu et al., 2018), as well as grain sizes and lack of hydraulic structures support an aeolian origin for the fine-grained sediments of the Shixia Fm.

A sediment sample was collected from the Shixia RC (N40° 15.754′; E114° 43.801′) close to Shixia village, located in the northeastern Nihewan Basin, on the northern side of the Sanggang River and ~ 1.5 km southeast of the Xiashagou, where the Nihewan Fauna (*sensu stricto*) was initially reported by Teilhard de Chardin and Piveteau (1930). Approximately 4 kg of sample was collected from a homogenous clayey silt overlain by a calcareous horizon composed of $CaCO_3$ nodules a few cm in diameter. The clayey siltstone is massive, slightly calcareous and shows a deep red colour (Munsell 5YR 5/4) (Fig. 10) with subtle traces of Fe-Mn staining. The magnetostratigraphy of Liu et al. (2018) place the sampled level at chron C2Ar (4.19–3.6 Ma) at ca. 4 Ma. While there are no rutile data available from potential secondary sources, the location of the Nihewan RC is ideal for testing the novel rutile provenance proxy since there are four studies that have reported Zr-in-rutile temperatures from adjacent potential primary source areas, including the KB, the TNCO, and the northern margin of the NCC (Fig. 11).

10.2. Sample preparation and methods

The sample was wet-sieved at 20 and 500 μm and dried in oven at 50 °C for heavy mineral separation at the Mineral Separation Laboratory of Vrije Universiteit Amsterdam. The sample was then dry-sieved at 250 μm before using diiodomethane heavy liquids (2.89 and 3.31 g/m^3) and at 120, 90, 60, and 30 μm prior to using a Franz magnetic separator. The zircons and rutiles were randomly hand-picked from a low- or non-magnetic heavy mineral separate, and from size fractions 30—120 μm (zircons) and 30—90 μm (rutiles) under an optical microscope and mounted in epoxy and polished. The grains were then pictured and analysed by scanning electron microscope JEOL JSM-5900-LV (20 kV, 1 nA) at the Geological Survey of Finland (GTK), in order to ensure only zircons and rutiles were picked. From backscattered electron images (Figs. A6–A7) and qualitative element mapping (rutiles), areas free of zoning, visible inclusions and cracks were chosen for U-Pb (zircon) and trace element (rutile) analyses. The grain sizes of each grain were measured from optical microscope and backscattered electron images using the program Fiji ImageJ (Schindelin et al., 2012) (https://imagej.net/Fiji).

Zircon U-Pb and rutile trace element analyses were performed using a Nu Plasma AttoM single collector ICP-MS (Nu Instruments Ltd., Wrexham, UK) connected to an Analyte Excite 193 ArF laser ablation system (Photon Machines, San Diego, USA) at GTK. The zircon U-Pb analyses were run with a laser beam diameter of 25 μm, 5 Hz pulse frequency, and a beam energy density of 2.5 J cm^{-2}. Calibration standard GJ-1 (609 ± 1 Ma; Belousova et al., 2006), in-house standard A382 (1877 ± 2 Ma, Huhma et al., 2012) and A1772 (2711 ± 1 Ma, Huhma et al., 2012) were cyclically run during the analytical sessions. Using the software GLITTER™ (Van Achterberg et al., 2001), raw data were corrected for the background, laser-induced elemental fractionation, mass discrimination and drift in ion counter gains and reduced to U-Pb isotope ratios by calibration to concordant reference zircons. Common Pb correction according to the model by Stacey and Kramers (1975) was used when the analysis showed common Pb contents significantly above the detection limit (i.e., >50 cps). All the ages were calculated with 1σ errors and without decay constant errors. Similarly to the zircon data in Sections 7 and 9, a threshold of 1.0 Ga for the $^{206}U/^{238}Pb$ (<1.0 Ga) and $^{207}Pb/^{206}Pb$ (>1.0 Ga) ages, and a discordance filter of 10% were used. The detrital zircon ages are plotted as a KDE with a bandwidth of 15 Myr using the R package "provenance" (Vermeesch et al., 2016). With the same R package, a non-metric MDS map with Kolmogorov-Smirnov statistic was generated of the Nihewan and the potential source area zircon data (Section 7). The stress value of the MDS configuration was 7.6%, which indicates good fit of the data.

The instrument settings for the rutile trace element analyses were as follows: a 10 Hz pulse frequency, and a 5 mJ pulse energy at 30% attenuation were used to produce an energy flux of 2.0–2.5 J cm^{-2}. The

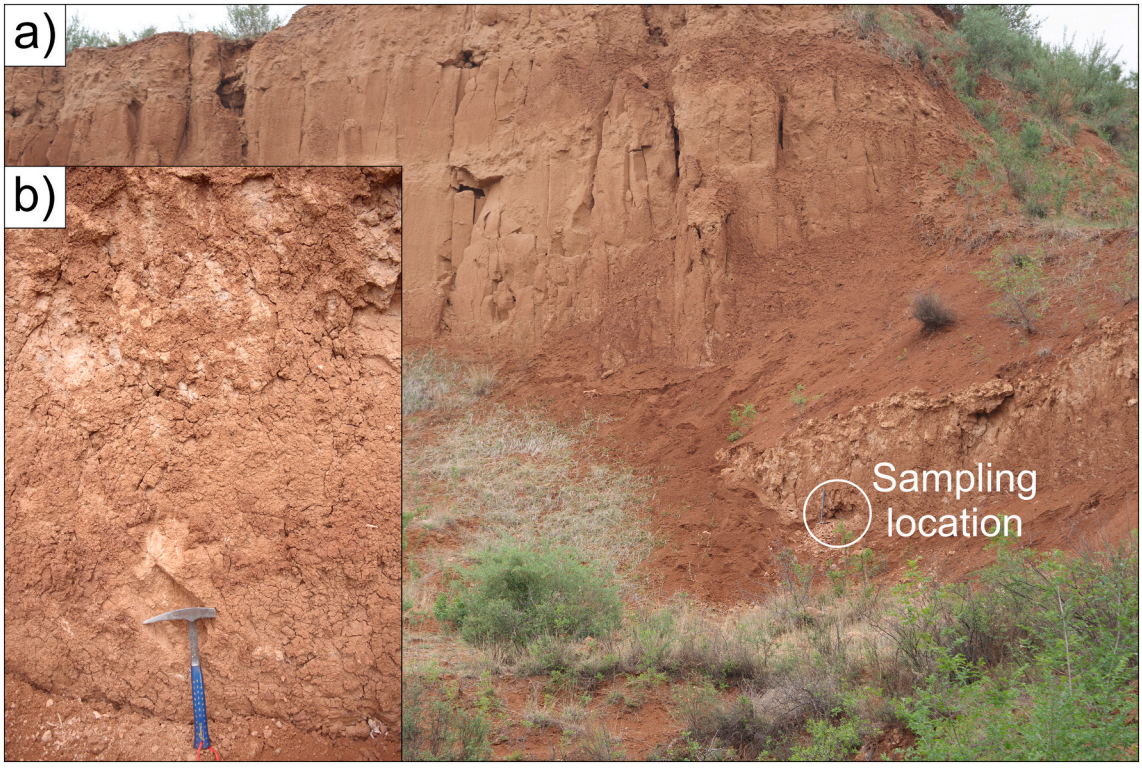

Fig. 10. a) Photo of the Nihewan Red Clay (Shixia Fm) sampling location. b) Close-up photo of the Nihewan Red Clay showing the massive structure of the sediment and the carbonate nodules. Photo credit: Arya Farjand. (For interpretation of the references to colour in this figure legend, the reader is referred to the web version of this article.)

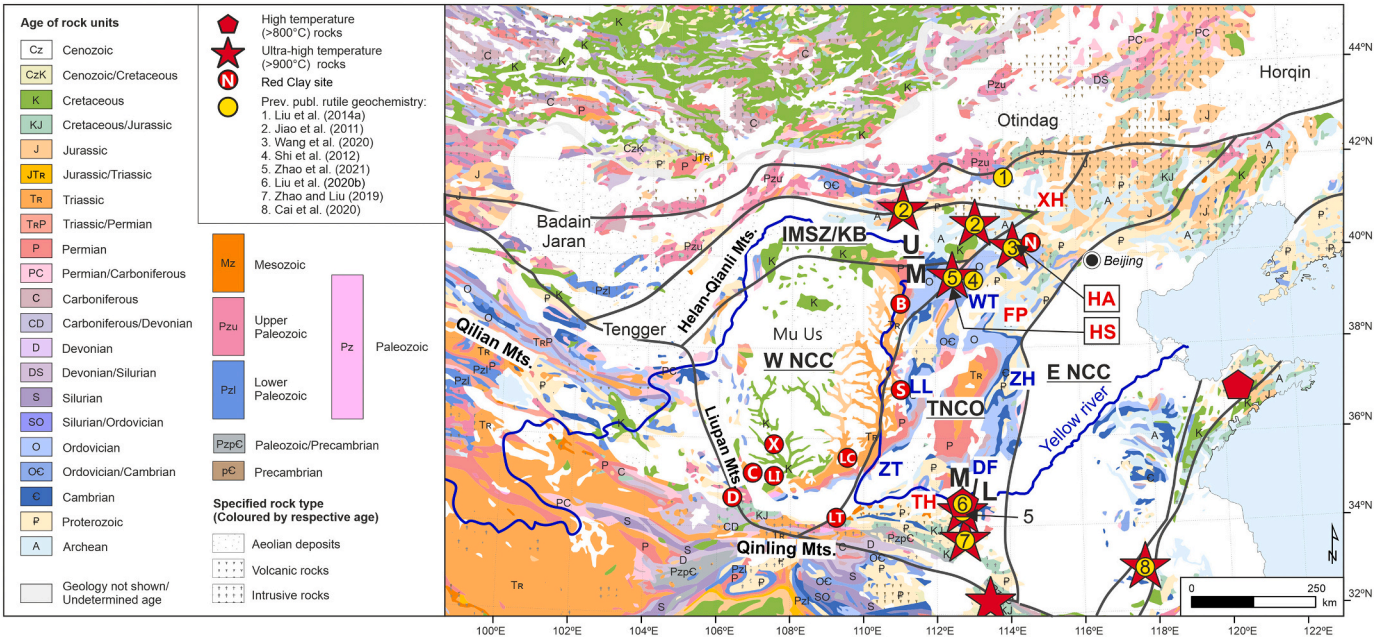

Fig. 11. Geologic map of the CLP and adjacent areas after Steinshouer et al. (1999). The upper (U), middle (M), and lower (L) reaches of the Yellow River are divided by black lines. The location of the East and West NCC, TNCO, and IMSZ/KB, which are the most relevant in terms of the provenance of the Nihewan RC, are indicated by dark gray lines. For the full set of labelled units/terranes see Fig. 2. Most Phanerozoic rock units in the TNCO are sedimentary unless otherwise indicated. High (low)-grade metamorphic complexes in TNCO are marked with red (blue) text: DF: Dengfeng, FP: Fuping, HA: Huai'an, HS: Hengshan, LL: Lüliang, TH: Taihua, WT: Wutai, XH: Xuanhua, ZH: Zanhuang, ZT: Zhongtiao. Red Clay sites: B: Baode, C: Chaona, D: Dongwan LC: Luochuan, LI: Lingtai, LT: Lantian, N: Nihewan, S: Shilou, X: Xifeng. The location of the Yellow River is figurative. (For interpretation of the references to colour in this figure legend, the reader is referred to the web version of this article.)

laser spot size was 20 or 25 μm, depending on the grain size. Due to the small grain size of the rutiles, only one measurement spot was used. Each analysis was initiated with a 20 s baseline measurement followed by switching on the laser for 40 s of sample signal acquisition. Analyses were made using time-resolved analysis with continuous acquisition of data for each set of points (2 standards, 15 unknowns, 1 quality control standard). The standard BHVO-2G was used as an external standard, and the standard BCR2-2G was used for quality control (Jochum et al., 2005; Schudel et al., 2015). The isotope ^{47}Ti was used as an internal standard for rutile. A value of 100% TiO_2 was allocated to each rutile for the calculation. The measurements were performed over 49 isotopes and 45 elements at low resolution (ΔM/M = 300) using the fast scanning mode. Data reduction was handled using the software GLITTER™ (Van Achterberg et al., 2001), which allows the baseline subtraction, the integration of the signal over a selected time resolve area, and quantification using known concentrations of the external and internal standards. Grains that showed high amounts (>10,000 ppm) of Si or Fe, and/or where mineral inclusions or a mix of multiple minerals could be detected in time-resolved analysis (Figs. A2—A3), were discarded as they were interpreted as signals deriving from other mineral phases than rutile. In addition, two rutiles showing high Si coupled with high Zr contents were also excluded from further analysis, because they may indicate the presence of zircon micro-inclusions in the rutiles, and result in false Zr-in-rutile temperature estimations. Discrimination between the TiO_2

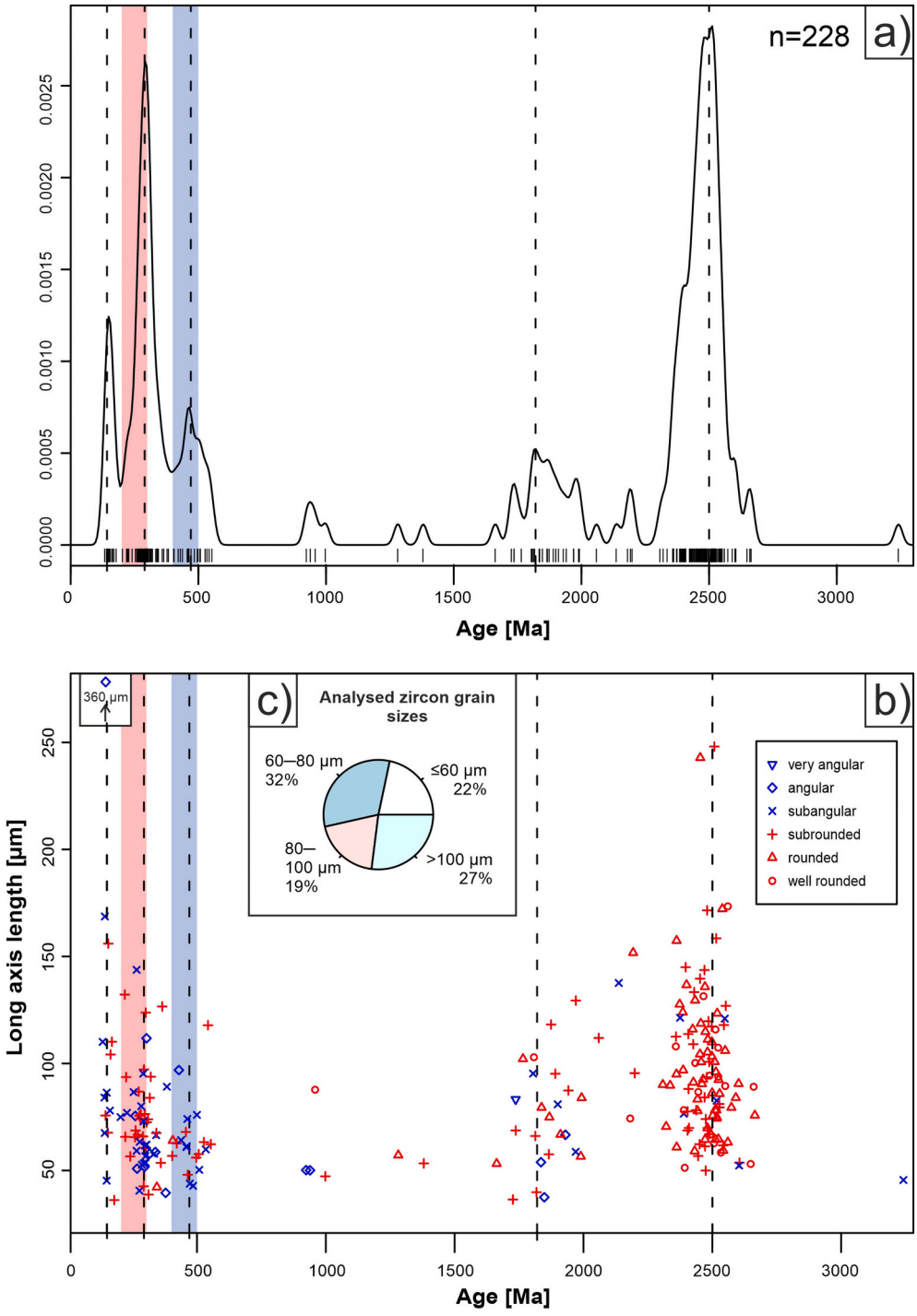

Fig. 12. The Nihewan RC zircon age data and morphology. The early Palaeozoic (500–400 Ma) age range is highlighted in blue colour, and the late Palaeozoic to early Mesozoic (300–200 Ma) age range in red colour. The dashed lines indicate the peaks of age populations at ca. 150 Ma, 290 Ma, 470 Ma, 1820 Ma, and 2500 Ma. a) KDE of the zircon ages. b) The grain size, morphology, and ages of the zircons. c) A pie chart of the grain sizes of the analysed zircons. (For interpretation of the references to colour in this figure legend, the reader is referred to the web version of this article.)

polymorphs rutile, anatase and brookite was made according to Triebold et al. (2011), by using the trace element concentrations of Nb, Cr, Sn, Fe, V, and Zr. Only rutiles were chosen for further data processing. Cr-Nb systematics by Triebold et al. (2012) were used to discriminate between metamafic and metapelitic rutiles. Zr-in-rutile temperatures were calculated after Tomkins et al. (2007) with a 10 kbar and α-quartz setting using the equation

$$T(^{\circ}C) = \frac{83.9 + 0.410P}{0.1428 - Rln[Zr(\text{ppm})]} - 273$$

where P is pressure in kbar and R is the gas constant, 0.0083144 kj K^{-1}. The same thermometer was used for the data from previous studies.

10.3. Results

Altogether 228 concordant detrital zircon ages were obtained from the early Pliocene Nihewan RC. The grain sizes of the zircons varied mostly from ~36 to 173 μm. Two grains had a long axis length of ~243 and 248 μm and one grain ~360 μm. The KDE of the detrital zircon U-Pb ages is shown in Fig. 12a. The dominant age populations are at ca. 2700—2300 Ma ($n = 106$, peak at ca. 2500 Ma) and at ca. 400—200 Ma ($n = 52$, peak at ca. 290 Ma), and minor populations occur at ca. 200—100 Ma ($n = 14$, peak at ca. 150 Ma), ca. 600—400 Ma ($n = 20$, peak at ca. 470 Ma), and ca. 2000—1700 Ma ($n = 23$, peak at ca. 1820 Ma). The youngest (<200 Ma), and the oldest (>2200 Ma) populations have the highest proportions of bigger grains (>80 μm), whereas the other populations are dominated by smaller (<80 μm) grains (Fig. 12b). It should be noted that 82% of >80 μm grains are sub-rounded, rounded or well rounded, implying aeolian origin or reworking (Garzanti, 2017), although roundness of the zircon grains may be also controlled by their age (Fig. 12b).

86 detrital rutiles were analysed from the Nihewan RC sample. The grain sizes vary from ~40 μm to 222 μm, but the majority are <80 μm. The rutiles have similar proportions of grain sizes analysed as the zircons from the same sample (Figs. 12c and 13a). Three out of 86 rutiles are metamafic according to the Cr-Nb systematics (Fig. 13d). The Zr concentrations of the rutiles varied from 7 to 4505 ppm, which correspond to metamorphic temperatures of 421—935 °C. Most of the >100 μm grains formed in granulite-facies (>750 °C) (Fig. 13c). It should be noted that the Zr concentration of rutile is not dependent on grain size (von Eynatten et al., 2005). Therefore, the high temperatures of the large detrital rutiles are likely representative of primary source rocks. This is supported by the observation that the second smallest grain (rutile No. 17, ~41 μm) in the data set of this study records one of the highest metamorphic temperatures (Zr = 4363 ppm, 931 °C; Fig. 13c).

10.4. Discussion

Since rutile data from potential secondary (sedimentary) source areas are lacking, the data and analysis of the potential primary source areas presented in Section 6 form the basis of the provenance interpretation from the rutile data. The aim of this section is to show the importance of understanding the geology of the primary source areas in provenance analysis by using these compilations. Another aim of this section is to show the potential of detrital rutile as a provenance proxy for the aeolian sediments on the CLP, as well as provide new insight into the provenance of the Nihewan RC. The Nihewan RC sample shows a relatively clear source signal in the zircon age spectrum, which leaves less room for speculation over the main source areas and therefore forms another good basis to test provenance interpretation from the novel rutile method. As we only present data from one RC unit, some of the problems discussed in Section 9.2 regarding the zircon provenance proxy cannot be addressed here (e.g. the temporal variation of the sources).

Our data from both zircons and rutiles are collected from relatively

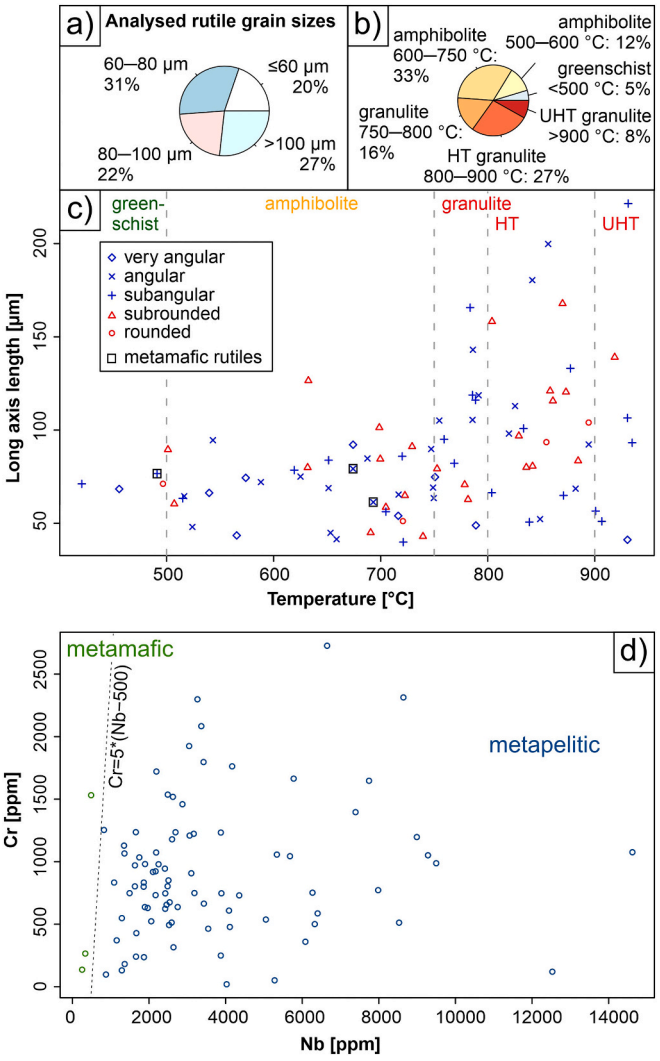

Fig. 13. The Nihewan RC rutile data. Pie charts of the a) grain sizes, and b) Zr-in-rutile temperatures (Tomkins et al., 2007) of the analysed rutile grains. c) The grain size, morphology and the Zr-in-rutile temperatures (Tomkins et al., 2007) of the rutiles. d) Cr vs. Nb concentration of the rutiles and source rock lithology according to Triebold et al. (2012).

coarse grains, which likely biases the results towards more proximal sources. However, coarse particles can be transported from distant sources via step-wise movement via multiple dust storms or via river transport. Furthermore, Van der Does et al. (2016, 2018) have shown that coarse (>63 μm) or even "giant" (>75 μm) dust particles can be wind-transported thousands of kilometres directly from source to sink, especially via dust storms. The single-grain detrital zircon provenance analysis by Nie et al. (2018) also indicated similar sources for the Chaona RC <20 μm and > 20 μm fractions. As such, we have not excluded the possibility of zircons and rutiles deriving from distal sources in our provenance interpretation of the Nihewan RC.

The detrital zircon ages from the Nihewan RC differ significantly from the other RC sites discussed in Section 9.1 by the greater abundance of the Archean-Palaeoproterozoic ages relative to Palaeozoic to late Mesozoic ages. Compared to the potential source areas, the zircon age distribution of the Nihewan RC (Fig. 12a) is very similar to that of the East and West NCC, the different samples from the Mu Us Desert, and the middle reaches of the YR (Fig. 5). The MDS map of the zircon data (Fig. 14a) support this and indicate E NCC, E Mu Us, the middle reaches of the YR, and Mu Us Cretaceous sandstone as the most probable sources for the Nihewan RC. At least for the Archean-Palaeoproterozoic (60%

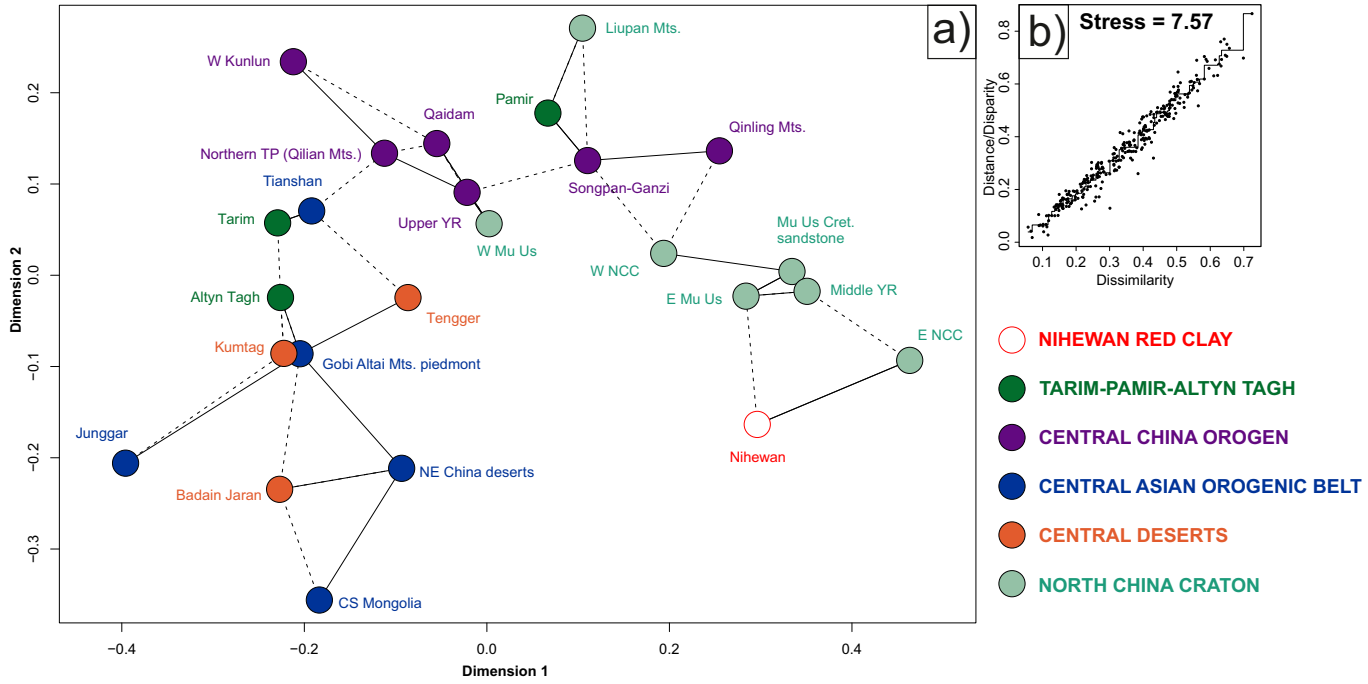

Fig. 14. a) Non-metric multidimensional scaling map of the Nihewan Red Clay and potential source area detrital zircon U-Pb data. Solid lines connect the nearest neighbours in Kolmogorov-Smirnov space and dashed lines connect the second-nearest neighbours. b) Stressplot of the fit. (For interpretation of the references to colour in this figure legend, the reader is referred to the web version of this article.)

>80 μm) and the Jurassic-Cretaceous (57% >80 μm) zircons, it seems indisputable that they derive from proximal sources on the NCC, since they consist mostly of zircons with large grain size and those zircon ages are consistent with the bedrock of the NCC and the rocks formed during the Yanshan Revolution (Section 5, Fig. 11).

The high age peak at ca. 400—200 Ma and the MDS map suggest material could be transported from the proximal E Mu Us, which is consistent with provenance interpretations from other northern CLP RC areas Baode and Shilou (Section 9.1). However, the Mu Us Desert lies southwest of the Nihewan RC, and there are no indicators of south-westerly winds in the Neogene. Other sources that could contribute to this ca. 290 Ma age peak in the Nihewan RC are the Upper and Middle YR (which likely existed in the Pliocene; Zhang et al., 2021b) and the central deserts west of Nihewan, or the CAOB sources further west/northwest, such as the Tianshan, Gobi Altay Mts. piedmont, CS Mongolia, NE deserts, and/or even Junggar and Tarim Basins (Fig. 5). The only CAOB source region that has age peaks in the 2500—1500 Ma age range is the NE deserts. Based on these data alone, the possibility of one of the more distal source areas further west or northwest of Nihewan contributing to the ca. 290 Ma age peak cannot, however, be ruled out. Most grain sizes of the analysed zircons are relatively large for long-distance transport but the relatively smaller grain size (typically <80 μm) of the 400—200 Ma zircons compared to the Archean-Palaeoproterozoic and Jurassic-Cretaceous zircons, could also suggest some of these grains to have been transported further. This may include grains originating from central deserts and/or CAOB sources, and the relative distance between Nihewan and these areas on the MDS plot could be explained by a mixture of source areas (Fig. 14a). Indeed, the position of the Nihewan RC age peak at ca. 290 Ma is most similar to the age peaks of the central deserts, CAOB, and the Middle YR, rather than that of the Upper YR (Fig. 5), which represents material eroded from the NE TP (CCO) (Nie et al., 2015). This is supported by the relatively low abundance of 600—400 Ma grains (see below), abundant in the Upper YR. Furthermore, despite its proximity to Nihewan on the MDS map, an origin from the Middle YR reaches itself appears unlikely due to its geographic position to the SW of Nihewan, as well as due to the fact that the Middle YR dominantly erodes Cretaceous sandstone and the NCC immediately after the upper/middle reach YR boundary, rather than deposits material (Nie et al., 2015). Furthermore, the NW/N China and southern Mongolian primary sources include more terranes (CAOB) that formed during ca. 350—250 Ma than the primary source terranes in central China (CCO), which have more abundant formation ages at <250 Ma and > 350 Ma (Table 1).

The presence of the 600–400 Ma ages in the sample, mostly consisting of smaller grains (<80 μm), implies that, similarly to Baode (Shang et al., 2016), some material may have been transported from distal sources from the CCO or Tarim, since those ages are not abundant in the E Mu Us, E NCC, Middle YR, nor the nearest CAOB samples (Fig. 5). However, these ages could also be explained by a proximal western source from the Upper YR, which does have abundant ages in this range (Fig. 5), although as discussed above, this cannot be the only source. These ages are also present in abundance in the W Mu Us and W NCC samples, although both of these areas are also southwest of Nihewan and therefore unlikely source areas (Fig. A1). To conclude, based on the zircon data, eroding local rocks (NCC) provide most material to the Nihewan RC, but the dry areas in the CAOB region, the central deserts, and possibly the upper reaches of the YR, likely also act as sources. Some sediment input from sources further west in the CCO and/or Tarim cannot be excluded from the potential source areas. If southwesterly palaeowinds were present in the early Pliocene, the E and W Mu Us Desert, and the W NCC may also have been sources for the Nihewan RC.

The rutile data provide a means to examine these ambiguities in the zircon age data. In general, the rutile data are consistent with the zircon data, but compared to published rutile data from adjacent areas (Fig. 15), the Nihewan RC Zr-in-rutile temperatures show higher variability, possibly indicating multiple sources for the RC rather than one (proximal) source. The likely sources for the HT and UHT granulitic rutiles in the Nihewan RC are the proximal KB and TNCO on the NCC because HT and UHT rutiles outside these areas in the study region are scarce (Section 6). A proximal source is supported by the large grain sizes of the granulitic Nihewan rutiles and inferences of strong local source input based on the zircon data. Furthermore, rutiles from the KB

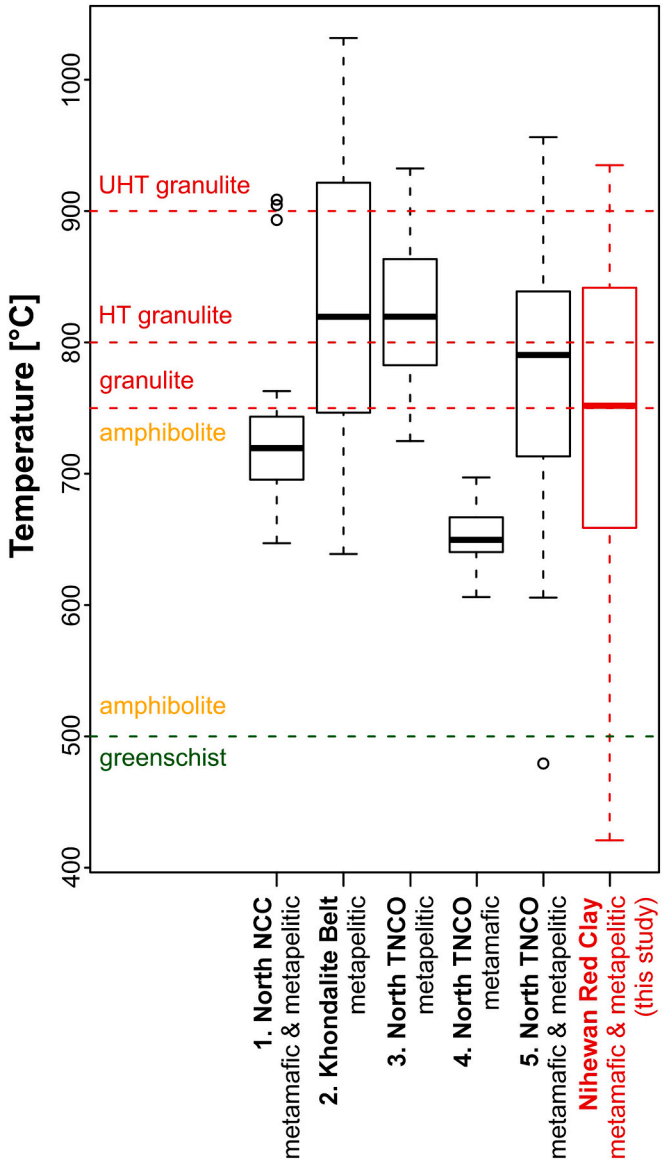

Fig. 15. Comparison of the Zr-in-rutile temperatures (Tomkins et al., 2007) of the Nihewan RC and the previously published rutile data from adjacent areas (see locations in Fig. 11): 1: Liu et al. (2014a), 2: Jiao et al. (2011), 3: Wang et al. (2020), 4: Shi et al. (2012), 5. Zhao et al. (2021).

and the rutile xenocrysts in the carbonatite dykes from the TNCO are metapelitic and detrital rutiles from north NCC and north TNCO are both metamafic (2.8% and 17%, respectively) and metapelitic (97.2% and 83%). Nihewan rutiles are mostly (97%) metapelitic, while those from the Daixian rutile ore in TNCO are all metamafic, also strongly supporting a dominant proximal source from the KB and adjacent areas. However, 16% of the rutiles in Nihewan have metamorphic temperatures lower than 600 °C, which are not present in the data from the adjacent areas (Fig. 15). Their grain sizes are also on the smaller side in the data set (Fig. 13c). Some of these lower Zr-in-rutile temperatures in the Nihewan sample may represent post-peak temperatures from granulitic source regions, but since post-peak temperatures are included in the studies in Fig. 15, most of these greenschist to amphibolite facies Nihewan rutiles are likely transported from other regions. This observation helps remove an ambiguity in the zircon data as the presence of low-temperature metamorphic grains could indicate a source signal from regions further west, such as the NQO in the CCO, or even the Tianshan in the CAOB, where low-temperature metamorphism is prevalent (Section 6). The rutile studies in distant Tianshan show Zr-in-rutile temperatures of ~ < 640 °C, mostly <580 °C, and metamorphic temperatures from NQO are between 420 and 540 °C (Table 1), consistent with the Nihewan low-temperature metamorphic rutiles. Thus, the combined rutile and zircon data demonstrate both near source and far-travelled grain sources the Nihewan RC sample, with the rutile data providing greater constraints on the far-travelled components, and demonstrating the potential of this combined approach.

For future comprehensive provenance analysis of the Nihewan RC by the joint zircon-rutile method, the sedimentary source area rutiles should be analysed for comparison, other trace elements (especially high field strength elements) than presented here (Zr, Cr, Nb) could be analysed, the number of analysed rutile grains should be increased for a better statistical significance, and ideally the analysed grain sizes should be smaller in order to better detect possible transport from distal source areas.

11. Concluding remarks

We present a compilation of the tectonic history of northern China and southern Mongolia that act as the main source areas for the Neogene-Quaternary aeolian dust deposits on the Chinese Loess Plateau (CLP). Future provenance studies on the CLP dust by single-grain methods using geochronologic or metamorphic tracers benefit from this better synthesized understanding of the primary source rocks in which the detrital minerals originally crystallized. This paper discusses four main tectonic divisions of the region: The North China Craton, the Tarim Craton, the Central China Orogen, and parts of the Central Asian Orogenic Belt. The oldest rocks of the study region (Archean to Proterozoic) are in the North China Craton, where the CLP lies, and in the Tarim Craton in West China, but Proterozoic rocks occur also in the Central China Orogen which is located west, south, and east of the CLP, and in parts of the Central Asian Orogenic Belt north and northwest of the CLP. Most of northern China and southern Mongolia formed during the Palaeozoic to Mesozoic closures of the Proto-Tethys (early Palaeozoic), the Palaeo-Tethys (early Mesozoic), and/or the Palaeo-Asian (late Palaeozoic to early Mesozoic) Oceans. The Central China Orogen records early Palaeozoic to Mesozoic Proto- and Palaeo-Tethys closure events, while the Central Asian Orogenic Belt mostly formed during the Palaeo-Asian Ocean closure during late Palaeozoic to early Mesozoic, although parts of the terrane were active also in the early Palaeozoic. The youngest pre-Cenozoic tectonic events in the northern China-southern Mongolia region were concentrated in the eastern parts of the study area, in the North China Craton and Central Asian Orogenic Belt, where they were affected by the late Mesozoic (ca. 170–120 Ma) Yanshan Revolution.

The metamorphic features of the primary source regions are also compiled in this paper, with a focus on metamorphic temperatures. The most striking features of the study region are the proximal North China Craton regions to the CLP that show HT/UHT metamorphic conditions in the Khondalite Belt and Trans-North China Orogen. Outside these Palaeoproterozoic belts, the HT/UHT localities are scarce. In distal regions, most of the Tarim Craton and Central Asian Orogenic Belt have been metamorphosed in greenschist to amphibolite facies, but in Tianshan (Central Asian Orogenic Belt) in the northern margin of the Tarim Craton, a high-pressure/low-temperature zone is identified. This trend of relatively low metamorphic temperatures continues to the North Qilian Orogen in the Central China Orogen, which could potentially be used to identify dust sources from distal western regions.

Dust on the CLP is likely to come from a range of mixed sources, which means that use of single-grain provenance proxies is needed when sourcing the CLP dust. While detrital zircon U-Pb dating has led to major breakthroughs in understanding dust provenance to the CLP, the sole use of detrital zircons still leaves ambiguities in provenance inferences, caused partly by the somewhat overlapping age distributions in the potential source areas west, north, and south of the CLP, the scarcity of

high-*N* detrital zircon age data for the CLP dust, and the bias inherent in the technique resulting from exclusion of metamorphic or zircon poor potential source rocks. Our compiled published dataset and re-analysis shows the dominance of 500—400 Ma ages over the 300—200 Ma ages has traditionally been attributed to western source area prevalence (Tarim and Central China Orogen), while the abundance of the 300—200 Ma ages is traditionally assigned to a source signal from the north/northwest of the CLP (Central Asian Orogenic Belt). However, the proximity of the western source areas is inconclusive from zircon U-Pb data alone, since secondary sources from both Central China Orogen and Tarim show similar age distributions. Furthermore, the 300—200 Ma zircon ages are present in almost all source areas to some degree, and should not be directly assigned only to the northern/northwestern Central Asian Orogenic Belt sources. Therefore, other proxies than the age of detrital zircons, which is also biased towards intermediate and felsic igneous rocks, should be used.

Our review and data compilation show that the metamorphic features of the distal (Tarim) and more proximal (Central China Orogen) western source regions differ, and that a northern/northwestern source signal could possibly be pinpointed from metamorphic temperature data by using the UHT signal from the Khondalite Belt. For these reasons, we encourage the use of multi-proxy single-grain provenance studies through combined detrital zircon U-Pb and detrital rutile geochemical analysis for sourcing the CLP sediments. The trace element geochemistry of detrital rutiles allow metamorphic features (temperature, protolith) of the primary source rocks to be used for quantitative provenance analysis. To illustrate the potential of this joint approach, we analysed the provenance of the ca. 4 Ma Nihewan Red Clay in northern CLP. The Nihewan zircon U-Pb and rutile trace element data show consistent results, which verifies the use of the novel rutile method. The data imply a main source from the eroding local bedrock (North China Craton), with additional contributions from the dry areas in the Central Asian Orogenic Belt region, the central deserts, and the Yellow River. Furthermore, if southwesterly winds were present during the Nihewan Red Clay deposition, Mu Us sediments could have been another major source. The joint zircon and rutile data also suggest that material from further west (Central China Orogen and Tarim) may have been transported to Nihewan, which is particularly evident in the rutile data. However, our aim here is more to reveal the potential of this approach and provide background data that facilitates it. More detailed analyses and rutile data from the potential secondary source areas are needed to make further conclusions, and we hope our new geologic background and data compilation provide a means to significantly refine future source interpretation to the CLP. Our review and data also demonstrate how future provenance studies on the CLP sediments would benefit from multi-proxy single-grain approaches. The combined use of detrital zircons and rutiles is especially practical because of their similar physical properties, enabling their simultaneous preparation, and because of the different source rock information that they provide. Future methodological developments enabling the analysis of large numbers of finer grain sizes would also aid in achieving better understanding of the Red Clay provenance and its spatiotemporal variations.

Declaration of Competing Interest

The authors declare that they have no known competing financial interests or personal relationships that could have appeared to influence the work reported in this paper.

Acknowledgements

We thank Editor Asfawossen Asrat and three anonymous reviewers for constructive comments, which significantly improved this paper. KB gratefully acknowledges Roel van Elsas for helping with sample preparation, and Nordenskiöld-foundation and GeoDoc for travel grants. This research was funded by the Academy of Finland grant (316799) to AK. TS gratefully acknowledges the support of the Swedish Research Council (2017-03888) and a STINT-NSFC mobility grant (CH2020-8688). ZZQ was supported by the Ministry of Science and Technology grant (2014FY110300).

Appendix A. Supplementary data

Supplementary data to this article can be found online at https://doi.org/10.1016/j.earscirev.2021.103909.

References

Abell, J.T., Winckler, G., Anderson, R.F., Herbert, T.D., 2021. Poleward and weakened westerlies during Pliocene warmth. Nature 589 (7840), 70–75.
Adebiyi, A.A., Kok, J.F., 2020. Climate models miss most of the coarse dust in the atmosphere. Sci. Adv. 6 (15), eaaz9507.
Aitchison, J.C., Ali, J.R., Davis, A.M., 2007. When and where did India and Asia collide? J. Geophys. Res. 112 (B5).
Alonso-Zarza, A.M., Zhao, Z., Song, C.H., Li, J.J., Zhang, J., Martín-Pérez, A., Martín-García, R., Wang, X.X., Zhang, Y., Zhang, M.H., 2009. Mudflat/distal fan and shallow lake sedimentation (upper Vallesian–Turolian) in the Tianshui Basin, Central China: evidence against the late Miocene eolian loess. Sediment. Geol. 222 (1), 42–51.
An, Z., Wang, S., Wu, X., Chen, M., Sun, D., Liu, X., Wang, F., Li, L., Sun, Y., Zhou, W., Zhou, J., Liu, X., Lu, H., Zhang, Y., Dong, G., Qiang, X., 1999. Eolian evidence from the Chinese Loess Plateau: the onset of the Late Cenozoic Great Glaciation in the Northern Hemisphere and Qinghai-Xizang Plateau uplift forcing. Sci. China Ser. D: Earth Sciences 42 (3), 258.
An, Z., Sun, D., Chen, M., Sun, Y., Li, L., Chen, B., 2000. Red clay sequences in Chinese Loess Plateau and recorded paleoclimate events of the late tertiary. Quat. Sci. 20 (5), 435–446.
An, Z., Kutzbach, J.E., Prell, W.L., Porter, S.C., 2001. Evolution of Asian monsoons and phased uplift of the Himalaya–Tibetan plateau since Late Miocene times. Nature 411, 62.
An, Z., Sun, Y., Zhou, W., Liu, W., Qiang, X., Wang, X., Xian, F., Cheng, P., Burr, G.S., 2014. Chinese Loess and the East Asian Monsoon. In: An, Z. (Ed.), Late Cenozoic Climate Change in Asia. Dev. Paleoenviron. Res., 16 Springer, Dordrecht, pp. 23–143.
Andersen, T., Kristoffersen, M., Elburg, M.A., 2016. How far can we trust provenance and crustal evolution information from detrital zircons? A South African case study. Gondwana Res. 34, 129–148.
Anwar, T., Kravchinsky, V.A., Zhang, R., 2015. Magneto- and cyclostratigraphy in the red clay sequence: new age model and paleoclimatic implication for the eastern Chinese Loess Plateau. J. Geophys. Res. Solid Earth 120 (10), 6758–6770.
Ao, H., Roberts, A.P., Dekkers, M.J., Liu, X., Rohling, E.J., Shi, Z., An, Z., Zhao, X., 2016. Late Miocene–Pliocene Asian monsoon intensification linked to Antarctic ice-sheet growth. Earth Planet. Sci. Lett. 444, 75–87.
Aoki, T., Motoyoshi, H., Kodama, Y., Yasunari, T.J., Sugiura, K., Kobayashi, H., 2006. Atmospheric aerosol deposition on snow surfaces and its effect on Albedo. SOLA 2, 13–16.
Badarch, G., Dickson Cunningham, W., Windley, B.F., 2002. A new terrane subdivision for Mongolia: implications for the Phanerozoic crustal growth of Central Asia. J. Asian Earth Sci. 21 (1), 87–110.
Bader, T., Franz, L., Ratschbacher, L., de Capitani, C., Webb, A.A.G., Yang, Z., Pfänder, J. A., Hofmann, M., Linnemann, U., 2013. The Heart of China revisited: II Early Paleozoic (ultra)high-pressure and (ultra)high-temperature metamorphic Qinling orogenic collage. Tectonics 32 (4), 922–947.
Barbour, G.B., 1924. Preliminary observations in the Kalgan area. Bull. Geol. Soc. China 3 (2), 153–168.
Barbour, G.B., 1925. The Deposits of the Sang Kan Ho Valley. Bull. Geol. Soc. China 4 (1), 53–55.
Barbour, G.B., Licent, E., Teilhard de Chardin, P., 1926. Geological study of the deposits of the Sangkanho Basin. Bull. Geol. Soc. China 5 (3–4), 263–278.
Belousova, E.A., Griffin, W.L., O'Reilly, S.Y., 2006. Zircon crystal morphology, trace element signatures and Hf isotope composition as a tool for petrogenetic modeling: examples from Eastern Australian granitoids. J. Petrol. 47, 329–353.
Bird, A., Stevens, T., Rittner, M., Vermeesch, P., Carter, A., Andò, S., Garzanti, E., Lu, H., Nie, J., Zeng, L., Zhang, H., Xu, Z., 2015. Quaternary dust source variation across the Chinese Loess Plateau. Palaeogeogr. Palaeoclimatol. Palaeoecol. 435, 254–264.
Bird, A., Millar, I., Rodenburg, T., Stevens, T., Rittner, M., Vermeesch, P., Lu, H., 2020. A constant Chinese Loess Plateau dust source since the late Miocene. Quat. Sci. Rev. 227, 106042.
Börker, J., Hartmann, J., Amann, T., Romero-Mujalli, G., 2018. Terrestrial Sediments of the Earth: Development of a Global Unconsolidated Sediments Map Database (GUM). Geochem. Geophys. Geosyst. 19 (4), 997–1024.
Cai, B.-Q., Zheng, S.-H., Liddicoat, J.C., Li, Q., 2013. Review of the Litho-, Bio-, and Chronostratigraphy in the Nihewan Basin, Hebei, China. In: Wang, X., Flynn, L.J., Fortelius, M. (Eds.), Fossil Mammals of Asia. Columbia University Press, New York, pp. 218–242.
Cai, J., Liu, F., Liu, P., Wang, F., Meng, E., Wang, W., Yang, H., Ji, L., Liu, L., 2017. Discovery of granulite-facies metamorphic rocks in the Ji'an area, northeastern Jiao–Liao–Ji Belt, North China Craton: metamorphic P–T evolution and geological implications. Precambrian Res. 303, 626–640.

Cai, J., Liu, F., Liu, C., 2020. A unique Paleoproterozoic HP–UHT metamorphic event recorded by the Bengbu mafic granulites in the southwestern Jiao–Liao–Ji Belt, North China Craton. Gondwana Res. 80, 244–274.
Chapman, J.B., Scoggin, S.H., Kapp, P., Carrapa, B., Ducea, M.N., Worthington, J., Oimahmadov, I., Gadoev, M., 2018. Mesozoic to Cenozoic magmatic history of the Pamir. Earth Planet. Sci. Lett. 482, 181–192.
Chen, X., Zheng, Y., Xu, R., Gu, P., Yu, J., Bai, J., Cai, P., Jiang, X., 2020. Subduction channel fluid-rock interaction: Indications from rutile-quartz veins within eclogite from the Yuka terrane, North Qaidam Orogen. Geosci. Front. 11 (2), 635–650.
Chen, Z., Li, G., 2013. Evolving sources of eolian detritus on the Chinese Loess Plateau since early Miocene: tectonic and climatic controls. Earth Planet. Sci. Lett. 371-372, 220–225.
Chen, Z.-Y., Zhang, L.-F., Du, J.-X., Lü, Z., 2013. Zr-in-rutile thermometry in eclogite and vein from southwestern Tianshan, China. J. Asian Earth Sci. 63, 70–80.
Cheng, F., Jolivet, M., Hallot, E., Zhang, D., Zhang, C., Guo, Z., 2017. Tectono-magmatic rejuvenation of the Qaidam craton, northern Tibet. Gondwana Res. 49, 248–263.
Cheng, F., Jolivet, M., Guo, Z., Wang, L., Zhang, C., Li, X., 2021. Cenozoic evolution of the Qaidam basin and implications for the growth of the northern Tibetan plateau: a review. Earth Sci. Rev. 220, 103730.
Chew, D., O'Sullivan, G., Caracciolo, L., Mark, C., Tyrrell, S., 2020. Sourcing the sand: accessory mineral fertility, analytical and other biases in detrital U-Pb provenance analysis. Earth Sci. Rev. 202, 103093.
Coale, K.H., Johnson, K.S., Fitzwater, S.E., Gordon, R.M., Tanner, S., Chavez, F.P., Ferioli, L., Sakamoto, C., Rogers, P., Millero, F., Steinberg, P., Nightingale, P., Cooper, D., Cochlan, W.P., Landry, M.R., Constantinou, J., Rollwagen, G., Trasvina, A., Kudela, R., 1996. A massive phytoplankton bloom induced by an ecosystem-scale iron fertilization experiment in the equatorial Pacific Ocean. Nature 383 (6600), 495–501.
Deer, W.A., Howie, R.A., Zussman, J., 2013. "Rutile TiO2", An Introduction to the Rock-Forming Minerals. In: Mineralogical Society of Great Britain and Ireland, pp. 393–395.
Demoux, A., Kröner, A., Liu, D., Badarch, G., 2009. Precambrian crystalline basement in southern Mongolia as revealed by SHRIMP zircon dating. Int. J. Earth Sci. 98 (6), 1365–1380.
Ding, L., Kapp, P., Wan, X., 2005. Paleocene–Eocene record of ophiolite obduction and initial India-Asia collision, south central Tibet. Tectonics 24 (3).
Ding, Z.L., Sun, J.M., Liu, T.S., Zhu, R.X., Yang, S.L., Guo, B., 1998a. Wind-blown origin of the Pliocene red clay formation in the central Loess Plateau, China. Earth Planet. Sci. Lett. 161 (1), 135–143.
Ding, Z.L., Sun, J.M., Yang, S.L., Liu, T.S., 1998b. Preliminary magnetostratigraphy of a thick eolian red clay-loess sequence at Lingtai, the Chinese Loess Plateau. Geophys. Res. Lett. 25 (8), 1225–1228.
Ding, Z.L., Xiong, S.F., Sun, J.M., Yang, S.L., Gu, Z.Y., Liu, T.S., 1999. Pedostratigraphy and paleomagnetism of a ~7.0 Ma eolian loess–red clay sequence at Lingtai, Loess Plateau, north-central China and the implications for paleomonsoon evolution. Palaeogeogr. Palaeoclimatol. Palaeoecol. 152 (1), 49–66.
Ding, Z.L., Rutter, N.W., Sun, J.M., Yang, S.L., Liu, T.S., 2000. Re-arrangement of atmospheric circulation at about 2.6 Ma over northern China: evidence from grain size records of loess-palaeosol and red clay sequences. Quat. Sci. Rev. 19 (6), 547–558.
Diwu, C., Sun, Y., Zhang, H., Wang, Q., Guo, A., Fan, L., 2012. Episodic tectonothermal events of the western North China Craton and North Qinling Orogenic Belt in central China: constraints from detrital zircon U–Pb ages. J. Asian Earth Sci. 47, 107–122.
van der Does, M., Korte, L.F., Munday, C.I., Brummer, G.J.A., Stuut, J.B.W., 2016. Particle size traces modern Saharan dust transport and deposition across the equatorial North Atlantic. Atmos. Chem. Phys. 16 (21), 13697–13710.
van der Does, M., Knippertz, P., Zschenderlein, P., Giles Harrison, R., Stuut, J.-B.W., 2018. The mysterious long-range transport of giant mineral dust particles. Sci. Adv. 4 (12), eaau2768.
Dong, J., Wei, C.-J., Clarke, G.L., Zhang, J.-X., 2018a. Metamorphic evolution during deep subduction and exhumation of continental crust: insights from Felsic Granulites in South Altyn Tagh, West China. J. Petrol. 59 (10), 1965–1990.
Dong, S., Zhang, Y., Zhang, F., Cui, J., Chen, X., Zhang, S., Miao, L., Li, J., Shi, W., Li, Z., Huang, S., Li, H., 2015. Late Jurassic–Early Cretaceous continental convergence and intracontinental orogenesis in East Asia: a synthesis of the Yanshan Revolution. J. Asian Earth Sci. 114, 750–770.
Dong, Y., Santosh, M., 2016. Tectonic architecture and multiple orogeny of the Qinling Orogenic Belt, Central China. Gondwana Res. 29 (1), 1–40.
Dong, Y., Zhang, G., Neubauer, F., Liu, X., Genser, J., Hauzenberger, C., 2011. Tectonic evolution of the Qinling orogen, China: review and synthesis. J. Asian Earth Sci. 41 (3), 213–237.
Dong, Y., He, D., Sun, S., Liu, X., Zhou, X., Zhang, F., Yang, Z., Cheng, B., Zhao, G., Li, J., 2018b. Subduction and accretionary tectonics of the East Kunlun orogen, western segment of the Central China Orogenic System. Earth Sci. Rev. 186, 231–261.
Dowsett, H.J., Robinson, M.M., Stoll, D.K., Foley, K.M., Johnson, A.L.A., Williams, M., Riesselman, C.R., 2013. The PRISM (Pliocene palaeoclimate) reconstruction: time for a paradigm shift. Philos. Trans. R. Soc. 371 (2001), 20120524.
Du, H.-J., Wang, A.-D., Zhao, Q.-Q., Cai, B.-Q., 1988. Daodi formation — A new Pliocene stratigraphic unit in Nihewan district. Earth Sci. - J. China Univ. Geosci. 13 (5), 561–568 (in Chinese).
Dupont-Nivet, G., Lippert, P.C., Van Hinsbergen, D.J.J., Meijers, M.J.M., Kapp, P., 2010. Palaeolatitude and age of the Indo–Asia collision: palaeomagnetic constraints. Geophys. J. Int. 182 (3), 1189–1198.
Eizenhöfer, P.R., Zhao, G., 2018. Solonker Suture in East Asia and its bearing on the final closure of the eastern segment of the Palaeo-Asian Ocean. Earth Sci. Rev. 186, 153–172.
Eizenhöfer, P.R., Zhao, G., Zhang, J., Sun, M., 2014. Final closure of the Paleo-Asian Ocean along the Solonker Suture Zone: constraints from geochronological and geochemical data of Permian volcanic and sedimentary rocks. Tectonics 33 (4), 441–463.
Enkelmann, E., Weislogel, A., Ratschbacher, L., Eide, E., Renno, A., Wooden, J.J.T., 2007. How was the Triassic Songpan-Ganzi basin filled? A provenance study. Tectonics 26 (4).
von Eynatten, H., Tolosana-Delgado, R., Triebold, S., Zack, T., 2005. Interactions between grain size and composition of sediments: two examples. In: Proceedings CoDaWork05-2nd compositional data analysis workshop, Girona. 19-21 Oct 2005.
Fang, X., Zhang, W., Meng, Q., Gao, J., Wang, X., King, J., Song, C., Dai, S., Miao, Y., 2007. High-resolution magnetostratigraphy of the Neogene Huaitoutala section in the eastern Qaidam Basin on the NE Tibetan Plateau, Qinghai Province, China and its implication on tectonic uplift of the NE Tibetan Plateau. Earth Planet. Sci. Lett. 258 (1), 293–306.
Fang, X., Dupont-Nivet, G., Wang, C., Song, C., Meng, Q., Zhang, W., Nie, J., Zhang, T., Mao, Z., Chen, Y., 2020. Revised chronology of central Tibet uplift (Lunpola Basin). Sci. Adv. 6 (50), eaba7298.
Farnsworth, A., Lunt, D.J., Robinson, S.A., Valdes, P.J., Roberts, W.H.G., Clift, P.D., Markwick, P., Su, T., Wrobel, N., Bragg, F., Kelland, S.-J., Pancost, R.D., 2019. Past East Asian monsoon evolution controlled by paleogeography, not CO2. Sci. Adv. 5 (10), eaax1697.
Fenn, K., Stevens, T., Bird, A., Limonta, M., Rittner, M., Vermeesch, P., Andò, S., Garzanti, E., Lu, H., Zhang, H., Lin, Z., 2018. Insights into the provenance of the Chinese Loess Plateau from joint zircon U-Pb and garnet geochemical analysis of last glacial loess. Quat. Res. 89 (3), 645–659.
Ferry, J.M., Watson, E.B., 2007. New thermodynamic models and revised calibrations for the Ti-in-zircon and Zr-in-rutile thermometers. Contrib. Mineral. Petrol. 154 (4), 429–437.
Foley, S.F., Barth, M.G., Jenner, G.A., 2000. Rutile/melt partition coefficients for trace elements and an assessment of the influence of rutile on the trace element characteristics of subduction zone magmas. Geochim. Cosmochim. Acta 64 (5), 933–938.
Force, E.R., 1980. The provenance of rutile. J. Sediment. Res. 50 (2), 485–488.
Gaetani, M., Gosso, G., Pognante, U., 1990. A geological transect from Kun Lun to Karakorum (Sinkiang, China): the western termination of the Tibetan Plateau. Preliminary note. Terra Nova 2 (1), 23–30.
Gao, J., Klemd, R., Zhang, L., Wang, Z., Xiao, X., 1999. P–T path of high-pressure/low-temperature rocks and tectonic implications in the western Tianshan Mountains, NW China. J. Metamorph. Geol. 17 (6), 621–636.
Garzanti, E., 2017. The maturity Myth in sedimentology and provenance analysis. J. Sediment. Res. 87 (4), 353–365.
Ge, J., Dai, Y., Zhang, Z., Zhao, D., Li, Q., Zhang, Y., Yi, L., Wu, H., Oldfield, F., Guo, Z., 2013b. Major changes in East Asian climate in the mid-Pliocene: triggered by the uplift of the Tibetan Plateau or global cooling? J. Asian Earth Sci. 69, 48–59.
Ge, R., Zhu, W., Wu, H., He, J., Zheng, B., 2013a. Zircon U–Pb ages and Lu–Hf isotopes of Paleoproterozoic metasedimentary rocks in the Korla Complex, NW China: implications for metamorphic zircon formation and geological evolution of the Tarim Craton. Precambrian Res. 231, 1–18.
Ge, R., Zhu, W., Wilde, S.A., He, J., Cui, X., Wang, X., Bihai, Z., 2014a. Neoproterozoic to Paleozoic long-lived accretionary orogeny in the northern Tarim Craton. Tectonics 33 (3), 302–329.
Ge, R., Zhu, W., Wilde, S.A., Wu, H., He, J., Zheng, B., 2014b. Archean magmatism and crustal evolution in the northern Tarim Craton: Insights from zircon U–Pb–Hf–O isotopes and geochemistry of ~2.7Ga orthogneiss and amphibolite in the Korla Complex. Precambrian Res. 252, 145–165.
Ge, R., Zhu, W., Wilde, S.A., 2016. Mid-Neoproterozoic (ca. 830–800 Ma) metamorphic P-T paths link Tarim to the circum-Rodinia subduction-accretion system. Tectonics 35 (6), 1465–1488.
Geng, Y.-S., Shen, Q.-H., Song, H.-X., 2018. Metamorphic petrology and geology in China: a review. China Geol. 1 (1), 137–157.
Gong, H., Xie, W., Zhang, R., Zhang, Y., 2017. U-Pb ages of detrital zircon and provenances of Red Clay in the Chinese Loess Plateau. J. Asian Earth Sci. 138, 495–501.
Guo, J., Peng, P., Chen, Y., Jiao, S., Windley, B.F., 2012. UHT sapphirine granulite metamorphism at 1.93–1.92Ga caused by gabbronorite intrusions: implications for tectonic evolution of the northern margin of the North China Craton. Precambrian Res. 222-223, 124–142.
Guo, J.H., O'Brien, P.J., Zhai, M., 2002a. High-pressure granulites in the Sanggan area, North China craton: metamorphic evolution, P–T paths and geotectonic significance. J. Metamorph. Geol. 20 (8), 741–756.
Guo, Z.T., Peng, S.Z., Hao, Q.Z., Biscaye, P.E., Liu, T.S., 2001. Origin of the Miocene–Pliocene Red-Earth formation at Xifeng in Northern China and implications for paleoenvironments. Palaeogeogr. Palaeoclimatol. Palaeoecol. 170 (1), 11–26.
Guo, Z.T., Ruddiman, W.F., Hao, Q.Z., Wu, H.B., Qiao, Y.S., Zhu, R.X., Peng, S.Z., Wei, J. J., Yuan, B.Y., Liu, T.S., 2002b. Onset of Asian desertification by 22 Myr ago inferred from loess deposits in China. Nature 416, 159.
Hacker, B.R., Wallis, S.R., Ratschbacher, L., Grove, M., Gehrels, G., 2006. High-temperature geochronology constraints on the tectonic history and architecture of the ultrahigh-pressure Dabie-Sulu Orogen. Tectonics 25 (5).
Han, J., Chen, H., Fyfe, W.S., Guo, Z., Wang, D., Liu, T.S., 2007. Spatial and temporal patterns of grain size and chemical weathering of the Chinese Red Clay Formation and implications for East Asian monsoon evolution. Geochim. Cosmochim. Acta 71 (16), 3990–4004.

Han, Y., Zhao, G., 2018. Final amalgamation of the Tianshan and Junggar orogenic collage in the southwestern Central Asian Orogenic Belt: constraints on the closure of the Paleo-Asian Ocean. Earth Sci. Rev. 186, 129–152.
Haug, G.H., Sigman, D.M., Tiedemann, R., Pedersen, T.F., Sarnthein, M., 1999. Onset of permanent stratification in the subarctic Pacific Ocean. Nature 401 (6755), 779–782.
Hou, S., Yang, S., Sun, J., Ding, Z., 2003. Oxygen isotope compositions of quartz grains (4–16 μm) from Chinese eolian deposits and their implications for provenance. Sci. China Ser. D Earth Sci. 46 (10), 1003.
Huang, B.-Y., Guo, S.-Y., 1981. Discussion on stratigraphic division, geological period and palaeography of the Nihewan according to the mollusca. Bull. Tianjin Inst. Geol. Mineral Resour. Res. 4, 17–30 (in Chinese with English abstract).
Huhma, H., Mänttäri, I., Peltonen, P., Kontinen, A., Halkoaho, T., Hanski, E., Hokkanen, T., Hölttä, P., Juopperi, H., Konnunaho, J., Layahe, Y., Luukkonen, E., Pietikäinen, K., Pulkkinen, A., Sorjonen-Ward, P., Vaasjoki, M., Whitehouse, M., 2012. The age of the Archaean greenstone belts in Finland. Geol. Surv. Finland Spec. Pap. 54, 74–175.
Jiang, X.-D., Li, Z.-X., 2014. Seismic reflection data support episodic and simultaneous growth of the Tibetan Plateau since 25 Myr. Nat. Commun. 5 (1), 5453.
Jiang, Y., Sun, M., Zhao, G., Yuan, C., Xiao, W., Xia, X., Long, X., Wu, F., 2010. The ~390 Ma high-T metamorphic event in the Chinese Altai: A consequence of ridge-subduction? Am. J. Sci. 310, 1421–1452.
Jiang, Y.D., Štípská, P., Sun, M., Schulmann, K., Zhang, J., Wu, Q.H., Long, X.P., Yuan, C., Racek, M., Zhao, G.C., Xiao, W.J., 2015. Juxtaposition of Barrovian and migmatite domains in the Chinese Altai: a result of crustal thickening followed by doming of partially molten lower crust. J. Metamorph. Geol. 33 (1), 45–70.
Jiao, S., Guo, J., Mao, Q., Zhao, R., 2011. Application of Zr-in-rutile thermometry: a case study from ultrahigh-temperature granulites of the Khondalite belt, North China Craton. Contrib. Mineral. Petrol. 162 (2), 379–393.
Jochum, K.P., Willbold, M., Raczek, I., Stoll, B., Herwig, K., 2005. Chemical Characterisation of the USGS Reference Glasses GSA-1G, GSC-1G, GSD-1G, GSE-1G, BCR-2G, BHVO-2G and BIR-1G Using EPMA, ID-TIMS, ID-ICP-MS and LA-ICP-MS. Geostand. Geoanal. Res. 29 (3), 285–302.
Khain, E.V., Bibikova, E.V., Kröner, A., Zhuravlev, D.Z., Sklyarov, E.V., Fedotova, A.A., Kravchenko-Berezhnoy, I.R., 2002. The most ancient ophiolite of the Central Asian fold belt: U–Pb and Pb–Pb zircon ages for the Dunzhugur Complex, Eastern Sayan, Siberia, and geodynamic implications. Earth Planet. Sci. Lett. 199 (3), 311–325.
Kohfeld, K.E., Harrison, S.P., 2001. DIRTMAP: the geological record of dust. Earth Sci. Rev. 54 (1), 81–114.
Kooijman, E., Smit, M.A., Mezger, K., Berndt, J., 2012. Trace element systematics in granulite facies rutile: implications for Zr geothermometry and provenance studies. J. Metamorph. Geol. 30 (4), 397–412.
Kröner, A., Lehmann, J., Schulmann, K., Demoux, A., Lexa, O., Tomurhuu, D., Štípská, P., Liu, D., Wingat, M.T.D., 2010. Lithostratigraphic and geochronological constraints on the evolution of the central Asian orogenic belt in SW Mongolia: Early paleozoic rifting followed by late paleozoic accretion. Am. J. Sci. 310 (7), 523–574.
Lei, H., Xu, H., Liu, P., 2020. Decoupling between Ti-in-zircon and Zr-in-rutile thermometry during ultrahigh temperature metamorphism of the Dabie Orogen, China. Geol. J. 55 (9), 6442–6449.
Li, J., Fang, X., Song, C., Pan, B., Ma, Y., Yan, M., 2014. Late Miocene–Quaternary rapid stepwise uplift of the NE Tibetan Plateau and its effects on climatic and environmental changes. Quat. Res. 81 (3), 400–423.
Li, X.-H., Li, W.-X., Wang, X.-C., Li, Q.-L., Liu, Y., Tang, G.-Q., Gao, Y.-Y., Wu, F.-Y., 2010. SIMS U–Pb zircon geochronology of porphyry Cu–Au–(Mo) deposits in the Yangtze River Metallogenic Belt, eastern China: magmatic response to early Cretaceous lithospheric extension. Lithos 119 (3), 427–438.
Li, Y., Wang, C., Dai, J., Xu, G., Hou, Y., Li, X., 2015. Propagation of the deformation and growth of the Tibetan–Himalayan orogen: a review. Earth Sci. Rev. 143, 36–61.
Licht, A., van Cappelle, M., Abels, H.A., Ladant, J.B., Trabucho-Alexandre, J., France-Lanord, C., Donnadieu, Y., Vandenberghe, J., Rigaudier, T., Lécuyer, C., Terry Jr., D., Adriaens, R., Boura, A., Guo, Z., Soe, A.N., Quade, J., Dupont-Nivet, G., Jaeger, J.J., 2014. Asian monsoons in a late Eocene greenhouse world. Nature 513 (7519), 501–506.
Licht, A., Pullen, A., Kapp, P., Abell, J., Giesler, N., 2016. Eolian cannibalism: Reworked loess and fluvial sediment as the main sources of the Chinese Loess Plateau. Geol. Soc. Am. Bull. 128 (5–6), 944–956.
Lin, A., Yang, Z., Sun, Z., Yang, T., 2001. How and when did the Yellow River develop its square bend? Geology 29 (10), 951–954.
Liu, C., Zhao, G., Liu, F., 2014a. Detrital zircon U–Pb, Hf isotopes, detrital rutile and whole-rock geochemistry of the Huade Group on the northern margin of the North China Craton: implications on the breakup of the Columbia supercontinent. Precambrian Res. 254, 290–305.
Liu, L., Yang, J., Chen, D., Wang, C., Zhang, C., Yang, W., Cao, Y., 2010. Progress and controversy in the study of HP-UHP metamorphic terranes in the West and Middle Central China orogen. J. Earth Sci. 21 (5), 581–597.
Liu, L., Wang, C., Cao, Y.-T., Chen, D.-L., Kang, L., Yang, W.-Q., Zhu, X.-H., 2012a. Geochronology of multi-stage metamorphic events: constraints on episodic zircon growth from the UHP eclogite in the South Altyn, NW China. Lithos 136-139, 10–26.
Liu, L., Xiao, Y., Wörner, G., Kronz, A., Simon, K., Hou, Z., 2014b. Detrital rutile geochemistry and thermometry from the Dabie orogen: implications for source–sediment links in a UHPM terrane. J. Asian Earth Sci. 89, 123–140.
Liu, P., Yue, F., Liu, J., Qin, H., Li, S., Zhao, X., Xu, J., Yuan, B., Deng, C., Zhu, R., 2018. Magnetostratigraphic dating of the Shixia red sediments and implications for formation of Nihewan paleo-lake, North China. Quat. Sci. Rev. 193, 118–128.
Liu, Q., Zhao, G., Sun, M., Eizenhöfer, P.R., Han, Y., Hou, W., Zhang, X., Wang, B., Liu, D., Xu, B., 2015a. Ages and tectonic implications of Neoproterozoic ortho- and paragneisses in the Beishan Orogenic Belt, China. Precambrian Res. 266, 551–578.
Liu, Q., Zhao, G., Han, Y., Eizenhöfer, P.R., Zhu, Y., Hou, W., Zhang, X., 2017. Timing of the final closure of the Paleo-Asian Ocean in the Alxa Terrane: constraints from geochronology and geochemistry of Late Carboniferous to Permian gabbros and diorites. Lithos 274-275, 19–30.
Liu, S., Zhao, G., Wilde, S.A., Shu, G., Sun, M., Li, Q., Tian, W., Zhang, J., 2006. Th–U–Pb monazite geochronology of the Lüliang and Wutai Complexes: constraints on the tectonothermal evolution of the Trans-North China Orogen. Precambrian Res. 148 (3), 205–224.
Liu, S., Tsunogae, T., Li, W., Shimizu, H., Santosh, M., Wan, Y., Li, J., 2012b. Paleoproterozoic granulites from Heling'er: Implications for regional ultrahigh-temperature metamorphism in the North China Craton. Lithos 148, 54–70.
Liu, S., Li, J., Stockli, D.F., Song, C., Guo, B., Stockli, L.D., Ma, Z., Li, X., Peng, T., 2019. Reappraisal of Miocene eolian deposition in Tianshui Basin, China, based on an investigation of stratigraphy and provenance. Geol. Soc. Am. Bull. 131 (7–8), 1312–1332.
Liu, W., Liu, Z., An, Z., Sun, J., Chang, H., Wang, N., Dong, J., Wang, H., 2014c. Late Miocene episodic lakes in the arid Tarim Basin, western China. Proc. Natl. Acad. Sci. 111 (46), 16292–16296.
Liu, X., Sun, H., Miao, Y., Dong, B., Yin, Z.-Y., 2015b. Impacts of uplift of northern Tibetan Plateau and formation of Asian inland deserts on regional climate and environment. Quat. Sci. Rev. 116, 1–14.
Liu, X., Wang, Q., Zhao, L., Peng, Y., Ma, Y., Zhou, Z., 2020b. Metallogeny of the large-scale Carboniferous karstic bauxite in the Sanmenxia area, southern part of the North China Craton, China. Chem. Geol. 556, 119851.
Liu, Y., Genser, J., Neubauer, F., Jin, W., Ge, X., Handler, R., Takasu, A., 2005. 40Ar/39Ar mineral ages from basement rocks in the Eastern Kunlun Mountains, NW China, and their tectonic implications. Tectonophysics 398 (3), 199–224.
Liu, Z., Bartoli, O., Tong, L., Xu, Y.G., Huang, X., 2020a. Permian ultrahigh–temperature reworking in the southern Chinese Altai: evidence from petrology, P–T estimates, zircon and monazite U–Th–Pb geochronology. Gondwana Res. 78, 20–40.
Lu, H., Wang, X., Li, L., 2010. Aeolian sediment evidence that global cooling has driven late Cenozoic stepwise aridification in central Asia. Geol. Soc. London Spec. Publ. 342 (1), 29–44.
Lu, H., Wang, X., Wang, X., Chang, X., Zhang, H., Xu, Z., Zhang, W., Wei, H., Zhang, X., Yi, S., Zhang, W., Feng, H., Wang, Y., Wang, Y., Han, Z., 2019. Formation and evolution of Gobi Desert in central and eastern Asia. Earth Sci. Rev. 194, 251–263.
Lu, S., Li, H., Zhang, C., Niu, G., 2008. Geological and geochronological evidence for the Precambrian evolution of the Tarim Craton and surrounding continental fragments. Precambrian Res. 160 (1), 94–107.
Lü, Z., Zhang, L., Du, J., Yang, X., Tian, Z., Xia, B., 2012. Petrology of HP metamorphic veins in coesite-bearing eclogite from western Tianshan, China: fluid processes and elemental mobility during exhumation in a cold subduction zone. Lithos 136-139, 168–186.
Lunt, D.J., Haywood, A.M., Schmidt, G.A., Salzmann, U., Valdes, P.J., Dowsett, H.J., 2010. Earth system sensitivity inferred from Pliocene modelling and data. Nat. Geosci. 3 (1), 60–64.
Ma, L., Sun, Y., Tada, R., Yan, Y., Chen, H., Lin, M., Nagashima, K., 2015. Provenance fluctuations of aeolian deposits on the Chinese Loess Plateau since the Miocene. Aeolian Res. 18, 1–9.
Maher, B.A., Prospero, J.M., Mackie, D., Gaiero, D., Hesse, P.P., Balkanski, Y., 2010. Global connections between aeolian dust, climate and ocean biogeochemistry at the present day and at the last glacial maximum. Earth Sci. Rev. 99 (1), 61–97.
Manabe, S., Broccoli, A.J., 1990. Mountains and arid climates of middle latitudes. Science 247 (4939), 192–195.
Mao, L.-J., He, Z.-Y., Zhang, Z.-M., Klemd, R., Xiang, H., Tian, Z.-L., Zong, K.-Q., 2015. Origin and geodynamic significance of the early Mesozoic Weiya LP and HT granulites from the Chinese Eastern Tianshan. Lithos 239, 142–156.
Martin, J.H., 1990. Glacial-interglacial CO2 change: the iron hypothesis. Paleoceanography 5 (1), 1–13.
Meijer, N., Dupont-Nivet, G., Licht, A., Trabucho-Alexandre, J., Bourquin, S., Abels, H.A., 2020. Identifying eolian dust in the geological record. Earth Sci. Rev. 211, 103410.
Meinhold, G., 2010. Rutile and its applications in earth sciences. Earth Sci. Rev. 102 (1), 1–28.
Meinhold, G., Anders, B., Kostopoulos, D., Reischmann, T., 2008. Rutile chemistry and thermometry as provenance indicator: an example from Chios Island, Greece. Sediment. Geol. 203 (1), 98–111.
Meng, F., Zhang, J., Cui, M., 2013. Discovery of Early Paleozoic eclogite from the East Kunlun, Western China and its tectonic significance. Gondwana Res. 23 (2), 825–836.
Meyer, M., John, T., Brandt, S., Klemd, R., 2011. Trace element composition of rutile and the application of Zr-in-rutile thermometry to UHT metamorphism (Epupa Complex, NW Namibia). Lithos 126 (3), 388–401.
Miao, X., Sun, Y., Lu, H., Mason, J.A., 2004. Spatial pattern of grain size in the Late Pliocene 'Red Clay' deposits (North China) indicates transport by low-level northerly winds. Palaeogeogr. Palaeoclimatol. Palaeoecol. 206 (1), 149–155.
Morton, A.C., Hallsworth, C., 2007. Chapter 7 Stability of Detrital Heavy Minerals During Burial Diagenesis. In: Mange, M.A., Wright, D.T. (Eds.), Heavy minerals in use, Developments in Sedimentology Series 58. Elsevier, Amsterdam, pp. 215–245.
Nie, J., Peng, W., Pfaff, K., Möller, A., Garzanti, E., Andò, S., Stevens, T., Bird, A., Chang, H., Song, Y., Liu, S., Ji, S., 2013. Controlling factors on heavy mineral assemblages in Chinese loess and Red Clay. Palaeogeogr. Palaeoclimatol. Palaeoecol. 381-382, 110–118.
Nie, J., Peng, W., Möller, A., Song, Y., Stockli, D.F., Stevens, T., Horton, B.K., Liu, S., Bird, A., Oalmann, J., Gong, H., Fang, X., 2014a. Provenance of the upper Miocene–Pliocene Red Clay deposits of the Chinese loess plateau. Earth Planet. Sci. Lett. 407, 35–47.

Nie, J., Zhang, R., Necula, C., Heslop, D., Liu, Q., Gong, L., Banerjee, S., 2014b. Late Miocene–early Pleistocene paleoclimate history of the Chinese Loess Plateau revealed by remanence unmixing. Geophys. Res. Lett. 41 (6), 2163–2168.
Nie, J., Stevens, T., Rittner, M., Stockli, D., Garzanti, E., Limonta, M., Bird, A., Andò, S., Vermeesch, P., Saylor, J., Lu, H., Breecker, D., Hu, X., Liu, S., Resentini, A., Vezzoli, G., Peng, W., Carter, A., Ji, S., Pan, B., 2015. Loess Plateau storage of Northeastern Tibetan Plateau-derived Yellow River sediment. Nat. Commun. 6, 8511.
Nie, J., Pullen, A., Garzione, C.N., Peng, W., Wang, Z., 2018. Pre-Quaternary decoupling between Asian aridification and high dust accumulation rates. Sci. Adv. 4 (2).
Nie, J., Ren, X., Saylor, J.E., Su, Q., Horton, B.K., Bush, M.A., Chen, W., Pfaff, K., 2019. Magnetic polarity stratigraphy, provenance, and paleoclimate analysis of Cenozoic strata in the Qaidam Basin, NE Tibetan Plateau. Geol. Soc. Am. Bull. 132 (1–2), 310–320.
Pan, F., Li, J., Xu, Y., Wingate, M.T.D., Yue, L., Li, Y., Guo, L., Guo, L., Xi, R., 2018. Uplift of the Lüliang Mountains at ca. 5.7 Ma: Insights from provenance of the Neogene eolian red clay of the eastern Chinese Loess Plateau. Palaeogeogr. Palaeoclimatol. Palaeoecol. 502, 63–73.
Parfenov, L.M., Khanchuk, A.I., Badarch, G., Miller, R.J., Naumova, V.V., Nokleberg, W. J., Ogasawara, M., Prokopiev, A.V., Yan, H., 2004. Northeast Asia geodynamic map, 2004. US Geol. Surv. Open-File Report 2004 1252.
Peng, W., Wang, Z., Song, Y., Pfaff, K., Luo, Z., Nie, J., Chen, W., 2016. A comparison of heavy mineral assemblage between the loess and the Red Clay sequences on the Chinese Loess Plateau. Aeolian Res. 21, 87–91.
Pullen, A., Kapp, P., McCallister, A.T., Chang, H., Gehrels, G.E., Garzione, C.N., Heermance, R.V., Ding, L., 2011. Qaidam Basin and northern Tibetan Plateau as dust sources for the Chinese Loess Plateau and paleoclimatic implications. Geology 39 (11), 1031–1034.
Pullen, A., Ibáñez-Mejía, M., Gehrels, G.E., Ibáñez-Mejía, J.C., Pecha, M., 2014. What happens when n= 1000? Creating large-n geochronological datasets with LA-ICP-MS for geologic investigations. J. Anal. At. Spectrom. 29 (6), 971–980.
Qiang, X., An, Z., Song, Y., Chang, H., Sun, Y., Liu, W., Ao, H., Dong, J., Fu, C., Wu, F., Lu, F., Cai, Y., Zhou, W., Cao, J., Xu, X., Ai, L., 2011. New eolian red clay sequence on the western Chinese Loess Plateau linked to onset of Asian desertification about 25 Ma ago. Sci. China Earth Sci. 54 (1), 136–144.
Qu, J., Zhang, L., Ai, Y., Lü, Z., Wang, J., Zhou, H., Wang, S., 2007. High-pressure granulite from Western Kunlun, northwestern China: Its metamorphic evolution, zircon SHRIMP U-Pb ages and tectonic implication. Sci. China Ser. D Earth Sci. 50 (7), 961–971.
Ramstein, G., Fluteau, F., Besse, J., Joussaume, S., 1997. Effect of orogeny, plate motion and land–sea distribution on Eurasian climate change over the past 30 million years. Nature 386, 788.
Rea, D.K., Snoeckx, H., Joseph, L.H., 1998. Late Cenozoic Eolian deposition in the North Pacific: Asian drying, Tibetan uplift, and cooling of the northern hemisphere. Paleoceanography 13 (3), 215–224.
Ren, X., Nie, J., Saylor, J.E., Wang, X., Liu, F., Horton, B.K., 2020. Temperature control on silicate weathering intensity and evolution of the neogene East Asian Summer Monsoon. Geophys. Res. Lett. 47 (15) (e2020GL088808).
Reynolds, R., Belnap, J., Reheis, M., Lamothe, P., Luiszer, F., 2001. Aeolian dust in Colorado Plateau soils: Nutrient inputs and recent change in source. Proc. Natl. Acad. Sci. 98 (13), 7123–7127.
Rittner, M., Vermeesch, P., Carter, A., Bird, A., Stevens, T., Garzanti, E., Andò, S., Vezzoli, G., Dutt, R., Xu, Z., Lu, H., 2016. The provenance of Taklamakan desert sand. Earth Planet. Sci. Lett. 437, 127–137.
Roger, F., Malavieille, J., Leloup, P.H., Calassou, S., Xu, Z., 2004. Timing of granite emplacement and cooling in the Songpan–Garzè Fold Belt (eastern Tibetan Plateau) with tectonic implications. J. Asian Earth Sci. 22 (5), 465–481.
Ruddiman, W.F., Kutzbach, J.E., 1989. Forcing of late Cenozoic northern hemisphere climate by plateau uplift in southern Asia and the American west. J. Geophys. Res. 94 (D15), 18409–18427.
Santosh, M., Tsunogae, T., Li, J.H., Liu, S.J., 2007a. Discovery of sapphirine-bearing Mg–Al granulites in the North China Craton: implications for Paleoproterozoic ultrahigh temperature metamorphism. Gondwana Res. 11 (3), 263–285.
Santosh, M., Wilde, S.A., Li, J.H., 2007b. Timing of Paleoproterozoic ultrahigh-temperature metamorphism in the North China Craton: evidence from SHRIMP U–Pb zircon geochronology. Precambrian Res. 159 (3), 178–196.
Schindelin, J., Arganda-Carreras, I., Frise, E., Kaynig, V., Longair, M., Pietzsch, T., Preibisch, S., Rueden, C., Saalfeld, S., Schmid, B., Tinevez, J.-Y., White, D.J., Hartenstein, V., Eliceiri, K., Tomancak, P., Cardona, A., 2012. Fiji: an open-source platform for biological-image analysis. Nat. Methods 9 (7), 676–682.
Schudel, G., Lai, V., Gordon, K., Weis, D., 2015. Trace element characterization of USGS reference materials by HR-ICP-MS and Q-ICP-MS. Chem. Geol. 410, 223–236.
Shang, Y., Beets, C.J., Tang, H., Prins, M.A., Lahaye, Y., van Elsas, R., Sukselainen, L., Kaakinen, A., 2016. Variations in the provenance of the late Neogene Red Clay deposits in northern China. Earth Planet. Sci. Lett. 439, 88–100.
Shao, Y., Wyrwoll, K.-H., Chappell, A., Huang, J., Lin, Z., McTainsh, G.H., Mikami, M., Tanaka, T.Y., Wang, X., Yoon, S., 2011. Dust cycle: an emerging core theme in Earth system science. Aeolian Res. 2 (4), 181–204.
Shi, G., Li, X., Li, Q., Chen, Z., Deng, J., Liu, Y., Kang, Z., Pang, E., Xu, Y., Jia, X., 2012. Ion Microprobe U-Pb Age and Zr-in-Rutile Thermometry of Rutiles from the Daixian Rutile Deposit in the Hengshan Mountains, Shanxi Province, China. Econ. Geol. 107 (3), 525–535.
Shu, L.S., Deng, X.L., Zhu, W.B., Ma, D.S., Xiao, W.J., 2011. Precambrian tectonic evolution of the Tarim Block, NW China: new geochronological insights from the Quruqtagh domain. J. Asian Earth Sci. 42 (5), 774–790.
Sláma, J., Košler, J., 2012. Effects of sampling and mineral separation on accuracy of detrital zircon studies. Geochem. Geophys. Geosyst. 13 (5).
Sloan, L.C., Crowley, T.J., Pollard, D., 1996. Modeling of middle Pliocene climate with the NCAR GENESIS general circulation model. Mar. Micropaleontol. 27 (1), 51–61.
Song, D., Xiao, W., Han, C., Li, J., Qu, J., Guo, Q., Lin, L., Wang, Z., 2013a. Progressive accretionary tectonics of the Beishan orogenic collage, southern Altaids: insights from zircon U–Pb and Hf isotopic data of high-grade complexes. Precambrian Res. 227, 368–388.
Song, S., Zhang, L., Niu, Y., 2004. Ultra-deep origin of garnet peridotite from the North Qaidam ultrahigh-pressure belt, Northern Tibetan Plateau, NW China. Am. Mineral. 89 (8–9), 1330–1336.
Song, S., Niu, Y., Su, L., Xia, X., 2013b. Tectonics of the North Qilian orogen, NW China. Gondwana Res. 23 (4), 1378–1401.
Song, S., Bi, H., Qi, S., Yang, L., Allen, M.B., Niu, Y., Su, L., Li, W., 2018. HP–UHP metamorphic belt in the East Kunlun Orogen: final closure of the Proto-Tethys Ocean and formation of the Pan-North-China Continent. J. Petrol. 59 (11), 2043–2060.
Song, S.G., Zhang, L.F., Niu, Y., Wei, C.J., Liou, J.G., Shu, G.M., 2007. Eclogite and carpholite-bearing metasedimentary rocks in the North Qilian suture zone, NW China: implications for Early Palaeozoic cold oceanic subduction and water transport into mantle. J. Metamorph. Geol. 25 (5), 547–563.
Song, Y., Fang, X., Li, J., An, Z.S., Yang, D., Lu, L.Q., 2000. Age of red clay at Chaona section near eastern Liupan Mountain and its tectonic significance. Quat. Sci. 20 (5), 457–463.
Spicer, R.A., Su, T., Valdes, P.J., Farnsworth, A., Wu, F.-X., Shi, G., Spicer, T.E.V., Zhou, Z., 2020. Why 'the uplift of the Tibetan Plateau' is a myth. Natl. Sci. Rev. 8 (1).
Stacey, J.S., Kramers, J.D., 1975. Approximation of terrestrial lead isotope evolution by a two-stage model. Earth Planet. Sci. Lett. 26 (2), 207–221.
Steiger, R.H., Jäger, E., 1977. Subcommission on geochronology: convention on the use of decay constants in geo- and cosmochronology. Earth Planet. Sci. Lett. 36 (3), 359–362.
Steinshouer, D.W., Qiang, J., McCabe, P.J., Ryder, R.T., 1999. Maps showing geology, oil and gas fields, and geologic provinces of the Asia Pacific region. US Geol. Surv. Open-File Report 97-470-F 16. https://doi.org/10.3133/ofr97470F.
Stern, R.J., Li, S.-M., Randy Keller, G., 2018. Continental crust of China: a brief guide for the perplexed. Earth Sci. Rev. 179, 72–94.
Stevens, T., Carter, A., Palk, C., Lu, H., Clift, P.D., 2010. Assessing the provenance of loess and desert sediments in northern China using U-Pb dating and morphology of detrital zircons. Geol. Soc. Am. Bull. 122 (7–8), 1331–1344.
Stevens, T., Carter, A., Watson, T.P., Vermeesch, P., Andò, S., Bird, A.F., Lu, H., Garzanti, E., Cottam, M.A., Sevastjanova, I., 2013. Genetic linkage between the Yellow River, the Mu Us desert and the Chinese Loess Plateau. Quat. Sci. Rev. 78, 355–368.
Su, Q., Nie, J., Meng, Q., Heermance, R., Gong, L., Luo, Z., Wang, Z., Zhang, R., Garzione, C., 2019a. Central Asian Drying at 3.3 Ma Linked to tropical forcing? Geophys. Res. Lett. 46 (17–18), 10561–10567.
Su, T., Farnsworth, A., Spicer, R.A., Huang, J., Wu, F.-X., Liu, J., Li, S.-F., Xing, Y.-W., Huang, Y.-J., Deng, W.-Y.-D., Tang, H., Xu, C.-L., Zhao, F., Srivastava, G., Valdes, P. J., Deng, T., Zhou, Z.-K., 2019b. No high Tibetan Plateau until the Neogene. Sci. Adv. 5 (3), eaav2189.
Su, W., Li, J., Mao, Q., Gao, J., Liu, X., Chen, F., Ge, X.-M., 2018. Rutile in HP rocks from the Western Tianshan, China: mineralogy and its economic implications. J. Earth Sci. 29 (5), 1049–1059.
Sun, D., An, Z., Shaw, J., Bloemendal, J., Sun, Y., 1998. Magnetostratigraphy and palaeoclimatic significance of Late Tertiary aeolian sequences in the Chinese Loess Plateau. Geophys. J. Int. 134 (1), 207–212.
Sun, J., 2002. Provenance of loess material and formation of loess deposits on the Chinese Loess Plateau. Earth Planet. Sci. Lett. 203 (3), 845–859.
Sun, J., 2005. Nd and Sr isotopic variations in Chinese eolian deposits during the past 8 Ma: implications for provenance change. Earth Planet. Sci. Lett. 240 (2), 454–466.
Sun, J., Liu, T., 2006. The age of the Taklimakan desert. Science 312 (5780), 1621.
Sun, J., Zhu, X., 2010. Temporal variations in Pb isotopes and trace element concentrations within Chinese eolian deposits during the past 8Ma: implications for provenance change. Earth Planet. Sci. Lett. 290 (3), 438–447.
Sun, J., Zhang, Z., Zhang, L., 2009. New evidence on the age of the Taklimakan Desert. Geology 37 (2), 159–162.
Sun, Y., Yan, Y., Nie, J., Li, G., Shi, Z., Qiang, X., Chang, H., An, Z., 2020. Source-to-sink fluctuations of Asian aeolian deposits since the late Oligocene. Earth Sci. Rev. 200, 102963.
Tam, P.Y., Zhao, G., Sun, M., Li, S., Iizuka, Y., Ma, G.S.-K.I., Yin, C., He, Y., Wu, M., 2012. Metamorphic P–T path and tectonic implications of medium-pressure pelitic granulites from the Jiaobei massif in the Jiao-Liao-Ji Belt, North China Craton. Precambrian Res. 220-221, 177–191.
Tan, Z., Agard, P., Gao, J., Hong, T., Wan, B., 2019. Concordant pulse in Mn, Y and HREEs concentrations during UHP eclogitic garnet growth: transient rock dynamics along a cold subduction plate interface. Earth Planet. Sci. Lett. 530, 115908.
Tang, L., Santosh, M., 2018. Neoarchean-Paleoproterozoic terrane assembly and Wilson cycle in the North China Craton: an overview from the central segment of the Trans-North China Orogen. Earth Sci. Rev. 182, 1–27.
Taylor, J.P., Webb, L.E., Johnson, C.L., Heumann, M.J., 2013. The Lost South Gobi Microcontinent: Protolith studies of Metamorphic Tectonites and implications for the evolution of continental crust in Southeastern Mongolia. Geosciences 3 (3), 543–584.
Tegen, I., 2003. Modeling the mineral dust aerosol cycle in the climate system. Quat. Sci. Rev. 22 (18), 1821–1834.
Tegen, I., Lacis, A.A., Fung, I., 1996. The influence on climate forcing of mineral aerosols from disturbed soils. Nature 380 (6573), 419–422.

Teng, X., Zhang, J., Mao, X., Lu, Z., Zhou, G., 2020. The earliest Cambrian UHT metamorphism in the Qaidam block, western China: a record of the final assembly of Greater Gondwana? Gondwana Res. 87, 118–137.
Tomkins, H.S., Powell, R., Ellis, D.J., 2007. The pressure dependence of the zirconium-in-rutile thermometer. J. Metamorph. Geol. 25 (6), 703–713.
Trap, P., Faure, M., Lin, W., Le Breton, N., Monié, P., 2012. Paleoproterozoic tectonic evolution of the Trans-North China Orogen: toward a comprehensive model. Precambrian Res. 222-223, 191–211.
Triebold, S., von Eynatten, H., Luvizotto, G.L., Zack, T., 2007. Deducing source rock lithology from detrital rutile geochemistry: an example from the Erzgebirge, Germany. Chem. Geol. 244 (3), 421–436.
Triebold, S., Luvizotto, G.L., Tolosana-Delgado, R., Zack, T., von Eynatten, H., 2011. Discrimination of TiO2 polymorphs in sedimentary and metamorphic rocks. Contrib. Mineral. Petrol. 161 (4), 581–596.
Triebold, S., von Eynatten, H., Zack, T., 2012. A recipe for the use of rutile in sedimentary provenance analysis. Sediment. Geol. 282, 268–275.
Újvári, G., Klötzli, U., Kiraly, F., Ntaflos, T., 2013. Towards identifying the origin of metamorphic components in Austrian loess: insights from detrital rutile chemistry, thermometry and U–Pb geochronology. Quat. Sci. Rev. 75, 132–142.
Van Achterberg, E., Ryan, C., Jackson, S., Griffin, W., 2001. Appendix 3: Data reduction software for LA-ICP-MS. In: Sylvester, P.J. (Ed.), Laser ablation-ICP-mass spectrometry in the Earth Sciences: Principles and applications: Ottawa, Ontario, Mineral. Assoc. Can., Short Course Series, 29, pp. 239–243.
de la Vega, E., Chalk, T.B., Wilson, P.A., Bysani, R.P., Foster, G.L., 2020. Atmospheric CO2 during the Mid-Piacenzian Warm Period and the M2 glaciation. Sci. Rep. 10 (1), 11002.
Vermeesch, P., 2004. How many grains are needed for a provenance study? Earth Planet. Sci. Lett. 224 (3), 441–451.
Vermeesch, P., 2013. Multi-sample comparison of detrital age distributions. Chem. Geol. 341, 140–146.
Vermeesch, P., Resentini, A., Garzanti, E., 2016. An R package for statistical provenance analysis. Sediment. Geol. 336, 14–25.
Wan, Y., Liu, D., Nutman, A., Zhou, H., Dong, C., Yin, X., Ma, M., 2012. Multiple 3.8–3.1Ga tectono-magmatic events in a newly discovered area of ancient rocks (the Shengousi Complex), Anshan, North China Craton. J. Asian Earth Sci. 54-55, 18–30.
Wang, B., Liu, H., Shu, L., Jahn, B.-M., Chung, S.-L., Zhai, Y., Liu, D., 2014b. Early Neoproterozoic crustal evolution in northern Yili Block: insights from migmatite, orthogneiss and leucogranite of the Wenquan metamorphic complex in the NW Chinese Tianshan. Precambrian Res. 242, 58–81.
Wang, B., Kaakinen, A., Clift, P.D., 2018. Tectonic controls of the onset of aeolian deposits in Chinese Loess Plateau – a preliminary hypothesis. Int. Geol. Rev. 60 (8), 945–955.
Wang, C., Liu, L., Yang, W.-Q., Zhu, X.-H., Cao, Y.-T., Kang, L., Chen, S.-F., Li, R.-S., He, S.-P., 2013. Provenance and ages of the Altyn Complex in Altyn Tagh: implications for the early Neoproterozoic evolution of northwestern China. Precambrian Res. 230, 193–208.
Wang, C., Wang, Y.-H., Liu, L., He, S.-P., Li, R.-S., Li, M., Yang, W.-Q., Cao, Y.-T., Meert, J.G., Shi, C., 2014a. The Paleoproterozoic magmatic–metamorphic events and cover sediments of the Tiekelik Belt and their tectonic implications for the southern margin of the Tarim Craton, northwestern China. Precambrian Res. 254, 210–225.
Wan, Y., Xu, Z., Yang, J., Zhang, J., 2001. Ages and Compositions of the Precambrian High-grade Basement of the Qilian Terrane and Its Adjacent Areas. Acta Geologica Sinica - English Edition 75 (4), 375–384. https://doi.org/10.1111/j.1755-6724.2001.tb00055.x.
Wang, C., Dai, J., Zhao, X., Li, Y., Graham, S.A., He, D., Ran, B., Meng, J., 2014c. Outward-growth of the Tibetan Plateau during the Cenozoic: aA review. Tectonophysics 621, 1–43.
Wang, C., Lai, Y.-J., Foley, S.F., Liu, Y., Belousova, E., Zong, K., Hu, Z., 2020. Rutile records for the cooling history of the Trans-North China orogen from assembly to break-up of the Columbia supercontinent. Precambrian Res. 346, 105763.
Wang, E., Wan, J., Liu, J., 2003. Late Cenozoic geological evolution of the foreland basin bordering the West Kunlun range in Pulu area: constraints on timing of uplift of northern margin of the Tibetan Plateau. J. Geophys. Res. 108 (B8).
Wang, E., Kirby, E., Furlong, K.P., van Soest, M., Xu, G., Shi, X., Kamp, P.J.J., Hodges, K. V., 2012. Two-phase growth of high topography in eastern Tibet during the Cenozoic. Nat. Geosci. 5 (9), 640–645.
Wang, G., Wu, C., Chen, C., Zhou, Z., Liu, C., Jiang, T., 2017a. Geochronological data of igneous and metamorphic rocks from the Xing'an-Mongolia Orogenic Belt of the eastern Central Asian Orogenic Belt: implications for the final closure of the Paleo-Asian Ocean. Int. J. Earth Sci. 106 (8), 2727–2746.
Wang, J., Wu, Y., Gao, S., Peng, M., Liu, X., Zhao, L., Zhou, L., Hu, Z., Gong, H., Liu, Y., 2010. Zircon U–Pb and trace element data from rocks of the Huai'an Complex: new insights into the late Paleoproterozoic collision between the Eastern and Western Blocks of the North China Craton. Precambrian Res. 178 (1), 59–71.
Wang, R., Zhou, D., Wang, J., Wang, Y., Liu, Y., 1999. Variscan terrane of deep-crustal granulite facies in Yushugou area, southern Tianshan. Sci. China Ser. D: Earth Sciences 42 (5), 482–490.
Wang, T., Zheng, Y., Gehrels, G.E., Mu, Z., 2001. Geochronological evidence for existence of South Mongolian microcontinent—A zircon U-Pb age of grantoid gneisses from the Yagan-Onch Hayrhan metamorphic core complex. Chin. Sci. Bull. 46 (23), 2005.
Wang, W., Zheng, W., Zhang, P., Li, Q., Kirby, E., Yuan, D., Zheng, D., Liu, C., Wang, Z., Zhang, H., Pang, J., 2017b. Expansion of the Tibetan Plateau during the Neogene. Nat. Commun. 8 (1), 15887.
Wang, Y.-X., Yang, J.-D., Chen, J., Zhang, K.-J., Rao, W.-B., 2007. The Sr and Nd isotopic variations of the Chinese Loess Plateau during the past 7 Ma: implications for the East Asian winter monsoon and source areas of loess. Palaeogeogr. Palaeoclimatol. Palaeoecol. 249 (3), 351–361.
Wang, Z., Nie, J., Wang, J., Zhang, H., Peng, W., Garzanti, E., Hu, X., Stevens, T., Pfaff, K., Pan, B., 2019. Testing contrasting models of the formation of the Upper Yellow River Using Heavy-Mineral Data From the Yinchuan Basin Drill Cores. Geophys. Res. Lett. 46 (17–18), 10338–10345.
Wasiljeff, J., Kaakinen, A., Salminen, J.M., Zhang, Z., 2020. Magnetostratigraphic constraints on the fossiliferous Ulantatal sequence in Inner Mongolia, China: implications for Asian aridification and faunal turnover before the Eocene-Oligocene boundary. Earth Planet. Sci. Lett. 535, 116125.
Watson, E.B., Wark, D.A., Thomas, J.B., Petrology, 2006. Crystallization thermometers for zircon and rutile. Contrib. Mineral. Petrol. 151 (4), 413.
Wei, C., Clarke, G., Tian, W., Qiu, L., 2007. Transition of metamorphic series from the Kyanite- to andalusite-types in the Altai orogen, Xinjiang, China: evidence from petrography and calculated KMnFMASH and KFMASH phase relations. Lithos 96 (3), 353–374.
Weislogel, A.L., Graham, S.A., Chang, E.Z., Wooden, J.L., Gehrels, G.E., Yang, H., 2006. Detrital zircon provenance of the Late Triassic Songpan-Ganzi complex: sedimentary record of collision of the North and South China blocks. Geology 34 (2), 97–100.
Wen, L., Lu, H., Qiang, X., 2005. Changes in grain-size and sedimentation rate of the Neogene Red Clay deposits along the Chinese Loess Plateau and implications for the palaeowind system. Sci. China Ser. D: Earth Sciences 48 (9), 1452–1462.
Wilhem, C., Windley, B.F., Stampfli, G.M., 2012. The Altaids of Central Asia: a tectonic and evolutionary innovative review. Earth Sci. Rev. 113 (3), 303–341.
Windley, B.F., Kröner, A., Guo, J., Qu, G., Li, Y., Zhang, C., 2002. Neoproterozoic to Paleozoic geology of the Altai Orogen, NW China: new zircon age data and tectonic evolution. J. Geol. 110 (6), 719–737.
Wu, F.-Y., Sun, D.-Y., Ge, W.-C., Zhang, Y.-B., Grant, M.L., Wilde, S.A., Jahn, B.-M., 2011. Geochronology of the Phanerozoic granitoids in northeastern China. J. Asian Earth Sci. 41 (1), 1–30.
Xiao, W., Windley, B.F., Hao, J., Zhai, M., 2003. Accretion leading to collision and the Permian Solonker suture, Inner Mongolia, China: termination of the central Asian orogenic belt. Tectonics 22 (6).
Xiao, W., Windley, B.F., Allen, M.B., Han, C., 2013. Paleozoic multiple accretionary and collisional tectonics of the Chinese Tianshan orogenic collage. Gondwana Res. 23 (4), 1316–1341.
Xiao, W., Windley, B.F., Sun, S., Li, J., Huang, B., Han, C., Yuan, C., Sun, M., Chen, H., 2015. A tale of Amalgamation of three Permo-Triassic collage systems in Central Asia: Oroclines, Sutures, and Terminal Accretion. Annu. Rev. Earth Planet. Sci. 43 (1), 477–507.
Xiao, W., Ao, S., Yang, L., Han, C., Wan, B., Zhang, J.E., Zhang, Z., Li, R., Chen, Z., Song, S., 2017. Anatomy of composition and nature of plate convergence: insights for alternative thoughts for terminal India-Eurasia collision. Sci. China Earth Sci. 60 (6), 1015–1039.
Xiao, W.J., Mao, Q.G., Windley, B.F., Han, C.M., Qu, J.F., Zhang, J.E., Ao, S.J., Guo, Q.Q., Cleven, N.R., Lin, S.F., Shan, Y.H., Li, J.L., 2010. Paleozoic multiple accretionary and collisional processes of the Beishan orogenic collage. Am. J. Sci. 310, 1553–1594.
Xiong, S., Ding, Z., Zhu, Y., Zhou, R., Lu, H., 2010. A ~6Ma chemical weathering history, the grain size dependence of chemical weathering intensity, and its implications for provenance change of the Chinese loess–red clay deposit. Quat. Sci. Rev. 29 (15), 1911–1922.
Xu, Y., Yue, L., Li, J., Sun, L., Sun, B., Zhang, J., Ma, J., Wang, J., 2009. An 11-Ma-old red clay sequence on the Eastern Chinese Loess Plateau. Palaeogeogr. Palaeoclimatol. Palaeoecol. 284 (3), 383–391.
Xu, Y.-G., Wei, X., Luo, Z.-Y., Liu, H.-Q., Cao, J., 2014. The early permian Tarim Large Igneous Province: main characteristics and a plume incubation model. Lithos 204, 20–35.
Yan, Y., Ma, L., Sun, Y., 2017. Tectonic and climatic controls on provenance changes of fine-grained dust on the Chinese Loess Plateau since the late Oligocene. Geochim. Cosmochim. Acta 200, 110–122.
Yang, S.-F., Li, Z., Chen, H., Santosh, M., Dong, C.-W., Yu, X., 2007. Permian bimodal dyke of Tarim Basin, NW China: geochemical characteristics and tectonic implications. Gondwana Res. 12 (1), 113–120.
Yang, S.L., Ding, Z.L., 2004. Comparison of particle size characteristics of the Tertiary 'red clay' and Pleistocene loess in the Chinese Loess Plateau: implications for origin and sources of the 'red clay'. Sedimentology 51 (1), 77–93.
Yarmolyuk, V., Kovalenko, V.I., Sacenikova, E., Kozakov, I.K., Kotov, A.B., Kovach, V., Vladykin, N.V., Yakovleva, S.J.D.E.S., 2005. U-Pb age of Syn- and postmetamorphic granitoids of south Mongolia: evidence for the presence of grenvillides in the central Asian foldbelt. Dokl. Earth Sci. 404, 986–990.
Yin, A., Harrison, T.M., 2000. Geologic Evolution of the Himalayan-Tibetan Orogen. Annu. Rev. Earth Planet. Sci. 28 (1), 211–280.
Yin, Y., Chen, L., 2007. The effects of heating by transported dust layers on cloud and precipitation: a numerical study. Atmos. Chem. Phys. 7 (13), 3497–3505.
You, Z., Han, Y., Suo, S., Chen, N., Zhong, Z., 1993. Metamorphic history and tectonic evolution of the Qinling Complex, eastern Qinling Mountains, China. J. Metamorph. Geol. 11 (4), 549–560.
Yuan, C., Sun, M., Zhou, M.-F., Zhou, H., Xiao, W.-J., Li, J.-L., 2002. Tectonic Evolution of the West Kunlun: geochronologic and geochemical constraints from kudi granitoids. Int. Geol. Rev. 44 (7), 653–669.
Yuan, D.-Y., Ge, W.-P., Chen, Z.-W., Li, C.-Y., Wang, Z.-C., Zhang, H.-P., Zhang, P.-Z., Zheng, D.-W., Zheng, W.-J., Craddock, W.H., Dayem, K.E., Duvall, A.R., Hough, B.G., Lease, R.O., Champagnac, J.-D., Burbank, D.W., Clark, M.K., Farley, K.A., Garzione, C.N., Kirby, E., Molnar, P., Roe, G.H., 2013. The growth of northeastern Tibet and its relevance to large-scale continental geodynamics: a review of recent studies. Tectonics 32 (5), 1358–1370.

Zack, T., Kronz, A., Foley, S.F., Rivers, T., 2002. Trace element abundances in rutiles from eclogites and associated garnet mica schists. Chem. Geol. 184 (1), 97–122.
Zack, T., Moraes, R., Kronz, A., 2004a. Temperature dependence of Zr in rutile: empirical calibration of a rutile thermometer. Contrib. Mineral. Petrol. 148 (4), 471–488.
Zack, T., von Eynatten, H., Kronz, A., 2004b. Rutile geochemistry and its potential use in quantitative provenance studies. Sediment. Geol. 171 (1), 37–58.
Zan, J., Li, X., Fang, X., Zhang, W., Yan, M., Mao, Z., 2018. Grain-size analysis of Upper Pliocene red clay deposits from Linxia Basin: implications for Asian monsoon evolution on the NE margin of the Tibetan Plateau. Palaeogeogr. Palaeoclimatol. Palaeoecol. 511, 597–605.
Zhai, M., Zhou, Y., 2015. General Precambrian Geology in China. In: Zhai, M. (Ed.), Precambrian Geology of China. Springer, Berlin Heidelberg, pp. 3–56.
Zhang, C.-L., Li, H.-K., Santosh, M., Li, Z.-X., Zou, H.-B., Wang, H., Ye, H., 2012a. Precambrian evolution and cratonization of the Tarim Block, NW China: Petrology, geochemistry, Nd-isotopes and U–Pb zircon geochronology from Archaean gabbro-TTG–potassic granite suite and Paleoproterozoic metamorphic belt. J. Asian Earth Sci. 47, 5–20.
Zhang, C.-L., Zou, H.-B., Li, H.-K., Wang, H.-Y., 2013. Tectonic framework and evolution of the Tarim Block in NW China. Gondwana Res. 23 (4), 1306–1315.
Zhang, G., Ellis, D.J., Christy, A.G., Zhang, L., Song, S., 2010. Zr-in-rutile thermometry in HP/UHP eclogites from Western China. Contrib. Mineral. Petrol. 160 (3), 427–439.
Zhang, H., Lu, H., Xu, X., Liu, X., Yang, T., Stevens, T., Bird, A., Xu, Z., Zhang, T., Lei, F., Feng, H., 2016a. Quantitative estimation of the contribution of dust sources to Chinese loess using detrital zircon U-Pb age patterns. J. Geophys. Res. Earth Surf. 121 (11), 2085–2099.
Zhang, H., Lu, H., Stevens, T., Feng, H., Fu, Y., Geng, J., Wang, H., 2018a. Expansion of Dust Provenance and Aridification of Asia Since ~7.2 Ma Revealed by Detrital Zircon U-Pb Dating. Geophys. Res. Lett. 45 (24), 13437–13448.
Zhang, H., Nie, J., Liu, X., Pullen, A., Li, G., Peng, W., Zhang, H., 2021a. Spatially variable provenance of the Chinese Loess Plateau. Geology 49.
Zhang, H., Lu, H., Zhou, Y., Cui, Y., He, J., Lv, H., Wang, K., Wang, X., 2021b. Heavy mineral assemblages and UPb detrital zircon geochronology of sediments from the Weihe and Sanmen Basins: new insights into the Pliocene-Pleistocene evolution of the Yellow River. Palaeogeogr. Palaeoclimatol. Palaeoecol. 562, 110072.
Zhang, J., Mattinson, C.G., Meng, F., Wan, Y., Tung, K., 2008. Polyphase tectonothermal history recorded in granulitized gneisses from the north Qaidam HP/UHP metamorphic terrane, western China: evidence from zircon U-Pb geochronology. Geol. Soc. Am. Bull. 120 (5–6), 732–749.
Zhang, J., Gong, J., Yu, S., 2012b. c. 1.85 Ga HP granulite-facies metamorphism in the Dunhuang block of the Tarim Craton, NW China: evidence from U–Pb zircon dating of mafic granulites. J. Geol. Soc. 169 (5), 511–514.
Zhang, J., Wei, C., Chu, H., Chen, Y., 2016b. Mesozoic metamorphism and its tectonic implication along the Solonker suture zone in central Inner Mongolia, China. Lithos 261, 262–277.
Zhang, J.-R., Wei, C.-J., Chu, H., 2018b. High-T and low-P metamorphism in the Xilingol Complex of central Inner Mongolia, China: an indicator of extension in a previous orogeny. J. Metamorph. Geol. 36 (4), 393–417.
Zhang, J.X., Meng, F.C., Wan, Y.S., 2007. A cold Early Palaeozoic subduction zone in the North Qilian Mountains, NW China: petrological and U-Pb geochronological constraints. J. Metamorph. Geol. 25 (3), 285–304.
Zhang, J.X., Mattinson, C.G., Yu, S.Y., Li, Y.S., 2014a. Combined rutile–zircon thermometry and U–Pb geochronology: new constraints on Early Paleozoic HP/UHT granulite in the south Altyn Tagh, north Tibet, China. Lithos 200-201, 241–257.
Zhang, L., Jin, Z., 2016. High-temperature metamorphism of the Yushugou ophiolitic slice: late Devonian subduction of seamount and mid-oceanic ridge in the South Tianshan orogen. J. Asian Earth Sci. 132, 75–93.
Zhang, L., Jiang, W., Wei, C., Dong, S., 1999. Discovery of deerite from the Aksu Precambrian blueschist terrane and its geological significance. Sci. China Ser. D: Earth Sciences 42 (3), 233–239.
Zhang, L.-Y., Ding, L., Pullen, A., Xu, Q., Liu, D.-L., Cai, F.-L., Yue, Y.-H., Lai, Q.-Z., Shi, R.-D., Ducea, M.N., Kapp, P., Chapman, A., 2014b. Age and geochemistry of western Hoh-Xil–Songpan-Ganzi granitoids, northern Tibet: implications for the Mesozoic closure of the Paleo-Tethys ocean. Lithos 190-191, 328–348.
Zhang, R.Y., Liou, J.G., Tsai, C.H., 1996. Petrogenesis of a high-temperature metamorphic terrane: a new tectonic interpretation for the north Dabieshan, central China. J. Metamorph. Geol. 14 (3), 319–333.
Zhang, T., Fan, S., Chen, S., Lu, Y., 2019. Climate change and tectonic implications during the Pliocene climate transition interval from lacustrine records in western Wei River Basin, central China. Geol. J. 1–15.
Zhang, Y., Sun, D., Li, Z., Wang, F., Wang, X., Li, B., Guo, F., Wu, S., 2014c. Cenozoic record of aeolian sediment accumulation and aridification from Lanzhou, China, driven by Tibetan Plateau uplift and global climate. Glob. Planet. Chang. 120, 1–15.
Zhao, G., Cawood, P.A., 2012. Precambrian geology of China. Precambrian Res. 222-223, 13–54.
Zhao, G., Wilde, S.A., Cawood, A., P. and Lu, L., 1999. Tectonothermal history of the basement rocks in the western zone of the North China Craton and its tectonic implications. Tectonophysics 310 (1), 37–53.
Zhao, G., Cawood, P.A., Wilde, S.A., Sun, M., Lu, L., 2000. Metamorphism of basement rocks in the Central Zone of the North China Craton: implications for Paleoproterozoic tectonic evolution. Precambrian Res. 103 (1), 55–88.
Zhao, G., Sun, M., Wilde, S.A., Sanzhong, L., 2005. Late Archean to Paleoproterozoic evolution of the North China Craton: key issues revisited. Precambrian Res. 136 (2), 177–202.
Zhao, G., Wilde, S.A., Sun, M., Guo, J., Kröner, A., Li, S., Li, X., Zhang, J., 2008. SHRIMP U–Pb zircon geochronology of the Huai'an Complex: constraints on Late Archean to Paleoproterozoic magmatic and metamorphic events in the Trans-North China Orogen. Am. J. Sci. 308, 520–547.
Zhao, G., Cawood, P.A., Li, S., Wilde, S.A., Sun, M., Zhang, J., He, Y., Yin, C., 2012. Amalgamation of the North China Craton: key issues and discussion. Precambrian Res. 222-223, 55–76.
Zhao, G., Wang, Y., Huang, B., Dong, Y., Li, S., Zhang, G., Yu, S., 2018. Geological reconstructions of the East Asian blocks: from the breakup of Rodinia to the assembly of Pangea. Earth Sci. Rev. 186, 262–286.
Zhao, L., Liu, X., 2019. Metallogenic and tectonic implications of detrital zircon U–Pb, Hf isotopes, and detrital rutile geochemistry of late carboniferous karstic bauxite on the southern margin of the North China Craton. Lithos 350-351, 105222.
Zhao, L., Liu, X., Yang, S., Ma, X., Liu, L., Sun, X., 2021. Regional multi-sources of Carboniferous karstic bauxite deposits in North China Craton: insights from multi-proxy provenance systems. Sediment. Geol. 421, 105958.
Zhao, X., Liu, C., Wang, J., Zhang, S., Guan, Y., 2020. Geochemistry, geochronology and Hf isotope of granitoids in the northern Alxa region: implications for the Late Paleozoic tectonic evolution of the Central Asian Orogenic Belt. Geosci. Front. 11 (5), 1711–1725.
Zheng, D., Clark, M.K., Zhang, P., Zheng, W., Farley, K.A., 2010. Erosion, fault initiation and topographic growth of the North Qilian Shan (northern Tibetan Plateau). Geosphere 6 (6), 937–941.
Zheng, H., Wei, X., Tada, R., Clift, P.D., Wang, B., Jourdan, F., Wang, P., He, M., 2015. Late Oligocene–early Miocene birth of the Taklimakan Desert. Proc. Natl. Acad. Sci. 112 (25), 7662–7667.
Zhou, G., Zhang, J., Li, Y., Lu, Z., Mao, X., Teng, X., 2019. Metamorphic Evolution and Tectonic Implications of the Granulitized Eclogites from the Luliangshan Terrane in the North Qaidam Ultrahigh Pressure Metamorphic Belt, NW China: new constraints from phase equilibrium modeling. J. Earth Sci. 30 (3), 585–602.
Zhou, J.-B., Wilde, S.A., 2013. The crustal accretion history and tectonic evolution of the NE China segment of the Central Asian Orogenic Belt. Gondwana Res. 23 (4), 1365–1377.
Zhou, J.-B., Wilde, S.A., Zhang, X.-Z., Zhao, G.-C., Liu, F.-L., Qiao, D.-W., Ren, S.-M., Liu, J.-H., 2011. A >1300km late Pan-African metamorphic belt in NE China: new evidence from the Xing'an block and its tectonic implications. Tectonophysics 509 (3), 280–292.
Zhou, J.-B., Wilde, S.A., Zhao, G.-C., Han, J., 2018. Nature and assembly of microcontinental blocks within the Paleo-Asian Ocean. Earth Sci. Rev. 186, 76–93.
Zhu, B., Kidd, William S.F., Rowley, David B., Currie, Brian S., Shafique, N., 2005. Age of initiation of the India-Asia Collision in the East-Central Himalaya. J. Geol. 113 (3), 265–285.
Zhu, W., Zheng, B., Shu, L., Ma, D., Wu, H., Li, Y., Huang, W., Yu, J., 2011. Neoproterozoic tectonic evolution of the Precambrian Aksu blueschist terrane, northwestern Tarim, China: insights from LA-ICP-MS zircon U–Pb ages and geochemical data. Precambrian Res. 185 (3), 215–230.
Zhu, Y., Zhou, L., Mo, D., Kaakinen, A., Zhang, Z., Fortelius, M., 2008. A new magnetostratigraphic framework for late Neogene Hipparion Red Clay in the eastern Loess Plateau of China. Palaeogeogr. Palaeoclimatol. Palaeoecol. 268 (1), 47–57.
Zong, K., Klemd, R., Yuan, Y., He, Z., Guo, J., Shi, X., Liu, Y., Hu, Z., Zhang, Z., 2017. The assembly of Rodinia: the correlation of early Neoproterozoic (ca. 900Ma) high-grade metamorphism and continental arc formation in the southern Beishan Orogen, southern Central Asian Orogenic Belt (CAOB). Precambrian Res. 290, 32–48.